Large Magnetocaloric Effect in Low-Cost Transition Metal Based Alloys for Magnetic Refrigeration

Thesis submitted for the degree of

Doctor of Philosophy (Science)

in

Physics (Experimental)

by

Subrata Ghosh

Department of Physics

Jadavpur University

2020

CENTRE FOR BASIC SCIENCES 1986
S.N. BOSE NATIONAL
1894-1974
विज्ञानेन परिपश्यन्ति धीराः

सत्येन्द्र नाथ बसु राष्ट्रीय मौलिक विज्ञान केन्द्र
SATYENDRA NATH BOSE NATIONAL
CENTRE FOR BASIC SCIENCES
সত্যেন্দ্র নাথ বসু জাতীয় মৌল বিজ্ঞান কেন্দ্র

CERTIFICATE FROM THE SUPERVISOR

This is to certify that the thesis entitled "**Large Magnetocaloric Effect in Low-Cost Transition Metal Based Alloys for Magnetic Refrigeration**" submitted by **Sri Subrata Ghosh** who got his name registered on **09th May, 2016** for the award of Ph. D. (Science) degree of Jadavpur University, is absolutely based upon his own work under the supervision of **Prof. Kalyan Mandal** and that neither this thesis nor any part of it has been submitted for either any degree/diploma or any other academic award anywhere before.

Kalyan Mandal 24-12-2020

(Signature of the Supervisor with official seal and date)

डॉ. कल्याण मण्डल / Dr. Kalyan Mandal
वरिष्ठ प्राध्यापक / Senior Professor
संघनित पदार्थ भौतिकी एवं सामग्री विज्ञान विभाग
Dept. of Condensed Matter Physics and Material Sciences
सत्येंद्र नाथ बसु राष्ट्रीय मौलिक विज्ञान केंद्र
S. N. Bose National Centre for Basic Sciences
ब्लॉक-जे.डी., सेक्टर-III, सॉल्ट लेक, कोलकाता-700106, भारत
Block-JD, Sector-III, Salt Lake, Kolkata-700106, India

Dedicated to Satyen da……..

Abstract

Energy-efficient and eco-friendly magnetic refrigeration technology based on magnetocaloric effect (MCE), which has enormous potential to replace the conventional vapor compression technology, is expected to be applicable in the solid-state based modern refrigeration devices. The crucial requirement of a magnetic refrigerator is giant magnetocaloric materials consist of transition metal (TM) based, less expensive, earth-abundant, and nontoxic elements for commercial application. In this thesis, we have investigated the MCE response of certain cost-effective TM based alloys such as MnNiSi-based intermetallic compounds and NiMn-based Heusler alloys which are found to exhibit large isothermal magnetic entropy change (ΔS_M), an important parameter to quantify MCE of a material, associated with large relative cooling power (RCP) around room temperature (RT).

Magnetic and structural transitions are observed to coincide at around RT in TM based $(Mn_{0.6}Fe_{0.4})NiSi_{1-x}Al_x$ (x = 0.06, 0.07) alloys and $(MnNiSi)_{1-y}(FeCoGa)_y$ (y = 0.15 – 0.17) alloys which lead to a coupled first order magnetostructural transition (MST) from paramagnetic (PM) hexagonal to ferromagnetic (FM) orthorhombic structure and as a result, giant MCE is observed in these alloys. In these doped MnNiSi compounds, a remarkable shifting of structural transition temperature from about 1210 K for MnNiSi compound, to lower than 300 K is observed. ΔS_M as large as about 20.6 J kg^{-1} K^{-1} with large RCP ~ 249.2 J/kg is found for the alloy with x = 0.07 due to a magnetic field change of ΔH ~ 50 kOe. A giant value of ΔS_M about 31.1 J kg^{-1} K^{-1} at 281 K with a large RCP of ~ 209.6 J/kg are observed for y = 0.16 alloy due to ΔH ~ 50 kOe. We have also discussed that isotherms should be measured during cooling to estimate the magnetocaloric parameter accurately for these similar types of materials.

We have further investigated the effect of hydrostatic pressure (P) on MCE and the exchange bias (EB) effect in a Co doped $Ni_{45.5}Co_2Mn_{37.5}Sn_{15}$ Heusler alloy. At ambient P, the martensitic transition temperature (T_M) shifts to a lower temperature with a rate of $dT_M/d\mu_0 H$ ~ 3.29 K/T whereas T_M increases rapidly to a higher

temperature with a shift rate of $dT_M/dP \sim 31.90$ K/GPa when P is applied. Hence, first order MST of similar materials can be tuned by applying both the pressure and magnetic field as they influence T_M oppositely. ΔS_M and RCP do not change significantly with applied pressure. EB effect is found to improve with applied pressure. However, the addition of a small amount of Co substituting Ni in NiMnSn-based Heusler alloys enhances ΔS_M value but the appearance of field induced hysteresis across MST reduces the net RCP of that material in higher doping concentrations. Therefore to improve the inverse MCE of Heusler alloys, we have to reduce the hysteresis loss (HL) significantly to make their real use as a refrigerant. For that purpose, we have doped Si in $Ni_{48}Co_{1.5}Mn_{35}Sn_{15.5-x}Si_x$ (x = 0, 1, 2, and 4) Heusler alloys and observed that average HL reduces drastically from 49.7 to 8.6 J/kg with increase in Si substitution from x = 0 to x = 4. T_M reduces with Si content whereas the Curie temperature (T_C) is insensitive to the doping content. ΔS_M is found to reduce with Si content. A maximum net RCP of about 141.8 J/kg due to $\Delta H \sim 50$ kOe is observed for x = 2 alloy. The results indicate that a few amounts of Si substituting main group (p-block) element is an effective way to reduce HL significantly which in turn enhances the effective efficiency of these similar types of materials.

Besides inverse MCE, to improve the conventional MCE of NiMnSn-based Heusler alloys across second order magnetic transition (SOMT), we have explored MCE response and critical exponents in $Mn_{48-x}Fe_xNi_{41}Sn_{11}$ (x = 8.5, 10.5) alloys across second order FM to PM transition at T_C. These alloys exhibit only SOMT and no MSTs are observed. Increase of Fe substituting Mn reduces Mn-Mn antiferromagnetic interaction resulting only austenite phase for $x \geq 8.5$. Second order transition, being continuous, is not associated with any thermal and field induced hysteresis. A reversible ΔS_M of about 1.02 J kg^{-1} K^{-1} with moderate RCP $\sim$ 40.2 J/kg is obtained at 305 K for x = 8.5, due to ΔH of 14 kOe only. The less consumption of energy in the applicability of MCE across SOMT in these materials can make them a good candidate for a magnetic refrigerant. Further, the critical exponents are estimated for both the samples and found to exhibit long range FM ordering in their austenite phase.

List of Publications

Included in this thesis

1. **S. Ghosh**, P. Sen, and K. Mandal, 'Magnetostructural transition and large magnetocaloric effect in $(Mn_{0.6}Fe_{0.4})NiSi_{1-x}Al_x$ (x = 0.06 - 0.08) Alloys' *J. Magn. Magn. Mater.* **500**, 166345 (2020).

2. **S. Ghosh**, A. Ghosh, P. Sen, and K. Mandal, 'Giant room-temperature magnetocaloric effect across magnetostructural transition in $(MnNiSi)_{1-x}(FeCoGa)_x$ alloys' *Phys. Rev. Applied* **14**, 014016 (2020).

3. S. Arumugam, **S. Ghosh**, A. Ghosh, U. Devarajan, M. Kannan, L. Govindaraj, and K. Mandal, 'Effect of hydrostatic pressure on the magnetic, exchange bias and magnetocaloric properties of $Ni_{45.5}Co_2Mn_{37.5}Sn_{15}$' *J. Alloys Compd*. **712**, 714 (2017).

4. **S. Ghosh**, P. Sen, and K. Mandal, 'Effect of Si Doping on Magnetic and Magnetocaloric Properties of Ni–Co–Mn–Sn Alloys' *IEEE Trans. Magn.* **54**, 1 (2018).

5. **S. Ghosh**, A. Ghosh, and K. Mandal, 'Reversible magnetocaloric effect and critical exponent analysis in Mn-Fe-Ni-Sn Heusler alloys' *J. Alloys Compd*. **746**, 200 (2018).

Not included in this thesis

6. S. Samanta, **S. Ghosh**, and K. Mandal, ' Influences of co-doping Fe and Co on magnetocaloric and transport properties in all d-metal Heusler alloys' (*submitted*)

7. **S. Ghosh**, A. Ghosh, P. Sen and K. Mandal, 'Magnetic and Magnetocaloric Properties in $TbCo_2Si_2$ Alloy' *AIP Conference Proceedings* **2265**, 030553 (2020)

8. M. Alam, **S. Ghosh**, and K. Mandal, 'Magnetic and magnetocaloric properties in double perovskite multiferroic Y_2NiMnO_6 nanoparticle' *AIP Conference Proceedings* **2265**, 030592 (2020)

Acknowledgement

Foremost, I would like to express my sincere gratitude to my Ph.D. supervisor *Professor Kalyan Mandal* for his continuous support to carry out my research, for his patience, the valuable discussion, and his humble guidance. He has always motivated me to work hard and encourage me to think about the research plan independently. During the difficulties of any research work, he always makes himself available for the discussion and never says 'tomorrow'. I have learnt from him the basics of research from designing the research plan, to execute that idea, and to present that in a scientific approach. His deep knowledge, invaluable suggestion, and comments influenced me a lot to pursue my research in a smoother way. I am really grateful for his constant inspiration, encouragement, and mental support, without his help it would not be possible to introduce my thesis.

I am thankful to *Dr. Pintu Sen*, *Scientist H*, *Variable Energy Cyclotron Centre (VECC), Kolkata,* for providing the PPMS facility and the help throughout the measurement. I am also grateful to *Dr. Abhijit Saha*, *UGC-DAE Consortium for Scientific Research*, to avail the SQUID facility and my sincere thanks to *Dr. Rajib Mondal* for the help during the measurements. I would like to thank *Prof. S. Arumugam, Bharathidasan University* for the help to measure pressure dependent magnetic measurements.

I am grateful to *S. N. Bose National Centre for Basic Sciences (SNBNCBS), Kolkata*, for providing a beautiful campus with great instrumental facilities and a favorable research environment. I am extremely thankful to the *Council of Scientific and Industrial Research (CSIR), Government of India,* for providing me the financial support (CSIR Award No.: 09/575(0112)/2015-EMR-I) during the tenure of my research work.

I would like to thank all of my lab mates of Magnetism Laboratory: *Madhuri Di*, *Arup Da*, *Rupali Di, Souvanik Da, Mahebub Da, Keshab Da*, *Indranil Da*, *Chaitali Di*, *Deblina Di*, *Dipika, Dipanjan, Priyanka, Anupam, Swarnali* and *Saheli* for their delightful company and the support in various ways. All of them are very cooperative to maintain a good research environment inside the laboratory. Arup Da has helped me a lot from

the beginning of my research. He taught me to prepare samples, measurement, data analysis, to make a habit to survey literature, the basic understanding of an instrument, and many more things. In any difficulties, Arup Da always gave me fruitful suggestions whenever I needed technical or personal assistance. The fun moments spent especially with Mahebub Da, Kesab Da, and Dipanjan inside and outside the lab are always cherishable. Dipika is my batch-mate as well as a good friend of mine. She is very cooperative and her excellent understandings of basic physics helped me to figure out many complications in my research work. Discussion with Jayee di and Saheli helped me a lot to be more precise in my research.

I am extremely grateful to all of my teachers especially, *Satyen Da, Subhasish Sir, Rafizul Sir,* and *Utpal Sir*. Without their constant support from the early stage of my life, it was impossible to initiate the beginning of this wonderful journey. I am also thankful for the support and encouragement to pursue research by *Amrita Di* from Paramparik-The-Tradition and *Monalisa Di* (Postdoctoral researcher, École Polytechnique).

I would like to acknowledge the help and support from the academic section, particularly from Nibedita madam, and the technical cell of our SNB Centre to pursue my research work efficiently.

I am thankful to every colleague in SNB Centre, specially *Supriyo Da, Souvanik Da, Arghya Da, Rakesh Da, Subhasish Da, Mahebub Da, Keshab Da, Subrata Da, Sarowar Da, Mithun Da, Khata Da, Samrat Da, Dipanjan, Santu (Pabi), Shubhrasish, Subhadip, Rafiqul, Prantick, Anupam, Pandya, Biswajit Kumar, Shubham,* for their amazing company in cricket and football. I also want to thank every staff member including cleaners, gardeners, and mess staff for making my stay memorable here.

I want to show my gratitude to my friends Sujay, Sukanta, Chinmoy, Palash Da, Sunil Da, Ranjit, and Joydev who are very supportive and helped me in every possible way. I always love their company.

Finally, I want to express my gratitude to baba, maa (Kartick ch. Ghosh & Lalita Ghosh), and dada (Debabrata) for their sacrifice, moral support, love, affection, and

guidance. Dada always treats me as a friend, and I can share anytime any difficulties either personal or professional with him. Lastly, I find myself blessed to have Satyen Da in my life since childhood.

Subrata Ghosh

S. N. Bose National Centre for Basic Sciences

List of abbreviation:

A_f	Austenite finish temperature
AFM	Antiferromagnetic
AMR	Active Magnetic regenerator
A_S	Austenite start temperature
Dc	Direct current
DSC	Differential Scanning Calorimetry
ΔH	Magnetic field change
ΔS_M	Isothermal magnetic entropy change
ΔT_{ad}	Adiabatic temperature change
ΔT_{hys}	Thermal hysteresis
EAF	Electric arc-melting furnace
EB	Exchange bias
EDAX	Energy dispersive analysis of X-ray
FC	Field cooled
Fcc	Face centered cubic
FM	Ferromagnetic
SEM	Scanning electron microscope
FIMMT	Field induced metamagnetic transition
FWHM	Full width at half maxima
H_C	Coercivity
H_E	Exchange bias field
HF	Heat flow
HL	Hysteresis loss
IMCE	Inverse magnetocaloric effect
MCE	Magnetocaloric effect
M_f	Martensite finish temperature
MR	Magnetic refrigerator
M_S	Martensite start temperature

M_{sat}	Saturation magnetization
M_{sp}	Spontaneous magnetization
MSME	Magnetic shape memory effect
MST	Magnetostructural transition
PPMS	Physical Property Measurement System
PM	Paramagnetic
RCP	Relative cooling power
RE	Rare earth
RT	Room temperature
SEM	Scanning electron microscope
SOMT	Second order magnetic transition
SOPT	Second order phase transition
SQUID	Superconducting quantum interference devices
T_{A}	Martensite to austenite transition temperature
T_{C}	Curie temperature
T_{EB}	Exchange bias blocking temperature
T_{M}	Austenite to martensite transition temperature
T_N	Neel temperature
T_t	Magnetostructural transition temperature
TM	Transition metal
VSM	Vibrating Sample Magnetometer
XRD	X-ray diffraction or diffractometer
ZFC	Zero field cooled

List of symbols:

a	Lattice constant
B	Magnetic flux density
C	Heat capacity
d	Inter-planner spacing
e	Elementary charge (=1.602×10^{-19} C)
e/a	Valence electron concentration
G	Gibb's free energy
g	gyromagnetic ratio
H	Magnetic field
I	Current
k_B	Boltzmann constant (=1.3806488×10^{-23} J/K)
λ	Wave length
M	Magnetization
μ_B	Bohr magnetron (= 9.274096×10^{-24} J/T)
μ_0	Permeability of free space
Δ	Phase shift
Φ	Magnetic flux
R	Resistance
r	Radius
S	Entropy
T	Temperature
t	Time
θ	Angle
V	Voltage

Contents

List of figures:

Chapter 1 | Introduction

This chapter highlights the basic introduction of magnetocaloric effect and its related thermodynamics. Various thermodynamics cycles of Magnetic refrigeration based on magnetocaloric effect are discussed in the present chapter. The motivation behind the present studies of magnetocaloric effect and the general properties of our preferred magnetocaloric materials are presented. A short literature review of magnetocaloric materials based on past research work is represented. This chapter also includes a brief overview of the thesis.

1.1 Preamble

The depletion of natural energy resources and climate changes with unpredictable consequences are two major concerns of the present-day scientific society. Nowadays, a significant part of the research activities is concentrated on overcoming these two challenges. Therefore, in the present scenario, it is important to conduct research on renewable energy resources as well as on technologies that can reduce energy consumption significantly compared to the existing one. Renewable energy resources are related to the conversion of solar energy, wind, hydropower, biomass, and geothermal energy into electric power [1–5].

The total consumption of electricity by the entire world population is approximately 16.38 trillion kWh [5]. A major portion of the electricity is consumed in using cooling devices on a regular basis such as a freezer to store food in a supermarket and home, the air conditioning in private and public buildings, in industrial fields for liquefaction of different kinds of gasses and also in certain medical fields. Conventional vapor compression refrigerators are used for the cooling technology which is bulky, energy inefficient, and contain hazardous gases like chlorofluorocarbon (CFC), hydrochlorofluorocarbon (HCFC) as refrigerant materials that are suspected to deplete the ozone layer of the atmosphere [6]. Though in recent time the previous usage of hazardous gas is replaced by harmless hydrofluorocarbons (HFC) gas, the lower efficiency of conventional gas refrigeration and also the potential for global warming are still concerns. Magnetic refrigeration, one of such energy-efficient and eco-friendly cooling technology based on magnetocaloric effect (MCE), has tremendous potential to replace the conventional gas refrigerators and is expected to be applicable in solid-state-based modern refrigeration devices [7–10]. The energy efficiency of a magnetic refrigerator is predicted to be enhanced up to 30% higher than that of a conventional gas refrigerator [5,7].

The study of magnetic refrigeration based on MCE was first initiated in 1881 by German physicist E. Warburg who observed the heat evolution in Fe under the application of magnetic field [11]. In 1918, Weiss and Piccard measured experimentally

a temperature change in Ni around its Curie temperature due to a change in the magnetic field [12]. The first breakthrough happened in the late 1920s when two scientists Debye in 1926 [13] and Giauque in 1927 [14], independently proposed the processes of adiabatic cooling under field variation. Experimentally, Giauque and MacDougall were the first to demonstrate magnetic cooling in 1933 and they achieved to reach a sub-Kelvin temperature, 0.25 K, by using paramagnetic $Gd(SO_4)_3.8H_2O$ salt as a magnetic refrigerant [15]. In 1976, Brown first designed magnetic refrigeration in a room temperature range [16]. Two breakthroughs occurred in 1997. First, Ames Laboratory in collaboration with the Astronautics Corporation demonstrated a magnetic refrigeration unit which can be operated in room temperature region and is competitive with the vapor compression refrigerators [17]. Another is the discovery of giant MCE in $Gd_5(Si_2Ge_2)$ alloy by Pecharsky and Gschneidner [18]. Since, to find suitable magnetic refrigerant, the MCE properties of various rare earth based materials are investigated [19–34]. Though the rare earth elements associated with large saturation magnetization are found to exhibit excellent magnetocaloric properties, the high cost of the raw materials is the major limitation for the commercial appliance. Subsequently, in recent times, the research on magnetocaloric materials is shifted to the transition metal based alloys to find the promising magnetic refrigerant material with large magnetocaloric properties near room temperature to make the magnetic refrigeration cost-effective [35–54].

In this chapter, we have discussed the basics of the magnetocaloric effect and its related thermodynamics. The advantages of a room temperature magnetic refrigerator based on the magnetocaloric effect over the conventional gas refrigerator in cooling technology are described here. A short literature review of magnetocaloric materials based on past research works is presented. The general properties of our investigated materials, Heusler alloy and Mn*TX* (*T*= Ni, Co, and *X* = Si, Ge) intermetallic compounds and their effectiveness as a magnetic refrigerant are described. This chapter also includes the motivation of the present studies and a brief overview of the thesis.

1.2 Magnetocaloric effect and its thermodynamics

Magnetocaloric effect (MCE) is a magneto-thermodynamic phenomenon that refers to a magnetic material's thermal response when subjected to changes in the magnetic field [7,9]. It is quantified as reversible temperature change (ΔT_{ad}) when the magnetic field is applied to the material adiabatically and if the magnetic field is applied to the material in isothermal condition, it is defined as reversible magnetic entropy change (ΔS_{M}). MCE can be used in refrigeration technology. The magnetocaloric material which exhibits temperature change under varying magnetic field is the most crucial requirement for a Magnetic Refrigeration device. It is worth noting that MCE is an intrinsic property of any magnetic material. However, any magnetic material has two sources of internal energies, the phonon excitation associated with the lattice degree of freedom and the magnetic excitation which is related to spin degrees of freedom. These two degrees of freedom are coupled to each other by spin lattice coupling.

When a ferromagnetic (FM) material is subjected to an external magnetic field adiabatically, it impacts the spin degrees of freedom which results in the alignment of magnetic spins in the direction of the magnetic field. Due to this spin ordering, the magnetic part of entropy reduces as the entropy is a measure of the disorder of a thermodynamic system; a higher order is related to lower entropy and vice versa. If the process is adiabatic, the total entropy of the system is constant. Therefore, to compensate for the reduction in magnetic entropy, the lattice entropy increases so that the total entropy of the system remains constant. As a result, the temperature of the material increases. The more will be the strength of the magnetic field; the change in temperature will be large. Similarly, upon removal of the external magnetic field, the material releases heat. The use of this effect in a magnetic refrigeration cycle is presented schematically in **Fig 1.1**.

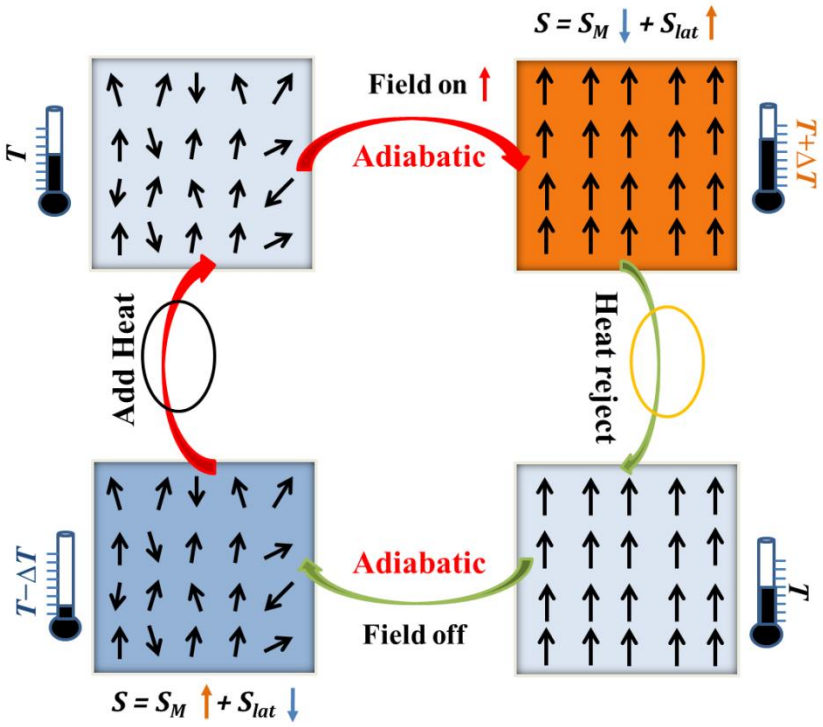

Figure 1.1: Schematic representation of a simple Magnetic Refrigeration cycle. At first, a magnetic field is applied adiabatically resulting, in an increase in the temperature of the material (refrigerant). Heat is removed to the hot reservoir. Magnetic field is removed adiabatically causing a reduction of temperature of the refrigerant material. Heat is added to the material from that has to be cooled (cold reservoir).

The total entropy of a magnetic material can be expressed as follows [55],

$$S(T,H) = S_{\mathrm{M}}(T,H) + S_l(T) + S_e(T) \qquad \textbf{(1.1)}$$

where, $S_{\mathrm{M}}(T,H)$ represents the magnetic part of the entropy which is caused by the ordering of magnetic spin. $S_l(T)$ is the lattice part of the entropy, originates from the vibration of the crystal lattice and $S_e(T)$ is electronic entropy of the material's free electrons. T and H are the temperature and the external magnetic field respectively. The lattice and electronic entropy are assumed to depend only on the temperature and independent of the applied magnetic field whereas; the magnetic entropy depends significantly on the magnetic field as well as temperature.

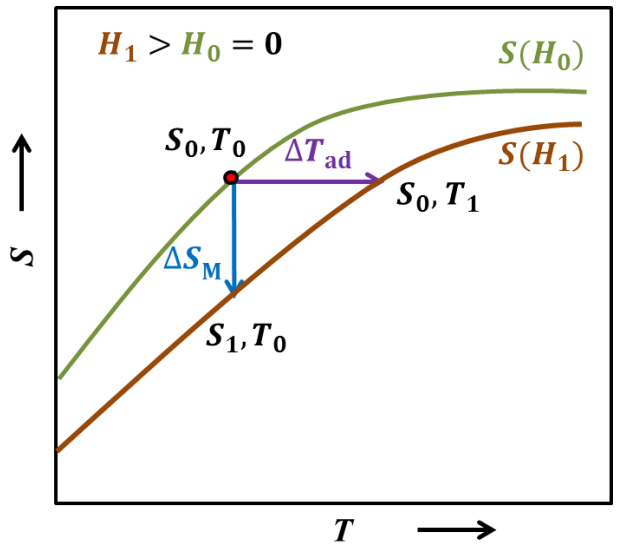

Figure 1.2: Schematic representation of the total entropy as a function of temperature for a ferromagnetic sample under zero field and a non-zero field. Isothermal line shows the decrease of magnetic entropy by ΔS_M due to field change of $\Delta H = H_1 - H_0$ and adiabatic magnetization shows an increase of temperature by ΔT_{ad}.

Figure 1.2 depicts the thermal response of the total entropy (S-T diagram) of a ferromagnetic material in presence of zero and non-zero magnetic field. Two relevant processes are shown in the diagram to understand the thermodynamics of MCE. Firstly when a magnetic field is applied adiabatically (There is no change in entropy i.e. $dS = 0$) in a reversible process, temperature increases which can be visualized from the figure as $\Delta T_{ad}(T, \Delta H) = T_1 - T_0$. Secondly, when the magnetic field is applied in an isothermal condition (T = constant), the total entropy reduces due to a decrease in magnetic contribution. Therefore the magnetic entropy change can be found as $\Delta S_M(T, \Delta H) = S(T_0, H_0) - S(T_0, H_1)$. Both the quantities are a function of initial temperature and the magnetic field change, $\Delta H = H_1 - H_0$.

1.2.1 Thermodynamic relation

If we consider the ferromagnetic sample as a thermodynamic system and the magnetic field is incorporated into the system through the performed magnetic work, the change

in internal energy (dU) can be written using the differential form of the first law of thermodynamics as,

$$\mathrm{d}U = đQ - pdV + \mu_0 H \mathrm{d}M \qquad (\mathbf{1.2})$$

where the total external work performed on the system ($đW$) is the sum of mechanical and the magnetic work ($đW = pdV - \mu_0 H \mathrm{d}M$), Q, the heat flux, p, the pressure and V, the volume of the sample, H, the applied magnetic field, μ_0, the magnetic permeability of free space and M is the magnetization of the sample. đ denotes that heat flux and work are not state functions. For an infinitesimal reversible process, $đQ = T\mathrm{d}S$ (where T, S are the temperature and entropy respectively), equation (**1.2**) can be expressed as,

$$\mathrm{d}U = T\mathrm{d}S - pdV + \mu_0 H \mathrm{d}M \qquad (\mathbf{1.3})$$

where, U is the function of S, V, and M; $U = U(S, V, M)$. Generally, the experiments are carried out in constant pressure while changing the temperature and magnetic field which leads to Gibbs free energy as,

$$G(T, p, H) = U - TS + pV - \mu_0 MH \qquad (\mathbf{1.4})$$

Using the equation (**1.3**), the total differential of $G(T, p, H)$ can be obtained as

$$\mathrm{d}G = -S\mathrm{d}T + V\mathrm{d}p - \mu_0 M \mathrm{d}H \qquad (\mathbf{1.5})$$

Thus, the entropy and magnetization can be evaluated from the above equation as,

$$S = -\left(\frac{\partial G}{\partial T}\right)_{p,H} \text{ and } M = -\frac{1}{\mu_0}\left(\frac{\partial G}{\partial H}\right)_{p,T} \qquad (\mathbf{1.6})$$

If we take the partial differentiation of S with respect to H and of M with respect to T, the equality gives the following Maxwell relation,

$$\left(\frac{\partial S}{\partial H}\right)_{p,T} = \mu_0 \left(\frac{\partial M}{\partial T}\right)_{p,H} \qquad (\mathbf{1.7})$$

If we consider the entropy is a function of T and H, the differential form of entropy at constant pressure can be expressed as,

$$\mathrm{d}S = \left(\frac{\partial S}{\partial T}\right)_{p,H} \mathrm{d}T + \left(\frac{\partial S}{\partial H}\right)_{p,T} \mathrm{d}H \qquad (\mathbf{1.8})$$

For an isothermal process, $\mathrm{d}T = 0$ and using the equation (**1.7**)

$$\mathrm{d}S = \left(\frac{\partial S}{\partial H}\right)_{p,T} \mathrm{d}H = \mu_0 \left(\frac{\partial M}{\partial T}\right)_{p,H} \mathrm{d}H \qquad (\mathbf{1.9})$$

The total isothermal magnetic entropy changes due to magnetic field changes from H_1 to H_2, takes the form:

$$\Delta S_{\mathrm{M}}(T, \Delta H) = \mu_0 \int_{H_1}^{H_2} \left(\frac{\partial M}{\partial T}\right)_{p,H} \mathrm{d}H \qquad (\mathbf{1.10})$$

For an adiabatic process, the total entropy of the system is constant i.e. $\mathrm{d}S = 0$. Therefore from equation (**1.8**), we get,

$$\mathrm{d}T = -\mu_0 \left[\left(\frac{\partial S}{\partial T}\right)_{p,H}\right]^{-1} \left(\frac{\partial M}{\partial T}\right)_{p,H} \mathrm{d}H \qquad (\mathbf{1.11})$$

The heat capacity (C) of the sample is defined as,

$$C_{p,H} = \left(\frac{\mathrm{d}Q}{\mathrm{d}T}\right)_{p.H} = T\left(\frac{\mathrm{d}S}{\mathrm{d}T}\right)_{p.H} \qquad (\mathbf{1.12})$$

Therefore, the equation (**1.11**) modifies as,

$$\mathrm{d}T = -\mu_0 \frac{T}{C_{p,H}} \left(\frac{\partial M}{\partial T}\right)_{p,H} \mathrm{d}H \qquad (\mathbf{1.13})$$

The total adiabatic temperature changes due to a magnetic field changes from H_1 to H_2, takes the form:

$$\Delta T_{\mathrm{ad}}(T, \Delta H) = -\mu_0 \int_{H_1}^{H_2} \frac{T}{C_{p,H}} \left(\frac{\partial M}{\partial T}\right)_{p,H} \mathrm{d}H \qquad (\mathbf{1.14})$$

Equations (**1.10**) and (**1.14**) are used to measure the magnetocaloric properties of any magnetic material experimentally and are well known as Maxwell's equations to determine magnetocaloric parameters $\Delta S_{\mathrm{M}}$and ΔT_{ad} numerically.

1.2.2 Criteria to obtain the large magnetocaloric effect

Magnetocaloric effect, in spite of being an intrinsic property of any magnetic material, we should find out the necessary criteria to achieve large magnetocaloric parameters which may help to select the investigated material and to tune the MCE response further. To find the criteria, we use the Curie-Weiss law for an FM material under the low magnetic field and high temperature condition [56],

$$\chi = \frac{M(T,H)}{H} = \frac{Ng^2\mu_B^2 J(J+1)}{3Ak_B(T-T_C)} \qquad (\mathbf{1.15})$$

where, N, g, μ_B, J, A, k_B & T_c stand for a number of magnetic atoms per unit volume, gyromagnetic ratio, Bohr magneton, total angular momentum quantum number, atomic weight, Boltzmann constant, and Curie temperature respectively.

Differentiating the above equation, we get

$$\left(\frac{\partial M(T,H)}{\partial T}\right)_H = -\frac{Ng^2 J(J+1)\mu_B^2}{3Ak_B(T-T_C)^2} \qquad (\mathbf{1.16})$$

Using the equation (**1.16**), the equation (**1.10**) and (**1.14**) take form as,

$$\Delta S_{\mathrm{M}}(T, \Delta \mathrm{H}) = -\int_{H_1}^{H_2} \frac{Ng^2 J(J+1)\mu_B^2}{3Ak_B(T-T_C)^2}\, dH \qquad (\mathbf{1.17})$$

$$\Delta T_{\mathrm{ad}}(T, \Delta \mathrm{H}) = \int_{H_1}^{H_2} \left(\frac{T}{C(T,H)}\right)_M \frac{Ng^2 J(J+1)\mu_B^2}{3Ak_B(T-T_C)^2}\, dH \qquad (\mathbf{1.18})$$

From the above two equations (**1.17**) and (**1.18**), both the magnetocaloric parameters; isothermal magnetic entropy change, ΔS_{M} and the adiabatic temperature change, ΔT_{ad} varies proportionally to J and $1/(T-T_C)^2$. Therefore, the parameters of

magnetic material are the maximum near its T_C i.e the region close to a phase transition, and also the materials having large J value will be desirable. In this context, rare earth materials are a great choice though their cost is very high. For room temperature (RT) application purposes, the phase transition temperature is preferred to be around RT. Additionally, the specific heat of the material should be low to achieve a large adiabatic temperate change of the material. Also, both the parameters depend on a term $\left(\frac{\partial M}{\partial T}\right)_H$ which signifies that its maximum appears when there is an abrupt change in magnetization. Therefore phase transitions, either of first order or second order type, are desirable which accompanies a significant change in magnetization. Further, from the susceptibility versus temperature curve of a paramagnetic (PM) or a soft FM material [56], susceptibility decreases with an increase in temperature at a constant field i.e. $\left(\frac{\partial M}{\partial T}\right)_H < 0$. If we insert this into equation (**1.10**) and (**1.14**), we see $\Delta S_{\mathrm{M}} < 0$ & $\Delta T_{\mathrm{ad}} > 0$, which is consistent with **Fig. 1.1**.

1.2.3 Conventional and Inverse Magnetocaloric effect

Depending on the sign convention of the magnetocaloric parameters, MCE can be classified into two types; conventional MCE, and inverse MCE. During the phase transition, if the magnetization decreases with an increase in temperature, the change in magnetization with respect to temperature $\left(\frac{\partial M}{\partial T}\right)$ becomes negative (shown in **Fig. 1.3(a)**). Thus, ΔS_{M} is negative and ΔT_{ad} is positive. Therefore, when the magnetic is applied adiabatically, the temperature of the material increases. This is known as conventional MCE. Generally, this type of MCE can be observed across the Curie temperature of FM to PM transition, Neel temperature (T_{N}) of an antiferromagnetic (AFM) to PM transition of a magnetic material.

On the other hand, during a phase transition if the magnetization increases with increasing temperature across the transition temperature, $\frac{\partial M}{\partial T}$ becomes positive (represented in **Fig. 1.3(b)**). Thus, ΔS_{M} is positive and ΔT_{ad} is negative. This means the material releases heat when it is subjected to an external magnetic field in an adiabatic

condition. This is recognized as Inverse MCE. Usually, the materials showing a structural transformation from a weak magnetic structure to a magnetically more favorable structure exhibit Inverse MCE across the transition temperature.

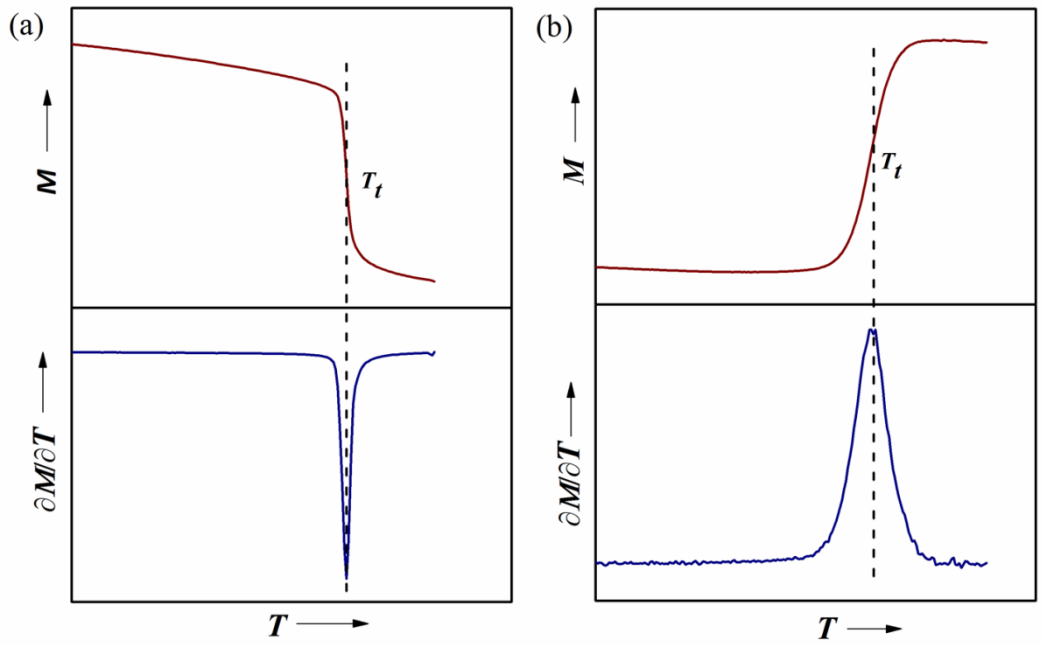

Figure 1.3: Schematic representation of M–T curve showing (a) a magnetic phase transition where M decreases with increase in T and corresponding $\boldsymbol{\partial M/\partial T - T}$ curve and (b) a phase transition where M increases with increase in $\boldsymbol{T}$ and its corresponding $\boldsymbol{\partial M/\partial T - T}$ curve.

1.2.4 Thermodynamic cycles

In the working principle of a magnetic refrigerator (MR), a magnetocaloric material is used as a refrigerant material which absorbs the heat from the load; the cold hot exchanger and rejects the heat to the heat sink; hot exchanger. Due to the cyclic repetition of this process, the load is cooled. MR is very alike to conventional gas refrigeration and the only major distinction is the use of external stimuli to the working material; in the case of gas refrigeration, it is hydrostatic pressure whereas in the case of MR it is the magnetic field. In general, MR consists of a refrigerant (magnetocaloric material), a variable magnetic field generator system, a heat, and cold heat exchangers, a heat transfer system (maybe fluid or a gas depending on the operating temperature).

Additionally, a regenerator, a thermal device, can be used to the device that may transfer the heat between the different parts of the cycle. MR operates using a combination of various thermodynamic processes such as adiabatic, isothermal, and isofield magnetization. There are four main thermodynamic cycles including Carnot, Brayton, Ericsson, Cascade magnetic cycle, and Active Magnetic Regenerator cycle which are used in MR [57,58].

1.1.1.1 Carnot Cycle

In MR cycles, the Carnot cycle is considered as a reference cycle as it involves the magnitude of the magnetocaloric parameters. It is the most efficient thermodynamic cycle between two thermal sources. In general, it consists of two adiabatic and two isothermal processes which are schematically represented by a *T*-*S* diagram in **Fig. 1.4(a)**. Let us consider the temperature of the magnetocaloric material in absence of an applied magnetic field is T_{cold}. Firstly, in the process (A to B), a partial magnetic field is applied to the magnetocaloric material under the adiabatic condition which results in an increase of temperature from T_{cold} to T_{hot}. Next, in the process (B to C), the magnetic field is further applied to magnetize the material completely in isothermal conditions maintaining the temperature T_{hot} of the material. In this process, the magnetic refrigerant exchanges heat with the high temperature sink. After that, in process (C to D) magnetic field is reduced which decreases the temperature of the material from T_{hot} to T_{cold}. At last, in the process (D to A) the magnetic field is reduced further to its initial value under isothermal condition maintaining the temperature T_{cold} of the material. In this process, the magnetic refrigerant material absorbs heat from the low temperature load to compensate for the energy loss during demagnetization. In this cyclic way, the low temperature load is cooled.

1.1.1.2 Brayton Cycle

Figure 1.4(b) depicts the schematic representation of the Brayton cycle through a simple *T*-*S* diagram. It consists of four thermodynamic processes; two adiabatic and two isofield processes. Unlike the Carnot cycle, here a constant magnetic field is applied. It can be assumed that the temperature of the working material is T_1 at the starting point

A while there is no application of a magnetic field. In process (A to B) when a constant magnetic field is subjected to the material adiabatically, the temperature of the material enhances from T_1 to T_1+ΔT. Now, in the isofield process (B to C), the material releases heat to the heat sink through heat transfer fluid which lowers the temperature to T_1. In addition, further cooling can be achieved using a regenerator though it is unnecessary [57]. Next, in the process (C to D), the adiabatic demagnetization causes a reduction of temperature of the material to T_1 to T_1-ΔT. In the last isofield process (D to A), the material takes heat from the low temperature load and reaches the initial temperature T_1. Following this cyclic processes, the load is cooled.

1.1.1.3 Ericsson cycle

The Ericsson cycle is consisted of two isothermal and two isofield thermodynamic processes which are shown by a *T*-*S* diagram in **Fig. 1.4(c)**. In this cycle, regeneration is required. As depicted in the figure, for the process (A to B), the magnetic field is applied to the material in isothermal condition, which reject the heat to the heat sink retaining the material's temperature constant (T_{hot}). Next, in the isofield process (B to C), the regenerator absorbs heat from the material and the temperature falls to T_{hot} to T_{cold}. Subsequently, in the next process (C to D) the demagnetization in isothermal condition absorbs heat from the load to maintain its temperature. Finally, in the process (D to A) regenerator releases heat to the material resulting, an increase of its temperature to its initial temperature T_{hot}. This is the cyclic procedure to cool the load.

1.1.1.4 Cascade Magnetic cycle

In general, the magnetocaloric material exhibits maximum MCE to a peak temperature and at the deviation of that peak temperature, MCE reduces. For a large operation temperature window of magnetic refrigeration, the efficiency reduces, as the peak of MCE decreases. To overcome this situation cascaded magnetic cycle can be used where two or more thermodynamic cycle is cascaded and each cycle accompanies a different refrigerant material with a maximum MCE value at respective peak temperature. In a *T*-*S* diagram, the cascade of two Ericsson cycles is shown schematically in **Fig. 1.4(d)**.

Here cooling power of cycle (i) is used to absorb the energy rejected by cycle (ii). The total work performed in the cascade cycle is the sum of the area covered by these two cycles. As the magnetocaloric material is solid, the same fluid can be transferred to these two cycles. Hence there is no need for heat exchangers between the two sources unlike the conventional one.

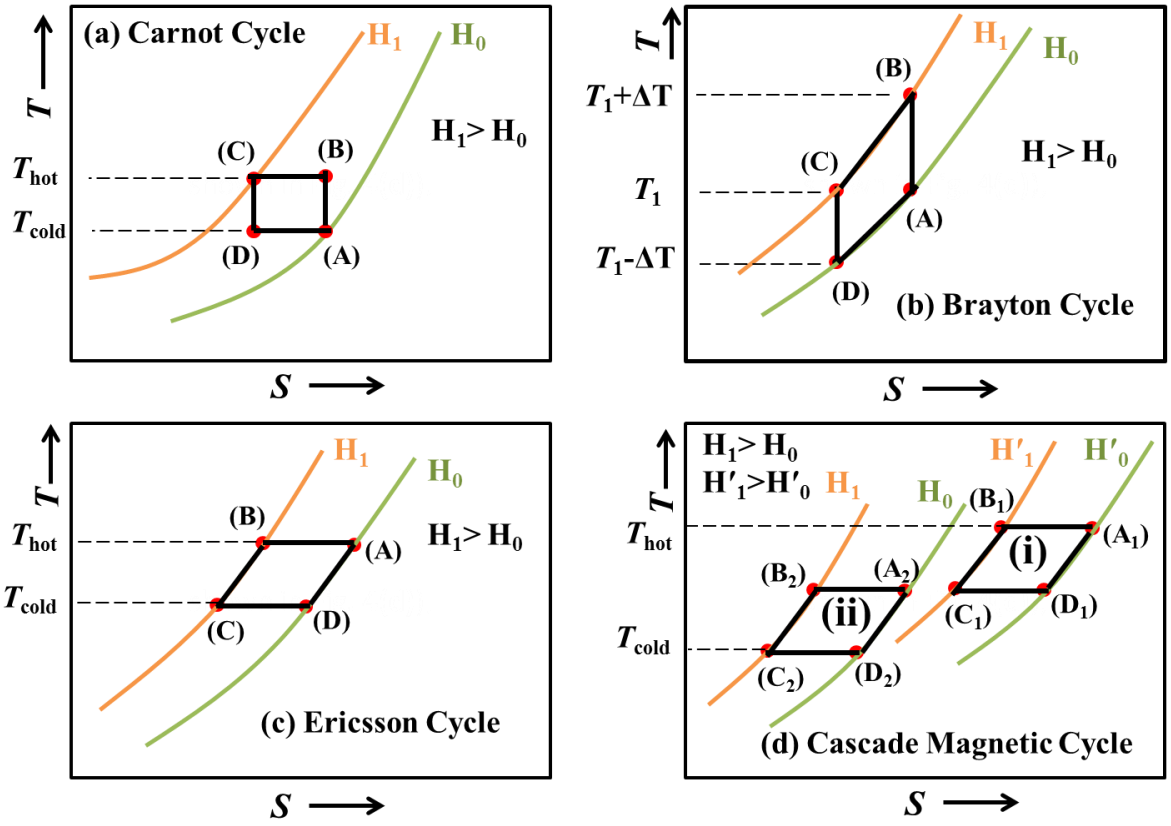

Figure 1.4: *T-S* diagram of thermodynamic (a) Carnot cycle, (b) Brayton cycle, (c) Ericsson cycle, and (d) Cascade magnetic cycle (based on Ericsson cycle) used in Magnetic refrigerator.

1.1.1.5 Active Magnetic Regenerator Cycle

Active magnetic regenerator (AMR) cycle was first introduced by Steyert in 1978 [59]. With the exception of the Carnot cycle, it is considered as the most efficient thermodynamic cycle for magnetic refrigeration when the operating temperature is at room temperature. Here, magnetocaloric material works both as a refrigerant and regenerator. AMR cycle consists of two adiabatic and two isofield processes. As the

refrigerant material is solid, a heat transfer fluid is needed which will connect the refrigerant with the hot and cold heat exchangers, and the refrigerant material is immersed into the fluid. The material is made in contact between the two extreme ends of cold and hot heat exchangers with a temperature gradient. At first, due to adiabatic magnetization, the temperature of the magnetocaloric regenerator material increases which releases heat to the heat transfer fluid in the regenerator and increases its temperature. Now, in the isofield processes, the heat transfer fluid in the regenerator with the fluid coming from the cold heat exchangers absorbs the heat and releases at a higher temperature than that of a heat sink in the hot heat exchangers. Next, in adiabatic demagnetization processes, the temperature of the magnetocaloric material reduces and it absorbs the heat from the heat transfer fluid and lowers its temperature than that of the cold load. At last, in the isofield process, the fluid in the cold heat exchangers takes the heat from the load and increases its temperature to its initial temperature. Thus, the cooling of the load occurs.

1.3 Experimental techniques to measure the magnetocaloric effect

Based on the determination procedure of magnetocaloric parameters, the characterization of MCE is categorized as a direct and indirect method which are described in detail as follows [26,57,60–62].

1.3.1 Direct technique

In the direct method, the adiabatic temperature change of a magnetic material, the utmost straight-forward parameter of MCE can be measured, and hence, no further estimation is required to realize the MCE of a magnetic material [26]. For that, the adiabatic condition of the system is maintained by isolating the material from the surroundings and by using a temperature sensor, in contact with the material, the temperature change can be recorded when the material is subjected to a magnetic field sweeping. Thus, $\Delta T_{\mathrm{ad}}(T, \Delta \mathrm{H})$ would be measured as a function of starting temperature [63–67]. In this technique, the thermal mass of the sample should be

larger than that of the thermal mass of the sample holder for the accurate measurement of the instantaneous temperature change due to field changes.

1.3.2 Indirect technique

The magnetocaloric parameter, ΔS_{M}, is less straight-forward compared to ΔT_{ad} but easy to determine. As the temperature changes of the material are owing to the change in the order of magnetic spin, it can be expected that if the ΔS_{M} becomes large, ΔT_{ad} would be large. In an indirect method, the magnetocaloric parameters are determined following two approaches.

Firstly, the specific heat of the material is measured as a function of temperature in the absence and presence of an applied magnetic field. Thus, the total entropy of the material can be written in zero field and non-zero field as [60],

$$S(T,0) = \int_0^T \frac{C(T,0)}{T}\, dT + S(0,0) \qquad (\mathbf{1.19})$$

$$S(T,H) = \int_0^T \frac{C(T,H)}{T}\, dT + S(0,H) \qquad (\mathbf{1.20})$$

where, $S(0,0)$ and $S(0,H)$ are the entropy in zero field and non-zero field at absolute zero and both are the same for a condensed system. Hence, subtraction of equation (**1.19**) from equation (**1.20**) results,

$$\Delta S_{\mathrm{M}}(T,\Delta H) = \int_0^T \frac{C(T,H)-C(T,0)}{T}\, dT \qquad (\mathbf{1.21})$$

In another way, indirectly ΔS_{M} can be estimated by measuring the isothermal magnetization data at different temperatures across the transition temperature within a small temperature interval (ΔT) and using the numerical approximation of equation (**1.10**) as

$$\Delta S_{\mathrm{M}}(T,\Delta H) = \mu_0 \sum_i \frac{\left(M\left(T+\frac{\Delta T}{2},H_i\right)-M\left(T-\frac{\Delta T}{2},H_i\right)\right)}{\Delta T}\Delta H_i \qquad (\mathbf{1.22})$$

Indirectly, ΔT_{ad} can be evaluated using the field dependent specific heat and ΔS_{M} data as,

$$\Delta T_{ad}(T, \Delta H) = \mu_0 \sum_i \frac{T}{C(T,H_i)} \frac{\left(M\left(T+\frac{\Delta T}{2},H_i\right)-M\left(T-\frac{\Delta T}{2},H_i\right)\right)}{\Delta T} \Delta H_i \qquad (\mathbf{1.22})$$

This method is suitable to measure the magnetocaloric parameters for a continuous phase transition. Generally, the materials exhibiting the first order phase transition (FOPT) are associated with large entropy change compared to the materials showing the second order phase transition (SOPT). In the case of FOPT, the use of these above equation provides an unphysical spike to the $\Delta S_{\mathrm{M}} - T$ curve. In order to get the appropriate results of magnetocaloric parameters, the so-called loop processes are followed to measure the isotherms where during every measurement of *M-H* curve, the material is heated or cooled to the weak magnetic region to remove the field history effect of the sample [68].

1.3.3 Relative Cooling Power

In order to follow the indirect method to explore the MCE of a magnetic material, there is a need of evaluation of another important factor which is referred to as Relative Cooling Power (RCP). RCP is defined as the amount of heat transfer between hot and cold heat reservoirs and it can be calculated numerically using the following equation as [57],

$$\mathrm{RCP} = \left|\Delta S_M^{peak}\right| \Delta T_{FWHM} \qquad (\mathbf{1.23})$$

where, ΔS_M^{peak} is the peak value of ΔS_{M} of $\Delta S_M - T$ curve and ΔT_{FWHM} stands for the temperature span of full width at half maxima of ΔS_M of $\Delta S_{\mathrm{M}} - T$ curve. A promising magnetocaloric material should have a large RCP value, provided the material has sizeable magnetocaloric parameters. Usually, the material associated with FOPT exhibits large magnetic hysteresis losses upon application and removal of an applied magnetic field which will heat up the material. As the purpose is to use the material for

cooling, the hysteresis losses are needed to subtract from the RCP value to obtain its net RCP [10].

1.4 Magnetocaloric Materials

During the last four decades, the magnetocaloric properties of the various types of materials are extensively investigated in search of efficient magnetocaloric material for room temperature magnetic refrigeration. Primarily, the focus was on the rare earth based materials as they are associated with large saturation magnetization and are found to exhibit large MCE across the magnetic transition near room temperature but the cost of the raw materials are high. In order to make the magnetic refrigeration cost-effective, the focus is shifted to the transition metal based alloys which are low-cost materials. In the following section, we have presented a brief review of the investigated magnetocaloric materials so far based on the literature survey. We have also compared the magnetocaloric properties of different types of materials in **Fig. 1.5**.

1.4.1 Rare Earth Containing Materials

Rare earth (RE) metals with localized magnetic moment on rare earth ions have a significantly large value of saturation magnetization. From the pure lanthanide elements, Gd is the only pure RE metal to exhibit a large magnetocaloric effect with ΔS_M about 10 J kg^{-1} K^{-1} near room temperature at $T \sim 294$ K due to the field changes of ΔH = 50 kOe [26]. A certain amount of Nb or Fe addition to Gd enhances considerable MCE response of Gd [57]. Room temperature MCE is also investigated in other Gd-based binary compounds with general formula Gd-M such as $Gd_{0.85}Y_{0.15}$, $Gd_{0.85}Tb_{0.15}$ [69]. Several RE containing materials which can be considered as promising magnetocaloric materials are Laves phases materials, $La(FeSi)_{13}$-based compounds, $Gd_5(Si,Ge)_4$ compounds, $ThCr_2Si_2$-type compounds, ferromagnetic Lanthanum manganite, and other RE containing compounds (**shown in Fig. 1.5**) [26,30–32,57,62]. For instance; In 1997, Pecharsky and Gschneidner reported the giant magnetocaloric effect in $Gd_5Ge_2Si_2$ with magnetocaloric parameters such as $\Delta S_M = 20$ J kg^{-1} K^{-1}, $\Delta T_{ad} \sim 15$ K at peak temperature T = 276 K due to a field change of 50 kOe which is associated with a first

order magnetostructural transition [18]. The intermetallic compound $LaFe_{11.4}Si_{1.6}$, reported by Hu *et al.* in 2001 [70], exhibits giant MCE with $\Delta S_M = 20$ J kg^{-1} K^{-1} at 208 K for ΔH = 50 kOe which is associated with first order itinerant electron metamagnetic transition where a change in unit cell volume about 1% does not change the crystal symmetry .

1.4.2 Transition Metal Based Materials

Considering the cost of the raw materials, RE elements are very high-cost materials though they are very effective as magnetocaloric materials. Therefore, to make the magnetic refrigerant cost-effective, researchers are focused on low-cost transition metal (TM) based alloys. In this regard, Mn-based compounds are the best option, as it possesses maximum magnetization among other TM elements. The MCE response of several Mn-containing materials including Ni-Mn-based Heusler alloys, Mn-Fe-based compounds are explored for this purpose [35–54, 57]. These materials exhibit first order magneto-structural transition with a significant change in magnetization which results in a large MCE response.

1.4.3 Others Materials and Overall Comparison

Besides, the above-mentioned magnetocaloric materials, the MCE response of a few transition metal based amorphous magnetic materials [57,71–74] are investigated in search of promising refrigerant material. An overview of the MCE response of various type of magnetocaloric materials is presented in **Fig. 1.5**, by plotting the absolute value of magnetic entropy changes obtained as a function of the peak temperature where the magnetic entropy change is a maximum.

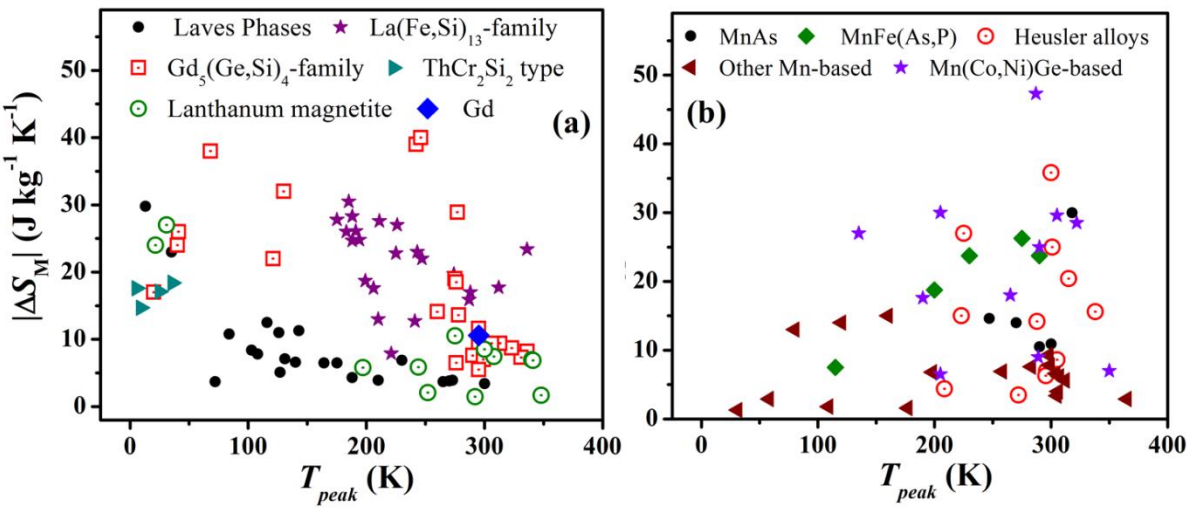

Figure 1.5: Magnetic entropy change vs peak temperature due to field change of 50 kOe for (a) rare earth containing magnetocaloric alloys (b) various transition metal based magnetocaloric materials.

From **Fig. 1.5(a)**, one can observe that Gd based materials exhibit giant magnetocaloric properties around room temperature. Their working temperature ranges from just below the room temperature (~ 300 K) to the lower temperature. The magnetocaloric materials belong to $La(Fe,Si)_{13}$-family are also potential candidates for magnetic refrigerant as they exhibit large magnetocaloric properties at and around room temperature. However, the high cost of the raw materials is a limitation for the usage of these materials in a commercial application. In the case of other rare earth containing magnetocaloric materials, either their peak value of MCE parameter is low or the operating temperature is at very low temperature. Form figure 1.5(b), it can be noticed that Heusler alloy and Mn(Co, Ni)Ge-based materials of Mn*TX* (*T* = Ni, Co, and *X* = Si, Ge) family have the potential to be a suitable refrigerant material as they exhibit giant MCE at and around room temperature. Heusler alloys are also cheap in cost and their transition temperature can be tuned easily around room temperature by changing the element's ration and also by single element substitution. On the other hand, Ge contains in Mn(Co,Ni)Ge-based material will make it a little expensive for magnetic refrigeration. Other materials such as MnAs- and MnFe(As,P)- based materials also show large MCE but these materials contain toxic 'As' element. Considering all the above-mentioned

facts, we have preferred low-cost transition metal based NiMnSn-based Heusler alloys and MnNiSi- based intermetallic compounds from the Mn*TX* (*T* = Ni, Co, and *X* = Si, Ge) family to study their magnetocaloric properties in-detail and to tune their MCE further to establish them as a promising refrigerant material for room temperature magnetic refrigeration technology. The basic properties of Heusler alloys and MnNiSi-based intermetallic compounds are described in the following section.

1.5 Heusler Alloys

Heusler alloys are an interesting class of magnetocaloric material. These are ordered intermetallic compounds with general formula X_2YZ, where three components occupy the crystallographic non-equivalent positions of an $L2_1$ structure. X and Y are the transition metal elements and Z is IIIA-VA group element [75,76]. These materials show magnetism mainly due to X and/or Y elements. The Heusler alloy is named after the German mining engineer and chemist Friedrich Heusler who reported that it is possible to produce a ferromagnetic alloy without using any ferromagnetic constituents and Cu_2MnSn alloy was first reported Heusler alloy in 1903 [75].

Heusler alloy has a cubic $L2_1$ type structure (space group: $Fm\bar{3}m$) which consists of four interpenetrating face centered cubic sub-lattices, shown in **Fig. 1.6(a)**. In the unit cell formed, X atoms take the positions (0, 0, 0) and (½, ½, ½), Y takes (¼, ¼, ¼) site, and Z occupies (¾, ¾, ¾) position. When one site, (½, ½, ½) is vacant, it is recognized as half Heusler alloy which has $C1_b$ crystal structure and is also shown in **Fig. 1.6(b)**. The atoms occupy X sites to Z sites depending on the number of valence electrons present in the atom. The atom containing many numbers of valence electrons occupies the X sites, following the Y and Z positions accordingly. The Heusler alloys in stoichiometric composition show ferromagnetic order. Most of the off-stoichiometric Heusler alloys in a broad composition range and few in stoichiometric ratio undergoes a structural transformation from parent austenite phase (Cubic $L2_1$) to a product martensitic phase (tetragonal or modulated 5M and 7M, where M indicates the monoclinicity arising from the distortion associated with the modulation) during

cooling [62]. Generally, the structural transformation is the first order phase transition which is associated with a thermal hysteresis. The application of a magnetic field to this structural transformation results in significant magnetization changes across the transition. Hence, a large MCE is observed in these alloys and MCE reaches its maximum value when the structural transformation temperature and magnetic transition temperature are close to each other.

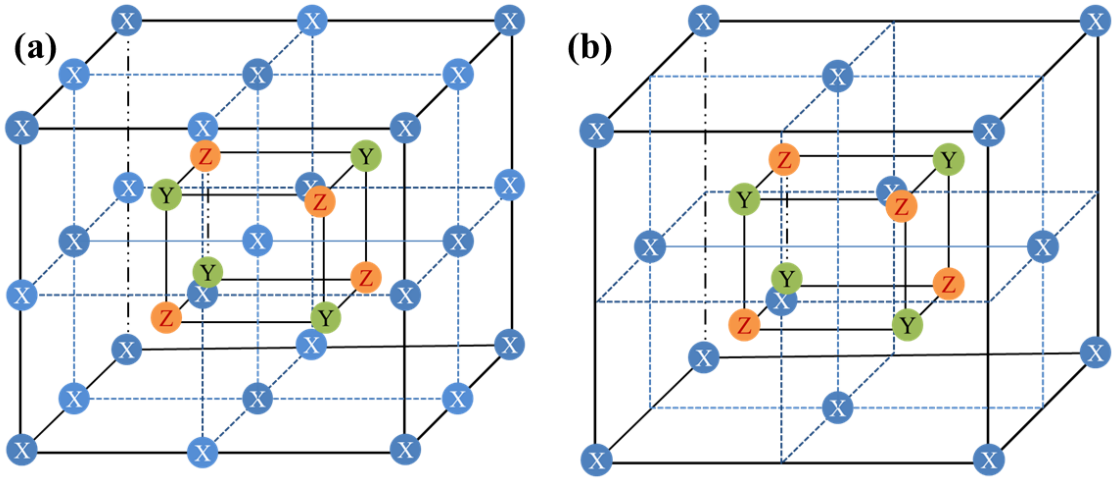

Figure 1.6: Schematic diagram of (a) full Heusler alloy and of (b) half Heusler alloy

1.5.1 Martensitic transformation in Heusler alloy

Martensitic transformations are the first order diffusionless crystallographic phase transformations which are dominated by the strain energy arising from the share like displacement [77]. During transformation, the atoms move less than their interatomic distances by maintaining their local neighborhood, hence there is no long range movement of the atoms. The diffusionless nature of the transformation generates a lattice change in the unit cell, resulting in a lattice distortion in the system. This transformation is induced in the system by mechanical processes or by temperature changes during the cooling process. The martensitic transformation was first observed in quenched steel by Adolf Martens at the end of the 19th century and the low temperature phase was named after the name as 'martensite' whereas, the high

temperature phase 'austenite' is named after Sir William Chandler Roberts-Austen. Generally, Heusler alloys in off-stoichiometry are found to exhibit martensitic transformation from cubic austenite to a tetragonal martensite phase which is a first order phase transition.

One of the characteristic features of the martensitic transformation is the transformation hysteresis. A schematic representation of temperature dependent magnetization curves in a Ni-Mn-based Heusler alloy which undergoes a martensitic transformation is shown in **Fig. 1.7**. Austenite phase is represented as Cubic lattice and the martensite as tetragonal lattice originated from the distortion of austenite. The martensitic transformation from austenite to martensite phase starts at a temperature M_S and finishes at M_f whereas, the reverse transformation from martensite to austenite occurs between A_S and A_f. The martensitic transition temperature is defined as, $T_M = (M_S + M_f)/2$ and the reverse transition temperature is defined as, $T_A = (A_S + A_f)/2$. The separation between T_A and T_M represents the hysteresis width. All the characteristic transitions are labeled in the figure.

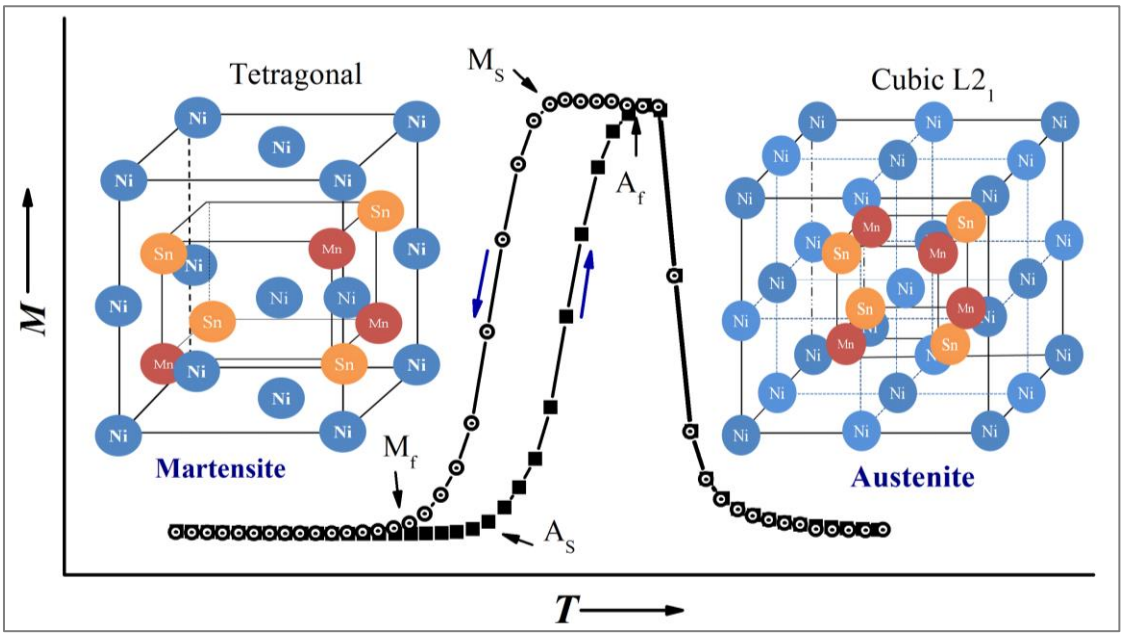

Figure 1.7: Temperature dependent magnetization curve of Ni-Mn-Sn based Heusler alloys exhibiting martensitic transformation

1.5.2 Exchange Bias effect in Heusler alloy

Apart from magnetocaloric properties, Heusler alloys are also found to exhibit an exchange bias (EB) effect in the martensite phase due to the presence of inhomogeneous magnetic phases. The macroscopic observation of the EB effect is the shifting of the magnetization curve from the center of origin. This effect was discovered in fine Cobalt particles coated with cobalt oxide by Meiklejohn and Bean in 1956 [78,79]. EB arises due to the unidirectional anisotropy which develops because of exchange interaction at the common interface of a FM/AFM bilayer. A schematic representation of exchange bias behavior is shown in **Fig. 1.8**. It can be considered, an FM layer is in close contact to an AFM layer and their critical temperature must satisfy the criteria, $T_C > T_N$. At a temperature, in between T_C and T_N, FM spins will be aligned in the direction of the applied magnetic field whereas, AFM spins remains randomly oriented in the PM state. Next, the magnetic field is applied high enough so that FM moments saturate, and in maintaining the constant high magnetic field, the temperature is reduced to a finite temperature which is lower than T_N.

During field cooled processes, because of exchange interaction at the interfaces, the first monolayer of AFM spins orients ferromagnetically following the FM layer. The next monolayer of antiferromagnet spins will align in the opposite order of the previous layer to complete the AFM arrangement and so on. As the AFM spins are uncompensated, there is a net magnetization of this monolayer. It can be assumed that both the monolayers are in a single domain state and will remain in that during remagnetization processes. Now, during reversing the field, the FM spins will rotate oppositely but having coupled with AFM layer, a stronger reversing field is needed to overcome the coupling and to rotate FM spins completely in the opposite direction. As a result, the first coercive field at $T < T_N$ is higher than that of at $T > T_N$. Similarly, on the way back from negative saturation to positive saturation, a smaller external field is necessary to rotate the FM spins in their original direction. Therefore, a shifting of the hysteresis loop is observed in the negative direction, and the displacement of the center of the hysteresis loop is defined as the exchange bias field.

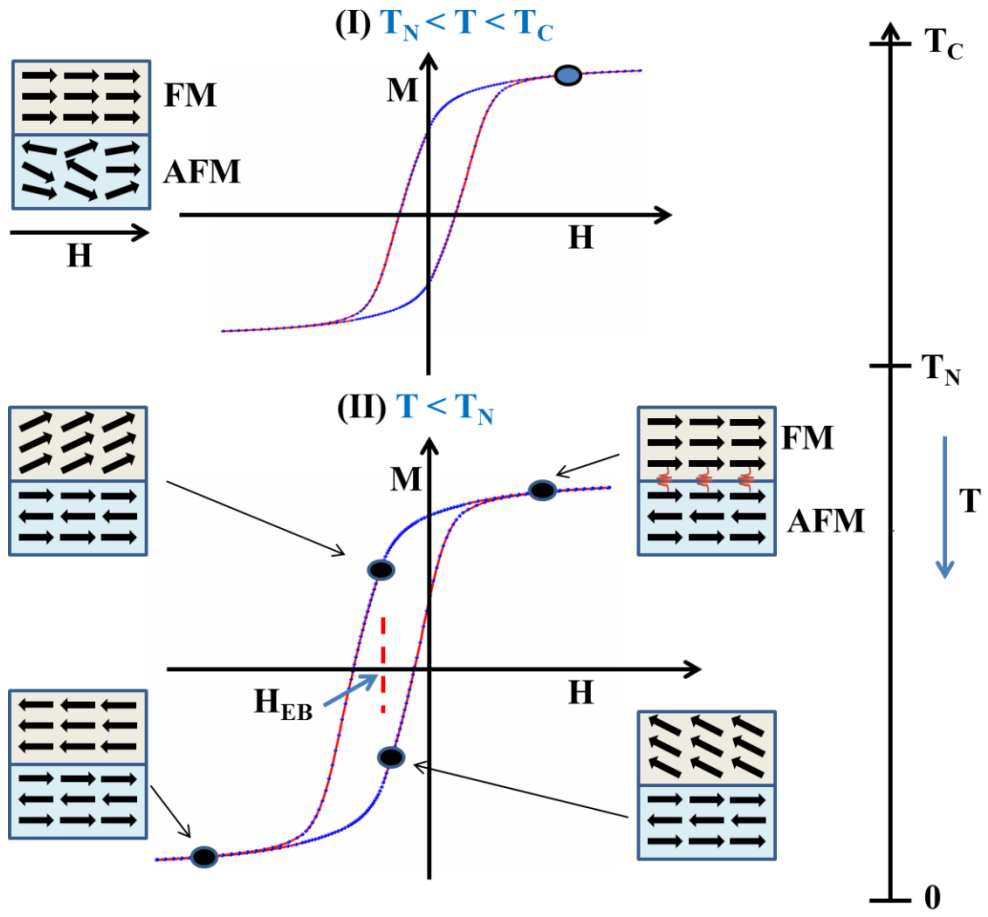

Figure 1.8: Schematic representation of the exchange bias effect which exhibits the shifting of the magnetic hysteresis loop.

EB is generally observed in the system which is containing AFM-FM interfaces such as in small coated particles, inhomogeneous material, and thin film. For Ni-Mn-based Heusler alloys, EB is observed in the martensite phase only [81–83]. EB property has many applications in technological devices including permanent magnets, magnetic recording media, sensors, read heads, and many other devices [84].

1.6 Mn*TX* (*T* = Ni, Co and *X* = Si, Ge) Compounds

The intermetallic compounds with the general formula, Mn*TX* (*T* = Ni, Co, and *X* = Si, Ge), are another important class of magnetocaloric materials. In stoichiometric composition, these materials exhibit a second order magnetic transition followed by a first order structural transformation from low-temperature orthorhombic TiNiSi-type structure (Space group: Pnma) to high-temperature hexagonal Ni_2In-type structure (Space group: $P6_3/mmc$) on heating in the paramagnetic region [46,85–89]. Structural transformation being first order transition, one can expect that there will be a large magnetocaloric effect across the transition temperature but the transformation is occurring in the paramagnetic state, with no significant change in magnetization. It is well known that magnetoresponsive properties including MCE are solely associated with the change in magnetization. Therefore, to make these materials useful for magnetocaloric purposes, the tuning of structural transformation in the ferromagnetic region or coupling it with the magnetic transition at the same temperature near room temperature is the excellent choice. Several strategies such as element substitution, off-stoichiometry, isostructural substitution, heat treatment, or an application of external stimulus like hydrostatic pressure are proposed to obtain coupled magnetostructural transition (MST). Generally, MST is associated with thermal hysteresis which signifies, it is a first order phase transition.

MnNiGe- and MnCoGe- based systems from the above group of intermetallic compounds are extensively studied to obtain MST successfully using the above-mentioned techniques as their closeness of magnetic and structural transition. Stoichiometric MnNiGe [89] exhibits a magnetic transition at a Neel temperature (T_N) of about 346 K and a structural transition at T_M ~ 470 K, whereas stoichiometric MnCoGe [86] undergoes a magnetic transition at the Curie temperature (T_C) of about 355 K and structural transitions at T_M ~ 650 K. Fang *et al.* [90] reported that off-stoichiometric $MnCo_{0.95}Ge_{1.14}$ exhibits a first order magnetostructural transition with a large $|\Delta S_M| = 6.4$ J kg^{-1} K^{-1} for $\Delta H = 10$ kOe at peak temperature T = 331 K. Trung *et al.* [46] discovered the coupled MST and giant MCE near room temperature by addition of few percent interstitials of boron atoms in $MnCoGeB_x$ alloy and they obtained the

optimum $|\Delta S_M| = 47.3$ J kg^{-1} K^{-1} due to $\Delta H = 50$ kOe at T = 287 K for the alloy with x = 0.02. Moreover, by substituting a few percent of V, Cr or Cu in place of Mn, MST with giant MCE is reported for this alloy near room temperature [86,91,92]. In off stoichiometry $Mn_{1.9-x}Ni_xGe$ [93], the structural transition reduces to the lower temperature than that of Curie temperature o Ni_2In phase and shows an optimal ΔS_M = ~27 J kg^{-1} K^{-1} due to $\Delta H = 50$ kOe at about T = 238 K for x = 0.85 which is ascribed to a first order metamagnetic structural transformation from AFM TiNiSi type to FM Ni_2In type structure. By isostructural alloying MnNiGe system with CoNiGe system, a coupled MST with giant MCE ($|\Delta S_M| = 40$ J kg^{-1} K^{-1} due to $\Delta H = 50$ kOe at T = 238 K) was reported by Liu *et al* [94].

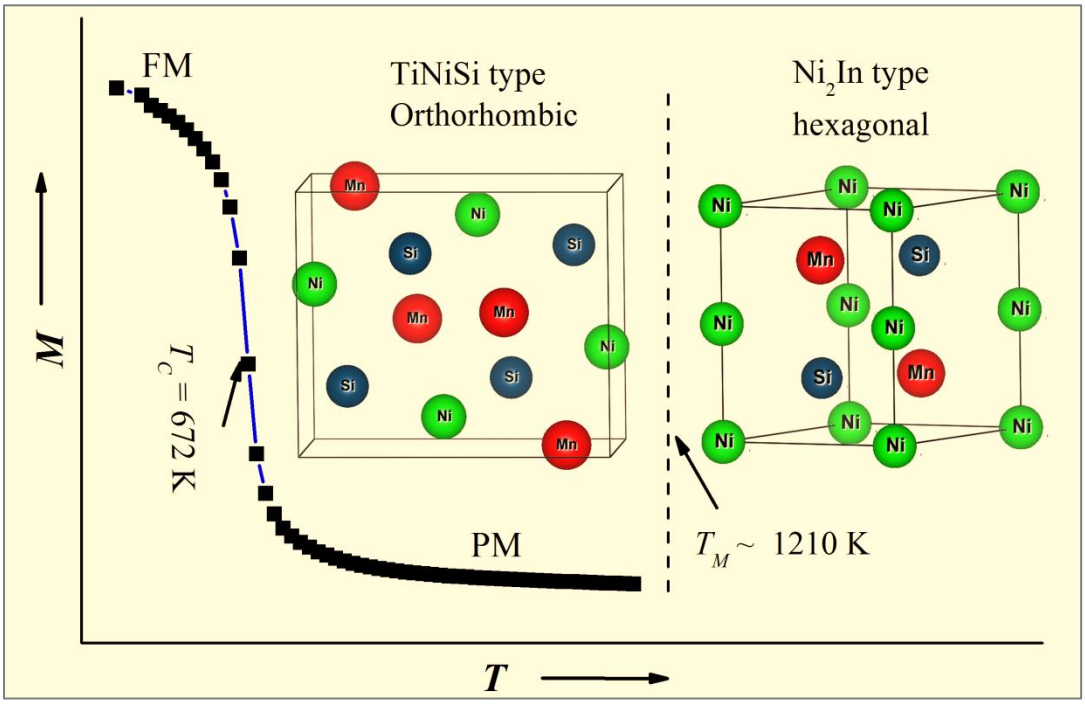

Figure 1.9: Schematic representation of Magnetization vs. Temperature curve of MnNiSi compound exhibiting magnetic transition from FM to PM at T_C ~ 672 K and a structural transformation from TiNiSi type orthorhombic structure to Ni_2In type hexagonal structure at around ~1210 K on heating.

In addition to the above mention system, stoichiometric MnNiSi compound [95] also exhibit a second order FM to PM transition at T_C ~ 622 K and, beyond that temperature, a first order structural transformation from TiNiSi type orthorhombic to Ni_2In-type hexagonal structure at a higher temperature of about T_M ~ 1210 K on heating as presented schematically in **Fig. 1.9**. The lattice parameters of two crystal phases are related as $a_o = c_h, b_o = c_h$, and $c_o = \sqrt{3}a_h$ which leads to the unit cell volume relation as, $V_o = 2V_h$. Here, 'o' and 'h' represent orthorhombic and hexagonal structure respectively. As both the transition temperatures are at higher temperature, it is difficult to obtain MST for this system near room temperature. Considering the cost of the raw materials, this material will be very cost-effective for magnetic refrigeration. Li, *et al*. [88] reported that with the substitution of Co (Fe) in Mn_xNiSi, both the magnetic and structural transition decreases significantly toward room temperature but even after x = 0.5, the structural transformation temperature is in the paramagnetic region and far from the room temperature. Therefore, unlike the above system, in MnNiSi system single element substitution may not be possible to achieve MST. However, by alloying $(MnNiSi)_{1-x}$ with binary compound Fe_2Ge [96], or with a ternary compound like FeNiGe [97] or FeCoGe [98] the MST is successfully obtained near room temperature which results in a giant MCE for this system. For x = 0.35 of Fe_2Ge doping, the maximum value of $|\Delta S_M|$ is 36.9 J kg^{-1} K^{-1} due to $\Delta H = 50$ kOe at peak temperature T = 248 K.

1.7 Motivation of Thesis

If the efficiency of energy conversion can be enhanced by a very small percentage in cooling technology, it will save a huge amount of energy globally and hence, a large commercial and environmental savings. Energy-efficient and environmental friendly magnetic refrigerator based on magnetocaloric effect has enormous potential to replace the conventional gas refrigerator in cooling technology. The parameter which defines the magnetocaloric properties of a material is the isothermal magnetic entropy change or an adiabatic temperature change due to an application of a magnetic field. As the temperature change of the materials is due to change in the order of magnetic moments under the application of magnetic field, it is usual that the material exhibiting large

magnetic entropy change with a wide temperature span across FM to PM transition or at the field induced metamagnetic transition from AFM to FM state with low thermal hysteresis and having low specific heat capacity will be the suitable refrigerant material for a magnetic refrigerator. MCE of a material can be large across a first order MST where both magnetic and structural transitions coincide at the same temperature. For room temperature application of magnetic refrigeration, the temperature span of MCE must be around room temperature. However, to make magnetic refrigerators commercially cost-effective, it essentially requires low-cost earth-abundant materials with giant magnetocaloric properties around room temperature as a refrigerant.

The materials such as $Gd_5Si_2Ge_2$ [18], $La(Fe,Si)_{13}$-based alloys [32], Mn-Fe-based compounds [10], and Ni-Mn-based Heusler alloys [57] are already established as promising refrigerant material because of their excellent MCEs around room temperature. All these alloys exhibit a magnetic field induced structural transition from AFM or PM to FM phase leading to a MST which is associated with a significant change in unit cell volume and a sharp change in magnetization across the phase transition. Now, it is a great challenge to discover such giant magnetocaloric materials with transition metal based, less expensive, nontoxic elements which also exhibits negligible magnetic hysteresis effect.

This thesis focuses mainly on exploring the magnetocaloric properties of transition metal based low-cost alloys made of earth-abundant elements and to tune their MCE further to make them suitable for room temperature magnetic refrigeration. For that purpose, we prefer Ni-Mn-Sn off stoichiometric Heusler alloys [99–101] and MnNiSi-based intermetallic compounds [102,103].

1.8 Organization of thesis

This thesis is divided into 8 charterers. An overview of these chapters is summarized as follows:

In ***Chapter 1***, a brief introduction of the magnetocaloric effect with its thermodynamics and magnetic refrigeration and its importance in cooling technology are described. A literature review of magnetocaloric materials is presented. The general properties of Heusler alloys and MnNiSi-based intermetallic compounds and their effectiveness as magnetic refrigerant materials are discussed. The chapter also includes the motivation of the thesis and the organization of the thesis.

In ***Chapter 2***, we have discussed about the sample preparation, characterization and measurement techniques used in the present studies.

Chapter 3 is devoted to the magnetic and magnetocaloric properties of Al doped $(Mn_{0.6}Fe_{0.4})NiSi_{1-x}Al_x$ (x = 0.06, 0.07) alloys. On doping Al in place of Si, the structural transition temperature is observed to shift to around room temperature (~272 K for x = 0.07) from a high temperature of ~1210 K for MnNiSi system. Here magnetic transition and the structural transition are found to couple into a single first order magnetostructural transition which results in a giant magnetocaloric effect in these alloys.

Chapter 4 is based on in-detail study of magnetocaloric properties in transition metal based $(MnNiSi)_{1-x}(FeCoGa)_x$ (x = 0.15 and 0.16) alloys. Here magnetic and structural transitions are observed to coincide at around room temperature in these alloys which leads to a coupled first order magnetostructural transition from paramagnetic hexagonal to ferromagnetic orthorhombic structure and as a result giant magnetocaloric effect is observed in these alloys. These transition based materials show excellent magnetocaloric effects in a board and tunable temperature region. The alloy with x = 0.16 is found to exhibit isothermal magnetic entropy change as large as ~31.1 J kg^{-1} K^{-1} at 281 K due to field change of 50 kOe. This investigated series of materials will

be a potential magnetic refrigerant for room temperature magnetic refrigeration technology.

Chapter 5 presents the effect of hydrostatic pressure on magnetic, exchange bias, and magnetocaloric properties of $Ni_{45.5}Co_2Mn_{37.5}Sn_{15}$ Heusler alloy. The alloy is found to exhibit a large magnetocaloric effect. We have observed that magnetic field and hydrostatic pressure influence first order magneto structural transition temperature oppositely and hence, fine control of operating temperature in these similar materials is possible for magnetic refrigeration by applying both magnetic field and hydrostatic pressure at a time.

In ***Chapter 6***, we have investigated the magnetic, exchange bias, and magnetocaloric properties of polycrystalline $Ni_{48}Co_{1.5}Mn_{35}Sn_{15.5-x}Si_x$ (x = 0, 1, 2, and 4) Heusler alloys. A few percentages of Si doping in place of post transition element is observed as an effective way to reduce thermal as well as magnetic hysteresis of these alloys.

In ***Chapter 7***, we have focused on the study of reversible magnetocaloric properties and analysis of critical exponents around second order magnetic transition in $Mn_{48-x}Fe_xNi_{41}Sn_{11}$ (x = 8.5, 10.5) Heusler alloys. A moderate magnetic entropy change with large relative cooling power is observed at around room temperature. The evaluated critical exponents suggest that the presence of long range ferromagnetic ordering in their ferromagnetic austenite phase.

Finally, an overall conclusion based on the present studies is presented in ***Chapter 8***. This chapter also includes the scope of future work in this particular field.

References

[1] J. Mohtasham, *Review Article-Renewable Energies*, Energy Procedia **74**, 1289 (2015).

[2] F. Díaz-González, A. Sumper, O. Gomis-Bellmunt, and R. Villafáfila-Robles, *A Review of Energy Storage Technologies for Wind Power Applications*, Renew. Sustain. Energy Rev. **16**, 2154 (2012).

[3] P. A. Owusu and S. Asumadu-Sarkodie, *A Review of Renewable Energy Sources, Sustainability Issues and Climate Change Mitigation*, Cogent Eng. **3**, (2016).

[4] A. Luque, A. Martí, and C. Stanley, *Understanding Intermediate-Band Solar Cells*, Nat. Photonics **6**, 146 (2012).

[5] O. Gutfleisch, M. A. Willard, E. Brück, C. H. Chen, S. G. Sankar, and J. P. Liu, *Magnetic Materials and Devices for the 21st Century: Stronger, Lighter, and More Energy Efficient*, Adv. Mater. **23**, 821 (2011).

[6] A. Cavallini, *Working Fluids for Mechanical Refrigeration-Invited Paper Presented at the 19th International Congress of Refrigeration, The Hague, August 1995*, Int. J. Refrig. **19**, 485 (1996).

[7] K. A. GschneidnerJr, V. K. Pecharsky, and A. O. Tsokol, *Recent Developments in Magnetocaloric Materials*, Reports Prog. Phys. **68**, 1479 (2005).

[8] A. Smith, C. R. H. Bahl, R. Bjørk, K. Engelbrecht, K. K. Nielsen, and N. Pryds, *Materials Challenges for High Performance Magnetocaloric Refrigeration Devices*, Adv. Energy Mater. **2**, 1288 (2012).

[9] L. Mañosa and A. Planes, *Materials with Giant Mechanocaloric Effects: Cooling by Strength*, Adv. Mater. **29**, 1603607 (2017).

[10] O. Gutfleisch, T. Gottschall, M. Fries, D. Benke, I. Radulov, K. P. Skokov, H. Wende, M. Gruner, M. Acet, P. Entel, and M. Farle, *Mastering Hysteresis in Magnetocaloric Materials*, Philos. Trans. R. Soc. A **374**, 20150308 (2016).

[11] E. Warburg, *Magnetische Untersuchungen*, Ann. Phys. **249**, 141 (1881).

[12] M. . Kuz'min and A. . Tishin, *Magnetocaloric Effect. Part 1: An Introduction to Various Aspects of Theory and Practice*, Cryogenics (Guildf). **32**, 545 (1992).

[13] P. Debye, *Einige Bemerkungen Zur Magnetisierung Bei Tiefer Temperatur*, Ann. Phys. **386**, 1154 (1926).

[14] W. F. Giauque, *A THERMODYNAMIC TREATMENT OF CERTAIN MAGNETIC EFFECTS. A PROPOSED METHOD OF PRODUCING TEMPERATURES CONSIDERABLY BELOW 1° ABSOLUTE*, J. Am. Chem. Soc. **49**, 1864 (1927).

[15] W. F. Giauque and D. P. MacDougall, *Attainment of Temperatures Below 1° Absolute by Demagnetization of $Gd_2(SO_4)_{3.8}H_2O$*, Phys. Rev. **43**, 768 (1933).

[16] G. V. Brown, *Magnetic Heat Pumping near Room Temperature*, J. Appl. Phys. **47**, 3673 (1976).

[17] C. Zimm, A. Jastrab, A. Sternberg, V. Pecharsky, K. Gschneidner, M. Osborne, and I. Anderson, *Description and Performance of a Near-Room Temperature Magnetic Refrigerator*, in *Advances in Cryogenic Engineering*, Vol. 43 (Springer US, Boston, MA, 1998), pp. 1759–1766.

[18] V. K. Pecharsky and K. A. Gschneidner, Jr., *Giant Magnetocaloric Effect in $Gd_5(Si_2Ge_2)$*, Phys. Rev. Lett. **78**, 4494 (1997).

[19] R. D. Shull, V. Provenzano, A. J. Shapiro, A. Fu, M. W. Lufaso, J. Karapetrova, G. Kletetschka, and V. Mikula, *The Effects of Small Metal Additions (Co,Cu,Ga,Mn,Al,Bi,Sn) on the Magnetocaloric Properties of the $Gd_5Ge_2Si_2$ Alloy*, J. Appl. Phys. **99**, 08K908 (2006).

[20] M. Halder, S. M. Yusuf, M. D. Mukadam, and K. Shashikala, *Magnetocaloric Effect and Critical Behavior near the Paramagnetic to Ferrimagnetic Phase Transition Temperature $InTbCo_{2-x}Fe_x$*, Phys. Rev. B **81**, 174402 (2010).

[21] W. Wu, A. O. Tsokol, K. A. Gschneidner, and J. A. Sampaio, *Influence of Oxygen on the Giant Magnetocaloric Effect of $Gd_5Si_{1.95}Ge_{2.05}$*, J. Alloys Compd. **403**, 118 (2005).

[22] D. K. Xiong, D. Li, W. Liu, and Z. D. Zhang, *Magnetocaloric Effect of Gd(FexAl1−x)2 Compounds*, Phys. B Condens. Matter **369**, 273 (2005).

[23] V. K. Pecharsky and K. A. Gschneidner, *Effect of Alloying on the Giant Magnetocaloric Effect of $Gd_5(Si_2Ge_2)$*, J. Magn. Magn. Mater. **167**, L179 (1997).

[24] L. Li, K. Nishimura, D. Tamei, and K. Mori, *Structure, Transport Properties and the Magnetocaloric Effect in $Gd(Co_{1-x}Ni_x)_2$ Pseudobinary Compounds*, Solid State

Commun. **145**, 427 (2008).

[25] Z. Gu, B. Zhou, J. Li, W. Ao, G. Cheng, and J. Zhao, *Magnetocaloric Effect of $GdCo_{2-x}Al_x$ Compounds*, Solid State Commun. **141**, 548 (2007).

[26] K. A. Gschneidner and V. K. Pecharsky, *Magnetocaloric Materials*, Annu. Rev. Mater. Sci. **30**, 387 (2000).

[27] V. K. Pecharsky and K. A. Gschneidner, *Tunable Magnetic Regenerator Alloys with a Giant Magnetocaloric Effect for Magnetic Refrigeration from ~20 to ~290 K*, Appl. Phys. Lett. **70**, 3299 (1997).

[28] V. Paul-Boncour and T. Mazet, *Investigation of Compounds for Magnetocaloric Applications: $YFe_2H_{4.2}$, $YFe_2D_{4.2}$, and $Y_{0.5}Tb_{0.5}Fe_2D_{4.2}$*, J. Appl. Phys. **105**, 013914 (2009).

[29] J. Q. Li, W. A. Sun, Y. X. Jian, Y. H. Zhuang, W. D. Huang, and J. K. Liang, *The Giant Magnetocaloric Effect of $Gd_5Si_{1.95}Ge_{2.05}$ Enhanced by Sn Doping*, J. Appl. Phys. **100**, 073904 (2006).

[30] M.-H. Phan and S.-C. Yu, *Review of the Magnetocaloric Effect in Manganite Materials*, J. Magn. Magn. Mater. **308**, 325 (2007).

[31] B. G. Shen, J. R. Sun, F. X. Hu, H. W. Zhang, and Z. H. Cheng, *Recent Progress in Exploring Magnetocaloric Materials*, Adv. Mater. **21**, 4545 (2009).

[32] L. Jia, J. R. Sun, J. Shen, Q. Y. Dong, J. D. Zou, B. Gao, T. Y. Zhao, H. W. Zhang, F. X. Hu, and B. G. Shen, *Magnetocaloric Effects in the $La(Fe,Si)_{13}$ Intermetallics Doped by Different Elements*, J. Appl. Phys. **105**, 7 (2009).

[33] B. Podmiljšak, P. McGuiness, B. Miklavič, K. Ž. Rožman, and S. Kobe, *Magnetocaloric Properties and Nanoscale Structure of Fe-Doped $Gd_5Ge_2Si_2$ Alloys*, J. Appl. Phys. **105**, 47 (2009).

[34] E. Yüzüak, I. Dincer, and Y. Elerman, *Magnetocaloric Properties of the $Gd_5Si_{2.05-x}Ge_{1.95-x}Mn_{2x}$ Compounds*, J. Rare Earths **28**, 477 (2010).

[35] T. Krenke, E. Duman, M. Acet, E. F. Wassermann, X. Moya, L. Manosa, and A. Planes, *Inverse Magnetocaloric Effect in Ferromagnetic Ni-Mn-Sn Alloys*, Nat. Mater. **4**, 450 (2005).

[36] R. Sahoo, A. K. Nayak, K. G. Suresh, and A. K. Nigam, *Effect of Fe Substitution on the Magnetic, Transport, Thermal and Magnetocaloric Properties in $Ni_{50}Mn_{38-x}Fe_xSb_{12}$ Heusler Alloys*, J. Appl. Phys. **109**, 123904 (2011).

[37] A. Ghosh and K. Mandal, *Effect of Structural Disorder on the Magnetocaloric Properties of Ni-Mn-Sn Alloy*, Appl. Phys. Lett. **104**, 031905 (2014).

[38] A. Ghosh, P. Sen, and K. Mandal, *Measurement Protocol Dependent Magnetocaloric Properties in a Si-Doped Mn-Rich Mn-Ni-Sn-Si off-Stoichiometric Heusler Alloy*, J. Appl. Phys. **119**, 183902 (2016).

[39] E. Yüzüak, I. Dincer, Y. Elerman, A. Auge, N. Teichert, and A. Hütten, *Inverse Magnetocaloric Effect of Epitaxial Ni-Mn-Sn Thin Films*, Appl. Phys. Lett. **103**, 222403 (2013).

[40] J. Liu, T. Gottschall, K. P. Skokov, J. D. Moore, and O. Gutfleisch, *Giant Magnetocaloric Effect Driven by Structural Transitions*, Nat. Mater. **11**, 620 (2012).

[41] T. Krenke, E. Duman, M. Acet, E. F. Wassermann, X. Moya, L. Mañosa, A. Planes, E. Suard, and B. Ouladdiaf, *Magnetic Superelasticity and Inverse Magnetocaloric Effect in Ni-Mn-In*, Phys. Rev. B **75**, 104414 (2007).

[42] D. Cong, W. Xiong, A. Planes, Y. Ren, L. Mañosa, P. Cao, Z. Nie, X. Sun, Z. Yang, X. Hong, and Y. Wang, *Colossal Elastocaloric Effect in Ferroelastic Ni-Mn-Ti Alloys*, Phys. Rev. Lett. **122**, 255703 (2019).

[43] A. Taubel, T. Gottschall, M. Fries, S. Riegg, C. Soon, K. P. Skokov, and O. Gutfleisch, *A Comparative Study on the Magnetocaloric Properties of Ni-Mn-X(-Co) Heusler Alloys*, Phys. Status Solidi **255**, 1700331 (2018).

[44] C. L. Zhang, Y. G. Nie, H. F. Shi, E. J. Ye, J. Q. Zhao, Z. D. Han, H. C. Xuan, and D. H. Wang, *Tunable Magnetostructural Coupling and Large Magnetocaloric Effect in $Mn_{1-x}Ni_{1-x}Fe_{2x}Si_{1-x}Ga_x$*, J. Magn. Magn. Mater. **432**, 527 (2017).

[45] C. L. Zhang, H. F. Shi, E. J. Ye, Y. G. Nie, Z. D. Han, and D. H. Wang, *Magnetostructural Transition and Magnetocaloric Effect in MnCoGe–NiCoGe System*, J. Alloys Compd. **639**, 36 (2015).

[46] N. T. Trung, L. Zhang, L. Caron, K. H. J. Buschow, and E. Brück, *Giant Magnetocaloric Effects by Tailoring the Phase Transitions*, Appl. Phys. Lett. **96**, 172504 (2010).

[47] K. Mandal, D. Pal, N. Scheerbaum, J. Lyubina, and O. Gutfleisch, *Magnetocaloric Effect in Ni-Mn-Ga Alloys*, in *IEEE Transactions on Magnetics*, Vol. 44 (2008), pp. 2993–2996.

[48] K. Mandal, D. Pal, N. Scheerbaum, J. Lyubina, and O. Gutfleisch, *Effect of Pressure on the Magnetocaloric Properties of Nickel-Rich Ni–Mn–Ga Heusler Alloys*, J. Appl. Phys. **105**, 073509 (2009).

[49] T. Krenke, E. Duman, M. Acet, X. Moya, L. Mañosa, and A. Planes, *Effect of Co and Fe on the Inverse Magnetocaloric Properties of Ni-Mn-Sn*, J. Appl. Phys. **102**, 033903 (2007).

[50] R. Das, S. Sarma, A. Perumal, and A. Srinivasan, *Effect of Co and Cu Substitution on the Magnetic Entropy Change in $Ni_{46}Mn_{43}Sn_{11}$ Alloy*, J. Appl. Phys. **109**, 07A901 (2011).

[51] P. A. Bhobe, K. R. Priolkar, and A. K. Nigam, *Room Temperature Magnetocaloric Effect in Ni–Mn–In*, Appl. Phys. Lett. **91**, 242503 (2007).

[52] I. Babita, S. I. Patil, and S. Ram, *First Order Structural Transformation and Inverse Magnetocaloric Effect in Melt-Spun Ni–Mn–Sn Ribbons*, J. Phys. D. Appl. Phys. **43**, 205002 (2010).

[53] A. Ghosh and K. Mandal, *Large Magnetic Entropy Change and Magnetoresistance Associated with a Martensitic Transition of Mn-Rich $Mn_{50.5-x}Ni_{41}Sn_{8.5+x}$ Alloys*, J. Phys. D. Appl. Phys. **46**, 435001 (2013).

[54] A. Ghosh and K. Mandal, *Large Inverse Magnetocaloric Effect in $Ni_{48.5-x}CoMn_{37}Sn_{14.5}$ (x= 0, 1 and 2) with Negligible Hysteresis*, J. Alloys Compd. **579**, 295 (2013).

[55] A. M. Tishin and Y. I. Spichkin, *The Magnetocaloric Effect and Its Applications - Series in Condensed Matter Physics*, in (2003), pp. 1–475.

[56] C. Kittel, *Introduction to Solid State Physics 7th Edition- Kittel, Charles*, in *John Wiley & Sons* (1996).

[57] V. Franco, J. S. Blázquez, J. J. Ipus, J. Y. Law, L. M. Moreno-Ramírez, and A. Conde, *Magnetocaloric Effect: From Materials Research to Refrigeration Devices*, Prog. Mater. Sci. **93**, 112 (2018).

[58] J. Romero Gómez, R. Ferreiro Garcia, A. De Miguel Catoira, and M. Romero Gómez,

Magnetocaloric Effect: A Review of the Thermodynamic Cycles in Magnetic Refrigeration, Renew. Sustain. Energy Rev. **17**, 74 (2013).

[59] W. A. Steyert, *Stirling-cycle Rotating Magnetic Refrigerators and Heat Engines for Use near Room Temperature*, J. Appl. Phys. **49**, 1216 (1978).

[60] V. Pecharsky, K. Gschneidner, A. Pecharsky, and A. Tishin, *Thermodynamics of the Magnetocaloric Effect*, Phys. Rev. B **64**, 144406 (2001).

[61] V. K. Pecharsky and K. A. Gschneidner, *Magnetocaloric Effect from Indirect Measurements: Magnetization and Heat Capacity*, J. Appl. Phys. **86**, 565 (1999).

[62] V. Franco, J. S. Blázquez, B. Ingale, and A. Conde, *The Magnetocaloric Effect and Magnetic Refrigeration near Room Temperature: Materials and Models*, Annu. Rev. Mater. Res. **42**, 305 (2012).

[63] L. Tocado, E. Palacios, and R. Burriel, *Direct Measurement of the Magnetocaloric Effect In* $Tb_5Si_2Ge_2$, J. Magn. Magn. Mater. **290**–**291**, 719 (2005).

[64] S. Y. Dan'kov, A. M. Tishin, V. K. Pecharsky, and K. A. Gschneidner, *Experimental Device for Studying the Magnetocaloric Effect in Pulse Magnetic Fields*, Rev. Sci. Instrum. **68**, 2432 (1997).

[65] F. Canepa, S. Cirafici, M. Napoletano, C. Ciccarelli, and C. Belfortini, *Direct Measurement of the Magnetocaloric Effect of Microstructured Gd Eutectic Compounds Using a New Fast Automatic Device*, Solid State Commun. **133**, 241 (2005).

[66] K. A. Gschneidner and V. K. Pecharsky, *Magnetocaloric Materials*, Annu. Rev. Mater. Sci. **30**, 387 (2000).

[67] A. Giguère, M. Foldeaki, B. Ravi Gopal, R. Chahine, T. K. Bose, A. Frydman, and J. A. Barclay, *Direct Measurement of the "Giant" Adiabatic Temperature Change in* $Gd_5Si_2Ge_2$, Phys. Rev. Lett. **83**, 2262 (1999).

[68] L. Caron, Z. Q. Ou, T. T. Nguyen, D. T. Cam Thanh, O. Tegus, and E. Brück, *On the Determination of the Magnetic Entropy Change in Materials with First-Order Transitions*, J. Magn. Magn. Mater. **321**, 3559 (2009).

[69] Y. Shao, J. Zhang, J. K. L. Lai, and C. H. Shek, *Magnetic Entropy in Nanocomposite Binary Gadolinium Alloys*, J. Appl. Phys. **80**, 76 (1996).

[70] F. Hu, B. Shen, J. Sun, Z. Cheng, G. Rao, and X. Zhang, *Influence of Negative Lattice Expansion and Metamagnetic Transition on Magnetic Entropy Change in the Compound $LaFe_{11.4}Si_{1.6}$*, Appl. Phys. Lett. **78**, 3675 (2001).

[71] F. Johnson and R. D. Shull, *Amorphous-FeCoCrZrB Ferromagnets for Use as High-Temperature Magnetic Refrigerants*, J. Appl. Phys. **99**, 08K909 (2006).

[72] R. Caballero-Flores, V. Franco, A. Conde, K. E. Knipling, and M. A. Willard, *Influence of Co and Ni Addition on the Magnetocaloric Effect in $Fe_{88-2x}Co_xNi_xZr_7B_4Cu_1$ Soft Magnetic Amorphous Alloys*, Appl. Phys. Lett. **96**, 182506 (2010).

[73] Y. K. Fang, C. C. Yeh, C. C. Hsieh, C. W. Chang, H. W. Chang, W. C. Chang, X. M. Li, and W. Li., *Magnetocaloric Effect in Fe–Zr–B–M (M=Mn, Cr, and Co) Amorphous Systems*, J. Appl. Phys. **105**, 07A910 (2009).

[74] S. G. Min, K. S. Kim, S. C. Yu, Y. C. Kim, K. Y. Kim, K. W. Lee, J. R. Rhee, S. Y. Cha, and Y. S. Kim, *The Magnetic Entropy Change on Amorphous FeMnZr Alloys*, J. Magn. Magn. Mater. **310**, 2820 (2007).

[75] T. Graf, C. Felser, and S. S. P. Parkin, *Simple Rules for the Understanding of Heusler Compounds*, Prog. Solid State Chem. **39**, 1 (2011).

[76] A. Planes, L. Mañosa, and M. Acet, *Magnetocaloric Effect and Its Relation to Shape-Memory Properties in Ferromagnetic Heusler Alloys*, J. Phys. Condens. Matter **21**, 233201 (2009).

[77] F. E. Wang, S. J. Pickart, and H. A. Alperin, *Mechanism of the TiNi Martensitic Transformation and the Crystal Structures of TiNi-II and TiNi-III Phases*, J. Appl. Phys. **43**, 97 (1972).

[78] W. H. Meiklejohn and C. P. Bean, *New Magnetic Anisotropy*, Phys. Rev. **105**, 904 (1957).

[79] W. H. Meiklejohn and C. P. Bean, *New Magnetic Anisotropy*, Phys. Rev. **102**, 1413 (1956).

[80] Florin Radu, Fundamental Aspects of Exchange Bias Effect in AF / F Bilayers and Multilayers, 2005.

[81] M. Khan, I. Dubenko, S. Stadler, and N. Ali, *Exchange Bias in Bulk Mn Rich Ni–Mn–Sn Heusler Alloys*, J. Appl. Phys. **102**, 113914 (2007).

[82] A. K. Nayak, K. G. Suresh, and a. K. Nigam, *Observation of Enhanced Exchange Bias Behavior in NiCoMnSb Heusler Alloys*, J. Phys. D. Appl. Phys. **42**, 115004 (2010).

[83] H. C. Xuan, Q. Q. Cao, C. L. Zhang, S. C. Ma, S. Y. Chen, D. H. Wang, and Y. W. Du, *Large Exchange Bias Field in the Ni–Mn–Sn Heusler Alloys with High Content of Mn*, Appl. Phys. Lett. **96**, 202502 (2010).

[84] J. Nogués and I. K. Schuller, *Exchange Bias*, J. Magn. Magn. Mater. **192**, 203 (1999).

[85] T. Samanta, I. Dubenko, A. Quetz, S. Temple, S. Stadler, and N. Ali, *Magnetostructural Phase Transitions and Magnetocaloric Effects in MnNiGe 1–x Al X*, Appl. Phys. Lett. **100**, 052404 (2012).

[86] S. C. Ma, Y. X. Zheng, H. C. Xuan, L. J. Shen, Q. Q. Cao, D. H. Wang, Z. C. Zhong, and Y. W. Du, *Large Roomtemperature Magnetocaloric Effect with Negligible Magnetic Hysteresis Losses in Mn1–xVxCoGe Alloys*, J. Magn. Magn. Mater. **324**, 135 (2012).

[87] E. Liu, W. Wang, L. Feng, W. Zhu, G. Li, J. Chen, H. Zhang, G. Wu, C. Jiang, H. Xu, and F. de Boer, *Stable Magnetostructural Coupling with Tunable Magnetoresponsive Effects in Hexagonal Ferromagnets*, Nat. Commun. **3**, 873 (2012).

[88] Y. Li, Z. Y. Wei, E. K. Liu, G. D. Liu, S. G. Wang, W. H. Wang, and G. H. Wu, *Structural Transitions, Magnetic Properties, and Electronic Structures of Co(Fe)-Doped MnNiSi Compounds*, J. Appl. Phys. **117**, 17C117 (2015).

[89] W. Bazela, A. Szytuła, J. Todorović, Z. Tomkowicz, and A. Zięba, *Crystal and Magnetic Structure of NiMnGe*, Phys. Status Solidi **38**, 721 (1976).

[90] Y. K. Fang, C. C. Yeh, C. W. Chang, W. C. Chang, M. G. Zhu, and W. Li, *Large Low-Field Magnetocaloric Effect in $MnCo_{0.95}Ge_{1.14}$ Alloy*, Scr. Mater. **57**, 453 (2007).

[91] N. T. Trung, V. Biharie, L. Zhang, L. Caron, K. H. J. Buschow, and E. Brück, *From Single- to Double-First-Order Magnetic Phase Transition in Magnetocaloric $Mn_{1-x}Cr_xCoGe$ Compounds*, Appl. Phys. Lett. **96**, 162507 (2010).

[92] T. Samanta, I. Dubenko, A. Quetz, S. Stadler, and N. Ali, *Giant Magnetocaloric Effects near Room Temperature in $Mn_{1-x}Cu_xCoGe$*, Appl. Phys. Lett. **101**, 242405 (2012).

[93] C. L. Zhang, D. H. Wang, Q. Q. Cao, Z. D. Han, H. C. Xuan, and Y. W. Du, *Magnetostructural Phase Transition and Magnetocaloric Effect in Off-*

Stoichiometric $Mn_{1.9-x}Ni_xGe$ Alloys, Appl. Phys. Lett. **93**, 122505 (2008).

[94] E. K. Liu, H. G. Zhang, G. Z. Xu, X. M. Zhang, R. S. Ma, W. H. Wang, J. L. Chen, H. W. Zhang, G. H. Wu, L. Feng, and X. X. Zhang, *Giant Magnetocaloric Effect in Isostructural MnNiGe-CoNiGe System by Establishing a Curie-Temperature Window*, Appl. Phys. Lett. **102**, 122405 (2013).

[95] V. Johnson and C. G. Frederick, *Magnetic and Crystallographic Properties of Ternary Manganese Silicides with Ordered Co_2P Structure*, Phys. Status Solidi **20**, 331 (1973).

[96] C. L. Zhang, H. F. Shi, E. J. Ye, Y. G. Nie, Z. D. Han, B. Qian, and D. H. Wang, *Magnetostructural Transition and Magnetocaloric Effect in MnNiSi-Fe_2Ge System*, Appl. Phys. Lett. **107**, 2 (2015).

[97] C. L. Zhang, D. H. Wang, Z. D. Han, B. Qian, H. F. Shi, C. Zhu, J. Chen, and T. Z. Wang, *The Tunable Magnetostructural Transition in MnNiSi-FeNiGe System*, Appl. Phys. Lett. **103**, 132411 (2013).

[98] P. Lloveras, T. Samanta, M. Barrio, I. Dubenko, N. Ali, J. L. Tamarit, and S. Stadler, *Giant Reversible Barocaloric Response of $(MnNiSi)_{1-x}(FeCoGe)_x$ (x = 0.39, 0.40, 0.41)*, APL Mater. **7**, 0 (2019).

[99] S. Arumugam, S. Ghosh, A. Ghosh, U. Devarajan, M. Kannan, L. Govindaraj, and K. Mandal, *Effect of Hydrostatic Pressure on the Magnetic, Exchange Bias and Magnetocaloric Properties of $Ni_{45.5}Co_2Mn_{37.5}Sn_{15}$*, J. Alloys Compd. **712**, 714 (2017).

[100] S. Ghosh, P. Sen, and K. Mandal, *Effect of Si Doping on Magnetic and Magnetocaloric Properties of Ni–Co–Mn–Sn Alloys*, IEEE Trans. Magn. **54**, 1 (2018).

[101] S. Ghosh, A. Ghosh, and K. Mandal, *Reversible Magnetocaloric Effect and Critical Exponent Analysis in Mn-Fe-Ni-Sn Heusler Alloys*, J. Alloys Compd. **746**, 200 (2018).

[102] S. Ghosh, P. Sen, and K. Mandal, *Magnetostructural Transition and Large Magnetocaloric Effect in $(Mn0.6Fe0.4)NiSi_{1-x}Al_x$ (x = 0.06–0.08) Alloys*, J. Magn. Magn. Mater. **500**, 166345 (2020).

[103] S. Ghosh, A. Ghosh, P. Sen, and K. Mandal, *Giant Room-Temperature Magnetocaloric Effect Across the Magnetostructural Transition in $(MnNiSi)_{1-x}(FeCoGa)_x$ Alloys*, Phys. Rev. Appl. **14**, 014016 (2020).

Chapter 2 | Experimental details

This chapter describes the experimental technique employed to prepare the sample and further characterization and measurement techniques used in the present studies.

2.1 Preamble

We have presented here an overview of the preparation of alloys, and further processing of the prepared alloys to make them ready for several characterizations, and measurement techniques. We have prepared the samples for the present thesis using the conventional arc-melting technique. The crystallographic phase of these samples has been detected by performing the X-ray diffraction (XRD) pattern using RIGAKU MiniFlex II, and PANalytical X'Pert Pro. The final composition of the prepared sample has been checked by Energy dispersive analysis of X-ray (EDAX, Quanta FEG 250). Differential Scanning Calorimetry (DSC, TA instrument) is used for the thermal characterization of the samples. Magnetic measurements of these samples are carried out using Vibrating Sample Magnetometer (VSM, Lake Shore Cryotronics), Physical Property Measurement System (PPMS, Cryogenic Ltd.), PPMS (Quantum Design), and Superconducting Quantum Interference Devices (SQUID, MPMS, Quantum Design). Pressure dependence of magnetic measurements is performed in Quantum Design PPMS equipped with Cu-Be clamp-type pressure cell with a maximum pressure of 1 Gpa. All the above-mentioned techniques are described separately with their basic principle of operation.

2.2 Sample Preparation

All the investigated samples to study their magnetocaloric properties for magnetic refrigeration in this thesis are prepared using conventional arc-melting technique under 4N purity of the argon atmosphere [1–3]. The constituent raw elements of the samples are purchased separately from Sigma Aldrich. Their form and purity are as follows: Nickel (Ni: foil, 99.98%), Cobalt (Co: granules, 99.995%), Iron (Fe: granules, 99.98%), Manganese (Mn: chips, 99.9%), Tin (Sn: shots, 99.999%), Silicon (Si: pieces, 99.95%), Aluminum (Al: foil: 99.999%), and Gallium (Ga: trace metal basis, 99.9995%). A maximum current of about 100 A is used to prepare the as-prepared samples. Initially, a low current is used to melt the constituent elements of the sample which form as a single lump, and subsequently, a high current is used to melt the lump so that the elements diffuse to each other, and formed an alloy. The prepared ingots are re-

melted seven to eight times to ensure the compositional homogeneity. It can be noted that an extra few percentages (about 2–3%) of Mn is added to compensate for the weight loss due to its evaporation during melting while the prepared sample contains Mn as the main element.

The as-prepared samples with a tantalum (Ta) foil are sealed in an evacuated (10^{-3} bar) quartz tube. Afterward, the ampoule is annealed at 1173 K for 1 to 4 days. Ta foil is used to protect the sample from being oxidized as it absorbs the oxygen easily before the sample present in the sealed ampoule. After heat treatment for the required times, the ampoule is quenched into ice water. The annealed samples are then cut into desired pieces using Buehler make low speed saw, and then polished for characterization, and measurements. An image of the sealed ampoule, furnace used for annealing, and low speed saw are presented in **Fig. 2.1**

Figure 2.1: An image of (a) the sample with tantalum foil in an evacuated quartz ampoule (b) tube furnace used for annealing (c) Buehler make Low Speed Saw used to cut the sample into the desired shape.

2.2.1 Electric Arc-Melting Furnace

Electric arc-melting furnace (EAF) is a sample preparation unit which is used here to prepare the investigated samples with a high degree of purity by melting constituent elements of the alloy under argon atmosphere [4–6]. The furnace system consists of the Tri-Arc Furnace, a resistor box, a D.C. power supply, a set of water-cooled power cables to bring power, and water to the furnace, a chiller to supply cold water and pump for circulation of water, and a vacuum unit to evacuate the chamber. In our Tri-Arc furnace (Centorr Vacuum Industries, model: 5TA), the maximum output current of the power supply is 450 A. A temperature of about 3000^0C can be achieved in EAF. The whole apparatus is shown in **Fig. 2.2**.

The furnace consists of a water-cooled top, and bottom sections separated by a transparent Pyrex tube. The top section contains three electrodes with negative polarity for striking the arcs. Three copper stringer rods carry the tungsten electrodes, and these are equally spaced around the top of the furnace. Each copper stinger rod is mounted into a swivel ball which allows the vertical as well as the angular movement of the electrodes. Additionally, there is a relief valve that maintains the chamber pressure. The bottom section contains a tapered opening copper hearth to mount the samples, an inert gas inlet, and an outlet for roughing/purging of the chamber. The hearth provides positive bias with respect to the negative electrodes. These two top and bottom sections of the furnace are electrically isolated with the insulating Pyrex tube.

Firstly, a titanium piece is kept inside in a smaller, separate cup in the base of the furnace for additional atmosphere purification. Afterward, the materials are mounted on a copper hearth. The chamber is evacuated and then argon gas is purged into the chamber. To maintain the good quality of inert atmosphere inside the furnace chamber about 5–6 times roughing and purging are required. When the electrodes (cathode) are brought closer to the copper hearth (anode), an intense stream of electrons flows from cathode to anode through ionized argon gas and it leads to an electric arc. The applied current can be controlled from the power supply unit or using the paddle switch attached with it. Before start to melt the materials, the titanium piece is melted by

striking the arc to remove any presence of oxygen inside the furnace. Next, the electric arc is applied to the materials to form an alloy. Three electrodes are used at a time and the ingot is turned and re-melted several times to improve the homogeneity of the prepared samples.

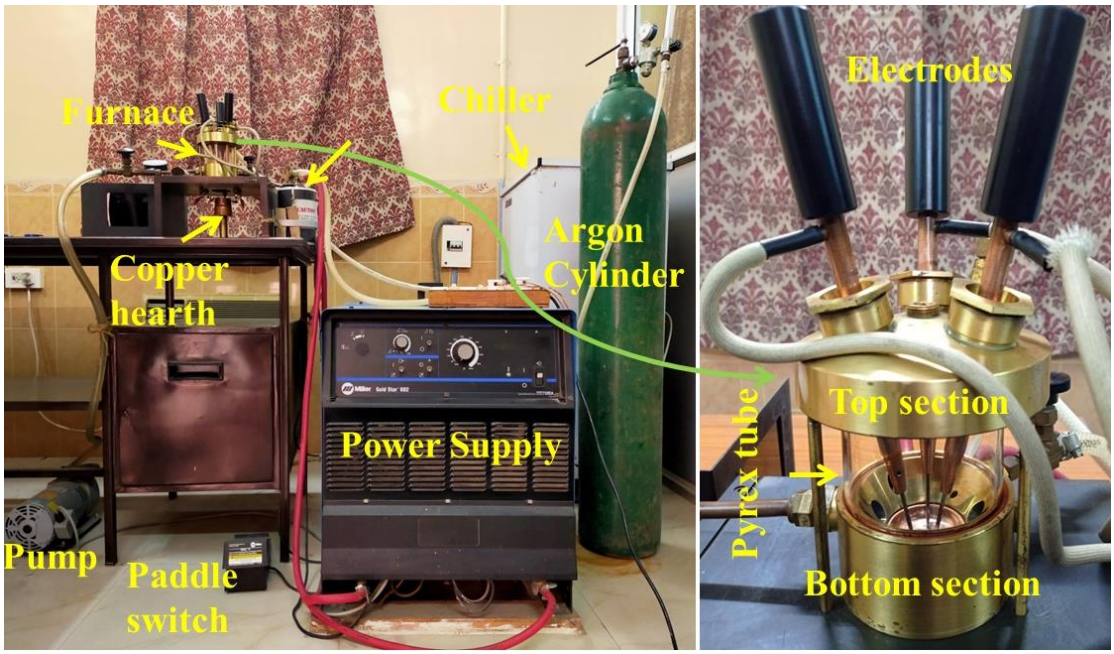

Figure 2.2: An image of EAF assembly (Centorr Vacuum Industries, model: 5TA)

2.3 Sample characterization

Here we will present an overview of the techniques which are used to characterize the structural properties, elemental composition, and thermal analysis of the sample. Thermal measurement of the sample can provide important information about its thermodynamic properties such as heat capacity, phase transition, corresponding latent heat, and so on.

2.3.1 X-ray diffraction

X-ray diffraction (XRD) is an extensively used technique for the characterization of crystalline materials [7]. It provides information about the crystal structures, phases,

preferred crystal orientations, and other structural parameters such as average grain size, lattice strain, and crystal defects. X-ray having wavelength similar to the distance between atoms of the crystal, it is used to study the atomic structure. A schematic presentation of X-ray diffraction measurement is shown in **Fig. 2.3.** The cathode ray tube and associated electronics generate limited frequency ranges of X-rays which are filtered to produce monochromatic radiation. A crystalline material can be considered as a periodic arrangement of atoms. When monochromatic X-rays having a wavelength, λ, fall on to the crystalline sample, X-rays are scattered elastically by the electrons of atoms within the crystal plane and form outgoing spherical waves. These scattered waves interfere constructively in a few specific directions following Bragg's law [8],

$$2d \sin\theta = n\lambda \tag{2.1}$$

where, d is the inter-planer spacing in the crystal, θ, the angle of diffraction, and n is an integer (order of diffraction). In practicality, θ is the incident angle of the X-ray beam with respect to the sample which is varied for a wide range of angles for a small step, and 2θ is the diffraction angle of the reflected beam with respect to the direction of the incident beam. The diffracted beam of X-ray is collected in all possible directions by a detector. Subsequently, the conversions of diffraction peaks to the d spacing allow us to identify the presence of elements in the sample with their crystalline nature. The peak positions provide detailed information about the crystal plane. Experimental diffraction peaks are identified by comparing the data with the Joint Committee on Powder Diffraction Standard (JCPDS) database.

Generally, the XRD pattern is performed in two types of systems. In the θ–2θ system, the X-rays source is fixed, and the sample rotates at θ^0/min while the detector moves at $2\theta^0$/min. In the θ–θ system, the sample stage is fixed while the X-ray source and the detector rotate simultaneously at an angular speed of θ^0/min. We have used RIGAKU MiniFlex II (θ–2θ system) and PANalytical X'Pert Pro (θ–θ system) X-ray diffractometer using Cu-K_α radiation (λ = 1.54 Å) for initial characterization of our investigated sample for the present studies.

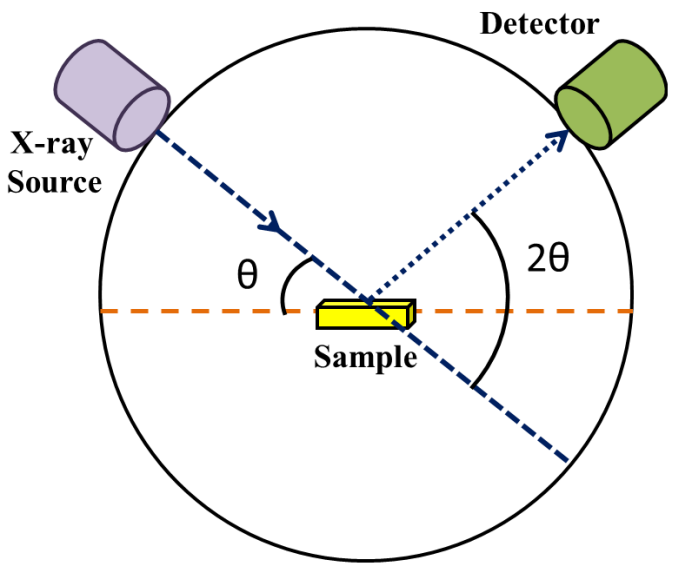

Figure 2.3: Schematic diagram of an X-ray diffractometer

2.3.2 Energy dispersive analysis of X-ray

Energy dispersive analysis of X-ray (EDAX) is a useful technique to determine the elemental composition of a material [9]. The atom of every element possesses a unique electronic structure with characteristic binding energies profile in different energy levels. During EDAX, the material (sample) is bombarded by high energy electron beams. When the bombarding electrons interact with the sample electrons, it can excite electrons of the inner shell of the atoms to higher energy levels or can knock out some of them during this process. Subsequently, there is an electrons deficiency (holes) by the ejected electrons in the inner shells, and eventually, it is filled by the electrons from the high energy levels of the outer shell. However, the energy difference between these two energy levels is emitted as an X-ray from the material. In general, a Si (or Li) detector is used as an energy dispersive spectrometer to measure the amount of energy and to count the number of emitted X-rays. A schematic presentation of this fundamental process is shown in **Fig. 2.4.** Furthermore, during the transferring process, the atom of each element releases X-rays with unique amounts of energy. Therefore the presence of elements in the sample can be identified by measuring the amounts of energy present in the X-rays being released by a sample. An EDAX spectrum exhibits

peaks corresponding to the energy levels for which the most X-rays have been received. Those peaks are unique to an atom and hence, for a single element. The relative intensities of those peaks provide the atomic percentage of the elements present in the sample.

The EDAX system performs as an integrated feature of a Scanning Electron Microscope (SEM). Here for the present studies, we have used SEM with model no: QUANTA FEG 200 to characterize our samples.

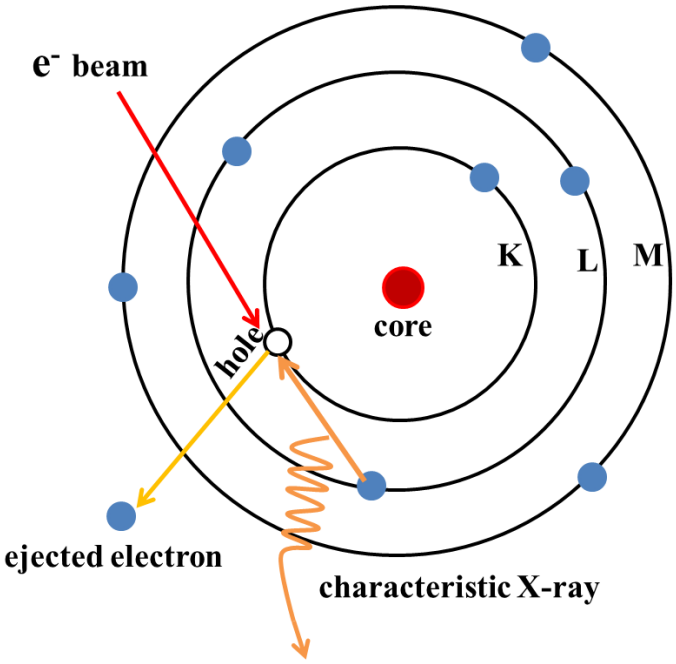

Figure 2.4: Schematic presentation of the interaction of high energy electron beam with the sample, and emission of X-ray from an atom.

2.3.3 Differential Scanning Calorimetry

Differential Scanning Calorimetry (DSC) is one of the most useful analytical technique for thermal characterization of any solid and liquid sample [10]. DSC measures the difference in the heat flow of the sample with respect to an inert reference, as a function of time and temperature while both the sample and reference are subjected to a similar atmosphere such as temperature, time, and pressure. It provides quantitative and

qualitative characteristics such as phase transition and other heat related changes of the sample occurs on endothermic (heat absorption) and exothermic (heat evolution) processes.

A schematic diagram of DSC is shown in **Fig. 2.5**. The sample material is encapsulated in a pan and an empty pan is used as a reference pan. Both the sample and reference pan are made of the same material having good thermal conductivity (usually made of Al). Both pans are placed on the raised stage of a thermoelectric disk made of constantan ($Cu_{55}Ni_{45}$) alloy. The constantan disk is the essential way of heat transfer to and from the sample material and the reference. A chromel ($Ni_{90}Cr_{10}$) wafer is there to cover the underside of the raised platforms. Moreover, to measure the temperature difference between the sample material and reference, two thermocouples junctions made of chromel ($Ni_{90}Cr_{10}$) and alumel ($Ni_{95}Mn_2Al_2Si$) wires are attached with the chromel wafers.

During measurement, both the sample and the reference are kept in the same thermal environment and subjected to a linear temperature ramping rate and eventually, the temperature difference between the sample and the reference (ΔT) i.e. the extra amount of heat is released or absorbed by the sample, measured by the thermocouple is converted to the differential heat flow (q) as,

$$q = \frac{\Delta T}{R} K_1 K_2 \tag{2.2}$$

where R is the thermal resistance of the constantan disk. K_1 and K_2 stand for the factory-set and user-set calibration values. The existence of any phase transition that is accompanied by the thermal changes can be detected from the DSC heat flow curve.

Our most of the studied samples are found to undergo a first order magnetic field induced martensitic transformation. We have used the DSC heat flow curve, performed at the temperature ramp rate of 10 K/min, to detect the characteristic transition temperatures of martensitic transformation such as martensite start (M_s), martensite finish (M_f), austenite start (A_s), and austenite finish (A_f) temperatures. The

latent heat, enthalpy, and the total entropy changes associated with the phase transition can also be evaluated by analyzing the DSC curve. Moreover, the specific heat of the sample can be evaluated as a function of temperature using a modulated DSC technique where a sinusoidal or modulated heating rate is applied over the linear heating rate.

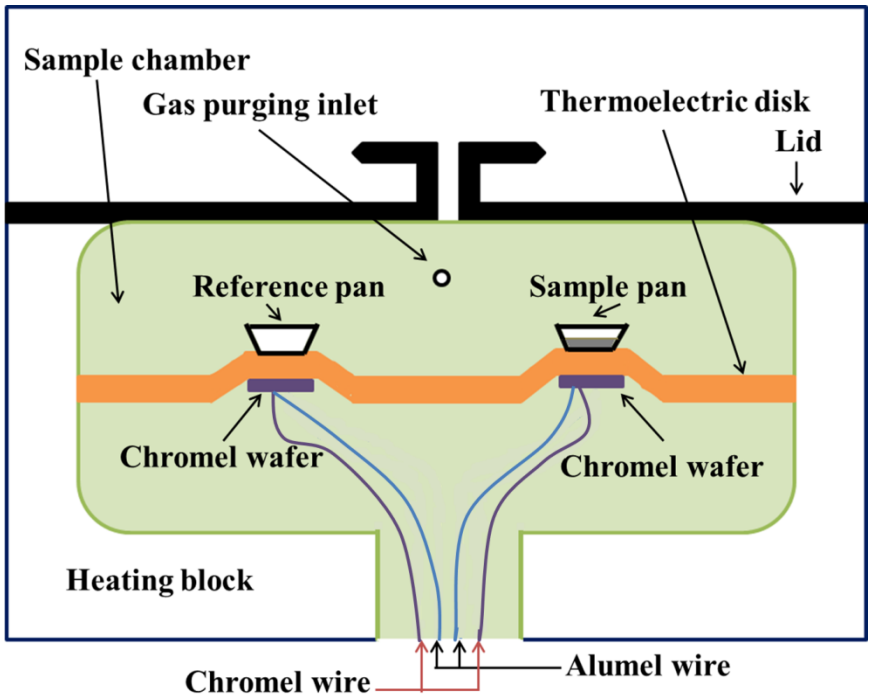

Figure 2.5: Schematic diagram of a Differential Scanning Calorimeter

2.4 Magnetic measurement technique

To estimate the magnetocaloric parameters using the Maxwell equation, we have performed temperature dependence of magnetization (*M* vs. *T*) and isothermal magnetic field dependent magnetization (*M* vs. *H*) curves. *M-T* measurements are carried out in an external magnetic field up to 90 kOe. *M-H* measurements are performed for a maximum field of 50 kOe. All the magnetic measurements are carried out using Vibrating Sample Magnetometer (VSM, Lake Shore Cryotronics), Physical Property Measurement System (PPMS, Cryogenic Ltd.), PPMS (Quantum Design), and Superconducting Quantum Interference Devices (SQUID, MPMS, Quantum Design). Pressure dependence of magnetic measurements is performed in Quantum Design

PPMS equipped with Cu-Be clamp-type pressure cell with a maximum pressure of 1 Gpa.

2.4.1 Vibrating Sample Magnetometer

The magnetic behavior of a magnetic material can be measured using a Vibrating Sample Magnetometer (VSM). VSM is a very sensitive magnetometer that can measure a very low magnetic moment up to the order of 10^{-5}-10^{-6} emu [11]. VSM operates based on Faraday's law of induction which states that an electromotive force (emf), V, will be induced in a coil if there is a change in magnetic flux linking with the coil.

The schematic diagram of a VSM is shown in **Fig. 2.6**. In this magnetometer, an electromagnet is used to apply a constant magnetic field to magnetize the sample. Two identical but oppositely wound pick-up coils are mounted on the poles of the electromagnet. The sample is placed at the center in the region between the poles of the electromagnet. A thin vertical nonmagnetic rod, usually made of plastic or quartz, connects the sample holder to the transducer assembly which is placed above the magnet. The oscillator generates a sinusoidal signal that is converted by the transducer assembly into a vertical vibration of the sample. An external dc magnetic field is set to a constant value which magnetizes the sample and hence, any change in magnetic flux density inside the sample will be due to the change in magnetization only. As the sample vibrates mechanically, according to Faraday's law of induction, the change in magnetic flux density that links with pick-up coils will produce an emf as,

$$V = -\frac{d\Phi}{dt} \tag{2.3}$$

where Φ is the magnetic flux. For the pick-up coils with a cross-sectional area A and N number of turns,

$$V = -NA\frac{dB}{dt} \tag{2.4}$$

where B is the magnetic flux density. When the pick-up coils are placed in a constant magnetic field (H),

$$B = \mu_0 H \tag{2.5}$$

where, μ_0 is the permeability of free space. Now, if the sample is placed between pick-up coils in a constant magnetic field, the sample will be magnetized and have a magnetization M. Hence, the magnetic flux density near the sample takes the form as,

$$B = \mu_0 (H + M) \tag{2.6}$$

Therefore, the corresponding change in magnetic flux density is given by,

$$\Delta B = \mu_0 M \tag{2.7}$$

The induced emf in the pick-up coils can be expressed as,

$$Vdt = -\mu_0 NAM \tag{2.8}$$

The output signal is proportional to the magnetization of the sample but independent of an applied magnetic field in which the magnetization of the sample has to be determined. This signal goes through the lock-in amplifier as an input. The mechanical vibrator's frequency is set to the reference of the lock-in amplifier to eliminate the noise of the environment and to deduce the magnetic moment of the sample only. However, though the induced emf signal in the pick-up coils is proportional to the magnitude of the moment of the sample, it also depends on other factors such as frequency and the amplitude of the vibration. Thus, the magnetic moment estimation by measuring the amplitude of the signal may generate an error. To eliminate these issues, a vibrating capacitor is used to generate the reference signal which varies with the vibrational frequency and the amplitude, in the same manner, the signal form in the pick-up coils.

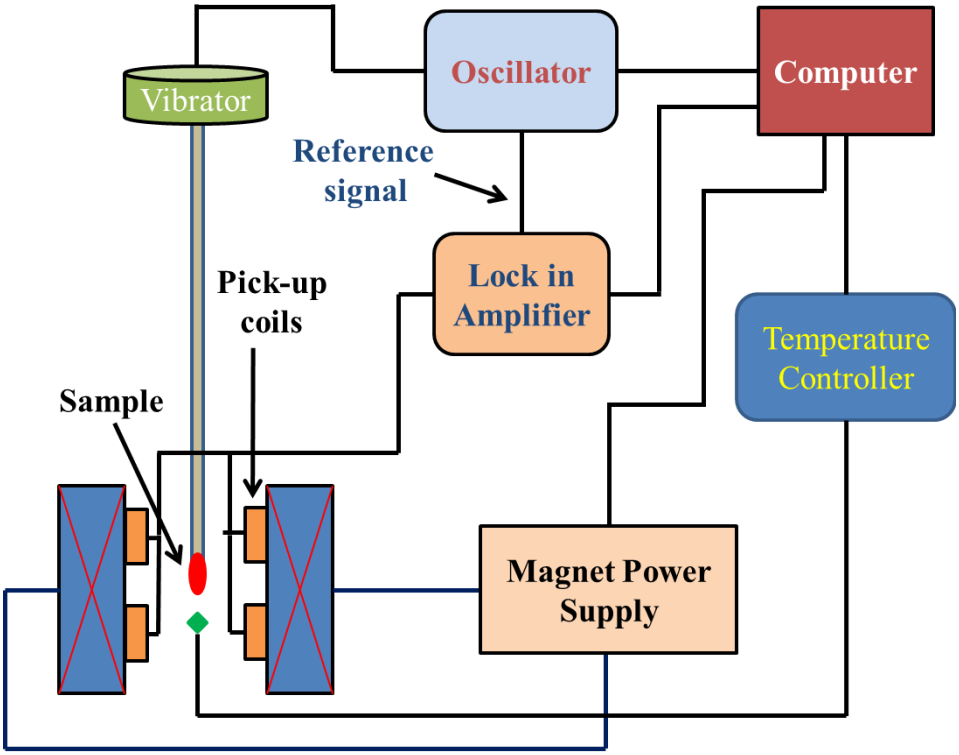

Figure 2.6: Schematic diagram of a Vibrating Sample Magnetometer

2.4.2 SQUID Magnetometer

Superconducting Quantum Interference Devices (SQUID) is the most sensitive and effective magnetic flux detector. It is capable of measuring any physical quantities which can be converted to magnetic flux, such as magnetic field, magnetic field gradient, magnetic moment, current, voltage, and magnetic susceptibility [12]. Hence, the application of SQUID is wide ranging. This device can detect an incredibly small magnetic field, small enough to measure the magnetic fields in living organisms [13].

The working principle of SQUID is based on two physical phenomena [12–15]. One is flux quantization which means the magnetic flux (Φ) in a superconducting ring is quantized and exists only in multiple of flux quantum ($\Phi_0 = h/2e = 2.068\times10^{-15}$ Wb, 1 Wb/m^2 = 1 T). Eventually, the magnetic field inside a ring with the area of 1 cm^2 can only exit in discrete steps of 2.068×10^{-11} T. The other physical phenomenon is the Josephson effect. SQUID can be of two types. The first one is dc SQUID which is consisted of two nearly identical Josephson junctions connected in parallel in a

superconducting loop and it is operated with a steady current bias. The other one is rf SQUID which utilizes a single Josephson junction interrupting the current flow around the superconducting loop and it is operated with a radio frequency flux bias.

Josephson junction is a fundamental structure on which a SQUID works. When two superconductors are separated by an insulating layer, a Josephson junction is formed. When the insulator is thin enough, superconducting electrons i.e cooper pair of electrons (the electrons in the superconducting state form correlated pairs of electrons with opposite spin and momentum called cooper pairs) are able to tunnel from one superconductor to the other superconductor through the insulating layer barrier which results the flow of resistance less current through the insulator. This is known as the Josephson Effect. The applied current (I) flows through a Josephson junction depends on the difference in phases (δ) of the two superconductors at the insulating barriers as $I = I_0 \sin \delta$. Where I_0 stands for the critical current which is the maximum supper current the junction can sustain.

Typically, a dc SQUID can be considered as a superconducting loop with inductance L, interrupted by two identical and symmetrically placed Josephson junctions connected in parallel and a steady bias current source is applied, shown in **Fig. 2.7(a)**. A high quality Josephson junction exhibits hysteretic I-V characteristic (shown in **Fig. 2.7(b)**). As the current is increased from zero value and less than I_0 value, the superconducting current flows through the junction without any voltage drop. When the current is increased further beyond I_0, the voltage starts to increase abruptly and it returns to zero only when the current is reduced to a lower value than I_0. To eliminate the hysteresis on the I-V characteristic, both the junction are shunted with a shun resistance. Now, we assume that the bias current is increased from zero to a slightly higher value than the critical current of the two junctions. In absence of any external magnetic field, no current will be circulating around the superconducting loop and hence, bias current will be divided equally to the two junctions. Subsequently, when an external magnetic flux ($\Phi = B_{ext}A$) is applied, there will be a screening current around the superconducting loop ($I_S = - \Phi/L$) as the superconductor expels the

magnetic flux through it. This induced current will flow along the direction of bias current of one junction and opposite direction of the other junction and eventually, that will increase or decrease the critical current of the junction depending on the direction of the screening current. Hence, the voltage drop in the Josephson junction will change. Now, during an increase or decrease in applied flux, the voltage will change periodically with the period being that of the flux quantum Φ_0. Therefore, the dc SQUID transforms the magnetic flux that has been coupled to the SQUID loop to a measurable voltage.

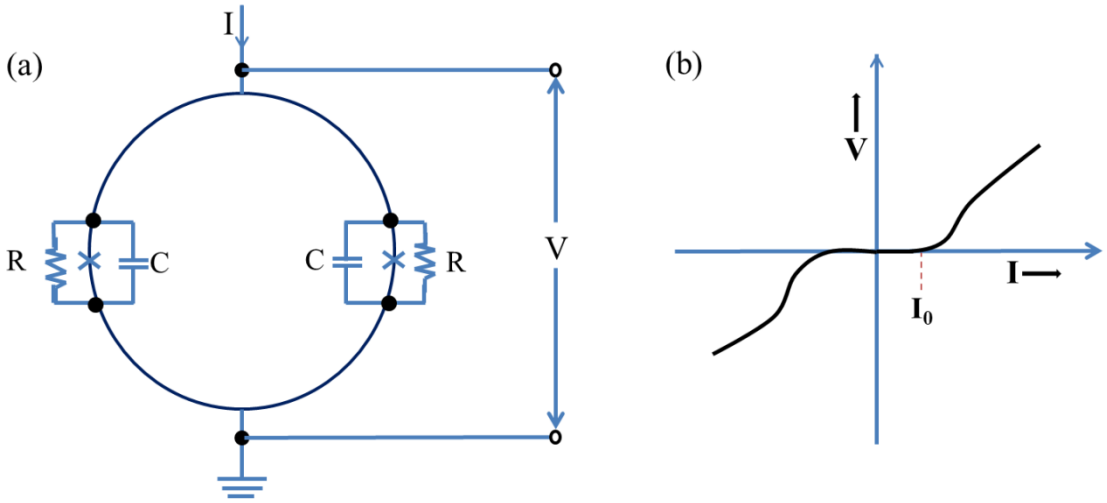

Figure 2.7: (a) A schematic diagram of a dc SQUID (b) I-V characteristic of a Josephson junction.

A schematic setup of the used MPMS SQUID magnetometer detection system is shown in **Fig. 2.8**. When the sample moves through the superconducting pick-up coils, a magnetic flux associated with the coil changes. Usually, SQUID detects the flux change which is converted to a voltage V_{SQUID}. For MPMS, the sample position is denoted as 'x' position which is parallel to the applied external magnetic field. The output voltage V_{SQUID} is recorded as a function of the position x, which is also shown in **Fig. 2.8**. To suppress the influence of all kinds of external magnetic fields, the pick-up coils are configured as second order gradiometer. A linear regression algorithm of the MPMS software fits the output data to a theoretical curve of an ideal dipole and extracts the magnetic moment of the sample.

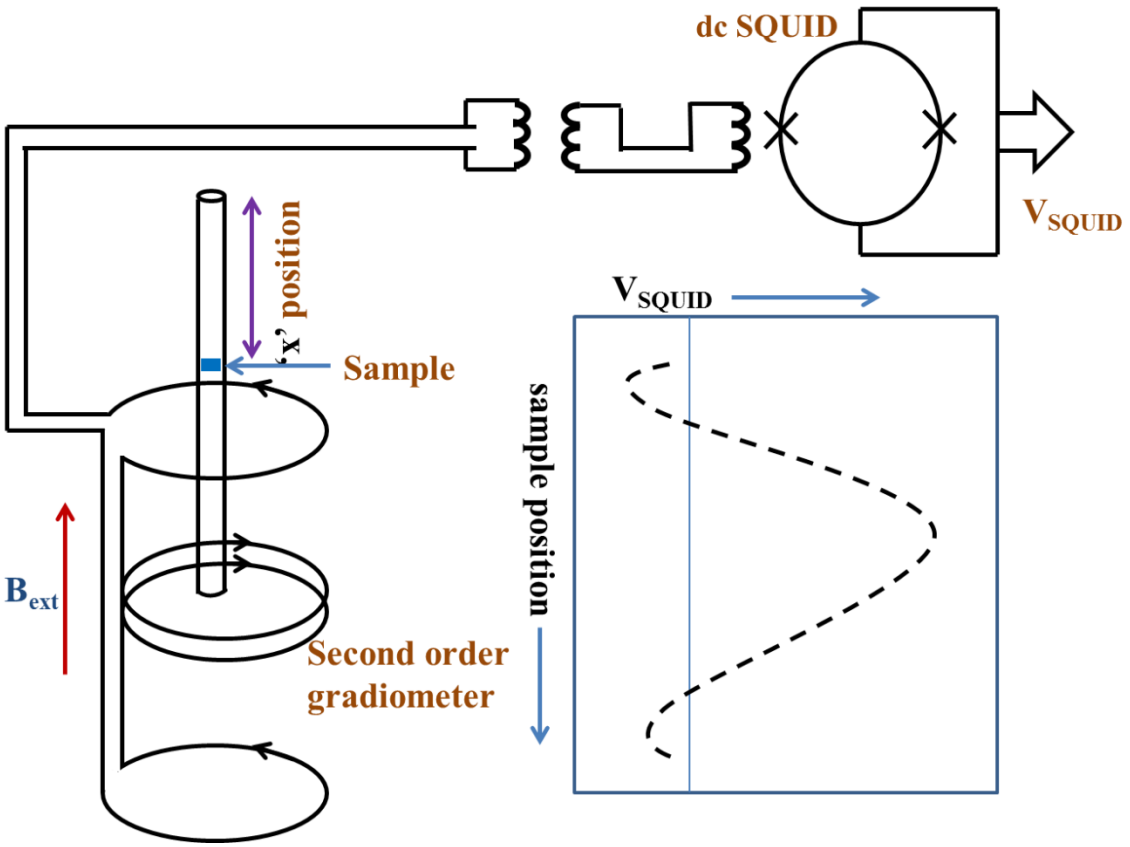

Figure 2.8: Schematic setup of MPMS SQUID with second order gradiometer [Inset: the output signal of SQUID as a function sample position].

References

[1] S. Arumugam, S. Ghosh, A. Ghosh, U. Devarajan, M. Kannan, L. Govindaraj, and K. Mandal, *Effect of Hydrostatic Pressure on the Magnetic, Exchange Bias and Magnetocaloric Properties of* $Ni_{45.5}Co_2Mn_{37.5}Sn_{15}$, J. Alloys Compd. **712**, 714 (2017).

[2] S. Ghosh, A. Ghosh, and K. Mandal, *Reversible Magnetocaloric Effect and Critical Exponent Analysis in Mn-Fe-Ni-Sn Heusler Alloys*, J. Alloys Compd. **746**, 200 (2018).

[3] S. Ghosh, A. Ghosh, P. Sen, and K. Mandal, *Giant Room-Temperature Magnetocaloric Effect Across the Magnetostructural Transition in* $(MnNiSi)_{1-x}(FeCoGa)_x$ *Alloys*, Phys. Rev. Appl. **14**, 014016 (2020).

[4] A. Ghosh and K. Mandal, *Effect of Fe Substitution on the Magnetic and Magnetocaloric Properties of Mn-Rich Mn-Ni-Fe-Sn off-Stoichiometric Heusler Alloys*, J. Appl. Phys. **117**, 093909 (2015).

[5] A. Ghosh and K. Mandal, *Effect of Structural Disorder on the Magnetocaloric Properties of Ni-Mn-Sn Alloy*, Appl. Phys. Lett. **104**, 031905 (2014).

[6] R. Sahoo, A. K. Nayak, K. G. Suresh, and A. K. Nigam, *Effect of Fe Substitution on the Magnetic, Transport, Thermal and Magnetocaloric Properties in* $Ni_{50}Mn_{38-x}Fe_xSb_{12}$ *Heusler Alloys*, J. Appl. Phys. **109**, 123904 (2011).

[7] B. D. Cullity and S. R. Stock, *Elements of X-Ray Diffraction, 3rd Edition*, Prentice Hall (2001).

[8] C. Kittel, *Introduction to Solid State Physics 7th Edition- Kittel, Charles*, in *John Wiley & Sons* (1996).

[9] J. I. Goldstein, D. E. Newbury, P. Echlin, D. C. Joy, C. E. Lyman, E. Lifshin, L. Sawyer, and J. R. Michael, *Scanning Electron Microscopy and X-Ray Microanalysis* (Springer US, Boston, MA, 2003).

[10] P. Gabbott, *A Practical Introduction to Differential Scanning Calorimetry*, in *Principles and Applications of Thermal Analysis* (Blackwell Publishing Ltd, Oxford, UK, 2008), pp. 1–50.

[11] S. Foner, *Versatile and Sensitive Vibrating-Sample Magnetometer*, Rev. Sci. Instrum. **30**, 548 (1959).

[12] H. Weinstock, editor, *SQUID Sensors: Fundamentals, Fabrication, and Applications* (Springer Netherlands, Dordrecht, 1996).

[13] A. Zięba, *Image and Sample Geometry Effects in SQUID Magnetometers*, Rev. Sci. Instrum. **64**, 3357 (1993).

[14] R. L. Fagaly, *Superconducting Quantum Interference Device Instruments, and Applications*, Rev. Sci. Instrum. **77**, 101101 (2006).

[15] M. Buchner, K. Höfler, B. Henne, V. Ney, and A. Ney, *Tutorial: Basic Principles, Limits of Detection, and Pitfalls of Highly Sensitive SQUID Magnetometry for Nanomagnetism and Spintronics*, J. Appl. Phys. **124**, 161101 (2018).

Chapter 3 | Magnetostructural transition and large magnetocaloric effect in $(Mn_{0.6}Fe_{0.4})NiSi_{1-x}Al_x$ alloys

This chapter describes the tuning of magnetostructural transition and the giant magnetocaloric properties across that transition in earth-abundant cost-effective transition metal based $(Mn_{0.6}Fe_{0.4})NiSi_{1-x}Al_x$ (x = 0.06 - 0.08) alloys and the present studies suggest that these materials can be very effective as magnetic refrigerant materials.

3.1 Preamble

Recently, studies of Mn*TX* (*T* = Co, Ni, and *X* = Ge, Si) intermetallic compounds have drawn considerable attention to the researchers owing to their magnetoresponsive multifunctional properties such as temperature induced magnetostructural transition (MST), magnetic shape memory effect (MSME), giant magnetocaloric effect (MCE), volume anomalies around room temperature [1–12]. These stoichiometric intermetallic compounds are observed to undergo a first order structural transformation, beyond the second order magnetic transition temperature, from TiNiSi-type orthorhombic structure to a Ni_2In-type hexagonal structure in the paramagnetic (PM) region without having a significant change in magnetization and thus, it is not suitable for room temperature magnetic refrigeration technology. Hence, it is desired to lower the structural transition to around room temperature in the magnetically ordered ferromagnetic (FM) state. Magnetoresponsive properties of these compounds are related to change in magnetization across their phase transitions. Therefore, it is crucial to couple both the magnetic and structural transitions at the same temperature to achieve a large magnetocaloric response in these alloys.

In order to obtain coupled MST in these systems, several efforts are made till now such as by element substitution, changing of stoichiometry, isostructurally substitution, or application of hydrostatic pressure [8,10,12–14]. For that purpose, MnCoGe and MnNiGe from the Mn*TX* system are extensively studied materials so far to obtain MST and the corresponding giant MCE across MST having their closeness of both magnetic and structural transition temperatures. MnCoGe [15] system in stoichiometric composition exhibits a magnetic transition at Curie temperature, T_C = 355 K and a structural transition at T_M = 650 K whereas, stoichiometric MnNiGe system [16] shows a magnetic transition temperature at Neel temperature, T_N = 346, followed by a structural transformation at T_M = 470 K. For instance; Fang *et al.* [3] reported that off stoichiometric $MnCo_{0.95}Ge_{1.14}$ alloy exhibits a large magnetic entropy change ($|\Delta S_M|$) about 6.4 J kg^{-1} K^{-1} for magnetic field change of $\Delta H = 10$ kOe at a peak temperature T = 331 K which is associated with first order MST. Trung *et al.* [17] discovered the coupled MST and the corresponding giant MCE near room temperature by addition of few

percent interstitial of boron atoms in $MnCoGeB_x$ alloy and they obtained an optimum $|\Delta S_M|$ about 47.3 J kg^{-1} K^{-1} due to $\Delta H = 50$ kOe at T = 287 K for the alloy with x = 0.02. Liu *et al* [8] reported a coupled MST with giant MCE ($|\Delta S_M| = 40$ J kg^{-1} K^{-1} due to $\Delta H = 50$ kOe at T = 238 K) in isostructural alloying MnNiGe system with CoNiGe system.

However, the stoichiometric MnNiSi [18] compound exhibits a magnetic transition at T_C = 622 K and a first order structural transition at a high temperature of about 1210 K in the paramagnetic state. Therefore, the large separation between the magnetic and structural transition temperature and the occurrence of both transitions at high temperatures make it very difficult to obtain MST near room temperature for this system though it will be a very cost-effective material for commercial usage. Recently, *Li et al* [19] observed a significant decrease of structural transformation temperature (T_M) due to the substitution of Fe and Co in place of Mn-site of MnNiSi system. *Zhang et al* [20] chemically alloyed MnNiSi with binary compound Fe_2Ge and studied the MCE properties across MST for different compositions of that alloy. Moreover, by chemically alloying MnNiSi with an isostructurally ternary compound such as FeNiGe or FeCoGe, giant MCEs are obtained near room temperature [14,21].

In this chapter, we have investigated the tuning of MST and the magnetocaloric properties across it by substituting Al in the place of Si site of $(Mn_{0.6}Fe_{0.4})NiSi$ chosen as parent alloy. The reported values of T_C and T_M of nearly similar composition, $(Mn_{0.64}Fe_{0.36})NiSi$ [19], very close to our parent alloy, are 529 K and 881 K respectively. Interestingly, T_M value reduces to room temperature with Al doping and for a nominal composition of $(Mn_{0.6}Fe_{0.4})NiSi_{0.93}Al_{0.07}$, we have observed first order MST with a large value of magnetic entropy change (ΔS_M) about −20.6 J kg^{-1} K^{-1} at 255 K. These transition metal based low-cost alloys are suitable for commercial use.

3.2 Experimental

Conventional arc-melting technique is used to prepare polycrystalline $(Mn_{0.6}Fe_{0.4})NiSi_{1-x}Al_x$ (x = 0.06, 0.07 and 0.08) samples under 4N purity argon atmosphere using high purity constituent elements. To ensure compositional homogeneity, samples are re-

melted five to six times. The as-cast samples are then sealed in an evacuated quartz tube along with a tantalum foil and annealed for 100 hours at 1173 K, followed by quenching it into ice water. The Compositions of annealed samples are checked by energy dispersive analysis of X-ray (EDAX) and the analyzed compositions are found to be very similar to the starting compositions. X-ray diffraction (XRD) patterns of the investigated samples are carried out using PANalytical X'Pert Pro with Cu-K_α radiation (wavelength, λ = 1.54 Å). We have prepared the powder form of the annealed samples using a mortar and pastel for XRD measurement. Thermomagnetic data (*M-T* curve) and isothermal magnetic measurements (*M-H* curve) are performed using a Physical Property Measurement System (PPMS, Cryogenic Limited) with a maximum applied magnetic field of 50 kOe. *M-T* measurements are performed for a temperature region of 80 – 400 K in presence of different applied magnetic fields under zero field cooled (ZFC) and field cooled (FC) condition. In ZFC condition, the sample is cooled from room temperature to a low temperature in presence of zero magnetic field and subsequently, the *M-T* data has been recorded with increasing temperature for the targeted region at a small interval in presence of a constant applied magnetic field. In FC condition the *M-T* data has been recorded when the sample is subjected to the constant magnetic field and the temperature is reduced to a targeted lower temperature at a small interval. *M-H* measurements are carried out for a maximum applied magnetic field of 50 kOe and the field sweeping is done as follows, 0→50 kOe→ 0. Differential scanning calorimetry (DSC) is performed to detect phase transition temperatures of the annealed samples both in heating and cooling mode with a temperature ramp rate of 10 K/min.

3.3 Results and Discussion

Figure 3.1 shows the XRD patterns for all the samples at room temperature (*RT* = ~ 300 K). In the figure, 'h' and 'o' denote the peaks of hexagonal Ni_2In-type and orthorhombic TiNiSi-type structures respectively. With enhancing Al content in Si sites the structure changes from orthorhombic TiNiSi-type (x = 0.06) to hexagonal Ni_2In-type (x = 0.08) at *RT*, suggesting that T_t decreases to lower temperature with Al substitution. For the alloy with x = 0.07, the structure is hexagonal and the estimated lattice

parameters are $a_{hex} = 3.97$ Å and $c_{hex} = 5.13$ Å. The calculated lattice parameters of orthorhombic structure for the alloy with x = 0.06 are $a_{ortho} = 5.55$ Å, $b_{ortho} = 3.80$ Å and $c_{ortho} = 6.84$ Å.

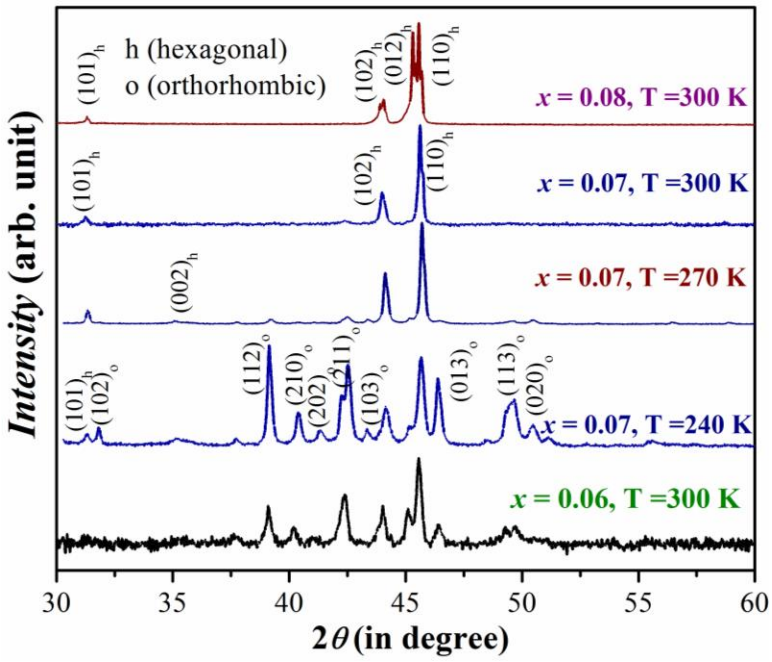

Figure 3.1: XRD patterns of $(Mn_{0.6}Fe_{0.4})NiSi_{1-x}Al_x$ (x = 0.06, 0.07 and 0.08) alloys at 300 K and temperature dependent XRD patterns for the alloy with x = 0.07.

Further, the temperature dependence of the XRD pattern is performed for the alloy with x = 0.07 and is shown in **Fig. 3.1**. At 240 K, dominating the orthorhombic phase is observed along with some traces of hexagonal phase as the MST is close to that temperature. On the increasing temperature, the hexagonal phase dominates and it is the only phase observed at 300 K. The unit cell volume changes about 2.81 % during the structural transformation from the low temperature orthorhombic to high temperature hexagonal phase. The lattice strain developed in these materials is calculated using the Williamson-Hall method [22]. The estimated lattice strain for the alloy with x = 0.07 at 240 K in the orthorhombic phase is 0.0038 whereas it is 0.0023 in the hexagonal phase at 300 K. Therefore, the structural transformation of these materials is accompanied by a significant change in unit cell volume as well as in lattice strain.

The temperature dependent magnetization curves (*M-T* curves) for the samples $(Mn_{0.6}Fe_{0.4})NiSi_{1-x}Al_x$ (x = 0.06, 0.07 and 0.08) are carried out in the presence of 500 Oe field during ZFC and FC condition within a temperature regime of 80 K – 400 K at an interval of 5 K which are shown in **Fig. 3.2**. For x = 0.06 and 0.07, the sudden change in magnetization during both heating and cooling indicates the MST between low temperature FM orthorhombic phase and high temperature PM hexagonal phase. The presence of thermal hysteresis signifies the coupling of magnetic and structural transition, leading to a coupled MST which is first order in nature. The magneto-structural transition temperature (T_t), defined as the temperature where dM/dT shows a maximum on heating, shifts towards lower temperature with higher substitution of Al replacing Si. On further doping of Al in place of Si sites, the sample with x = 0.08 does not exhibit any first order MST in the temperature region of 80 K ≤ T ≤ 400 K. Hence, x ~ 0.07 is the maximum doping content of Al for this system to achieve coupled MST suitable for room temperature magnetic refrigeration.

Further *M-T* measurements for the alloy with x = 0.07 is carried out for the various applied magnetic field of 10, 30 and 50 kOe for the temperature region of 100 K ≤ T ≤ 300 K at an interval of 1 K which is shown in **Fig. 3.3**. T_t is found to increase from 272 K to 277 K with enhancing magnetic field from 500 Oe to 50 kOe that signifies the field dependency of MST. As the low temperature FM orthorhombic phase is magnetically more sensitive to the applied magnetic field than the high temperature PM hexagonal phase, low temperature phase is preferred and stabilized to higher temperature in the presence of a magnetic field. That's why a shift in transition temperature towards higher temperature is observed with the magnetic field. Moreover, a large change in magnetization about 50.3 emu g^{-1} is observed during MST from PM phase to FM phase due to an application of 50 kOe magnetic field. In MST, the magnetovolume effect changes the ferromagnetic interaction leading to a sharp change in magnetization at PM to FM transition.

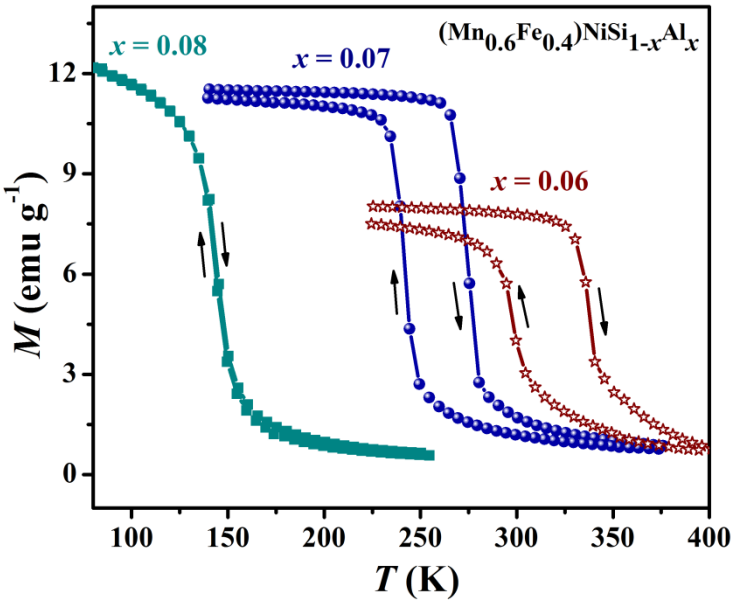

Figure 3.2: (a) *M-T* curves for $(Mn_{0.6}Fe_{0.4})NiSi_{1-x}Al_x$ (x = 0.06, 0.07 and 0.08) alloys in presence of 500 Oe magnetic field.

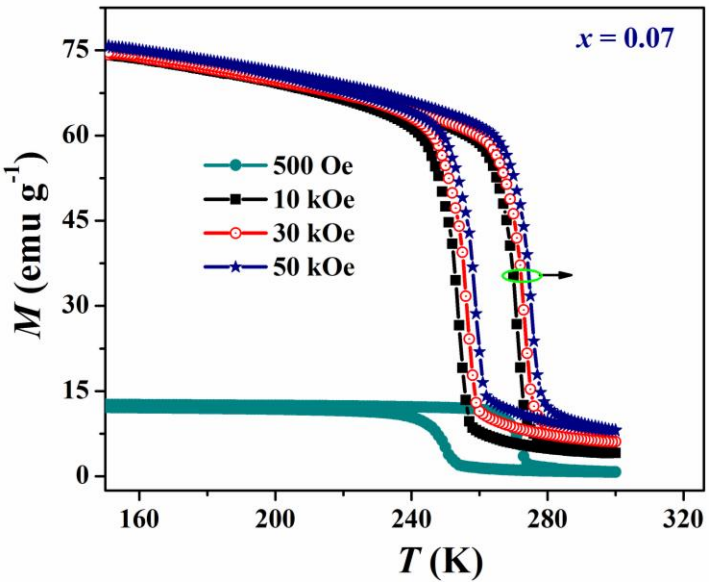

Figure 3.3: *M-T* curve for the alloy with x = 0.07 in presence of different applied magnetic field at a temperature interval of 1 K.

In order to detect the phase transition temperatures of the investigated samples, differential scanning calorimetry heat flow curves are measured for the samples with x = 0.06 and 0.07 during both heating and cooling with a ramp rate of 10 K/min which

are shown in **Fig. 3.4**. The observed exothermic/endothermic peak during the cooling/heating cycle with large thermal hysteresis again signifies the first order nature of MST. T_t reduces with increasing Al substitution and its values calculated from the endothermic peak of the curve are 339 K and 271.3 K for x = 0.06 and 0.07 respectively.

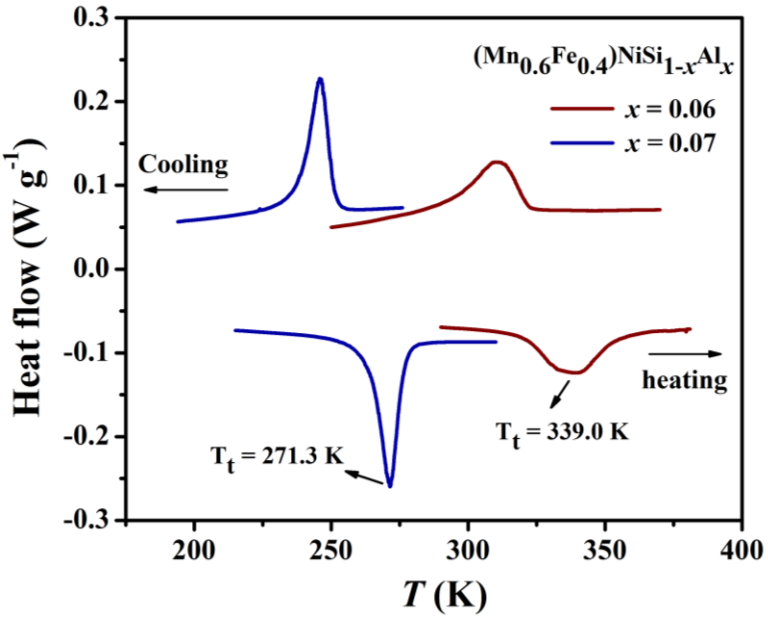

Figure 3.4: DSC heat flow curves for x = 0.06 and 0.07 samples during heating and cooling mode.

Isothermal field dependent magnetization (M-H) curves of x = 0.07 alloy for a maximum field up to 50 kOe are measured around T_t at 3 K interval during heating obeying discontinuous heating method [23] which are shown in **Fig. 3.5(a).** The heating cycle does not exhibit any field induced metamagnetic transition (FIMMT) which suggests that any first order transition does not take place during FM to PM transition and it is unusual the results obtained from M-T curves. Hence, 50 kOe magnetic field is not sufficient to produce first order MST during heating. For that, isothermal M-H curves of x = 0.07 alloy for a maximum field up to 50 kOe are measured around MST at selected temperatures with 3 K intervals in cooling mode obeying discontinuous cooling protocol [23] and are shown in **Fig. 3.5(b)**. The protocol is used in order to remove the field history effect of the sample. In this protocol, at first, the sample is

heated to a temperature (~300 K) in the paramagnetic region and then, under ZFC condition the sample cooled to a selected temperature (~265 K) for isothermal *M-H* measurement. Afterward, the sample is heated to ~300 K and then under ZFC condition cooled to a temperature, 3 K lowers than the previous one for *M-H* measurement. This procedure is followed for all the *M-H* curves measured within the temperature region of 265 K - 244 K at an interval of 3 K in cooling cycle. The presence of metamagnetic transition in the *M-H* curves indicates the field induced magnetostructural transition from the PM hexagonal phase to FM orthorhombic phase and the transition is first order type in nature.

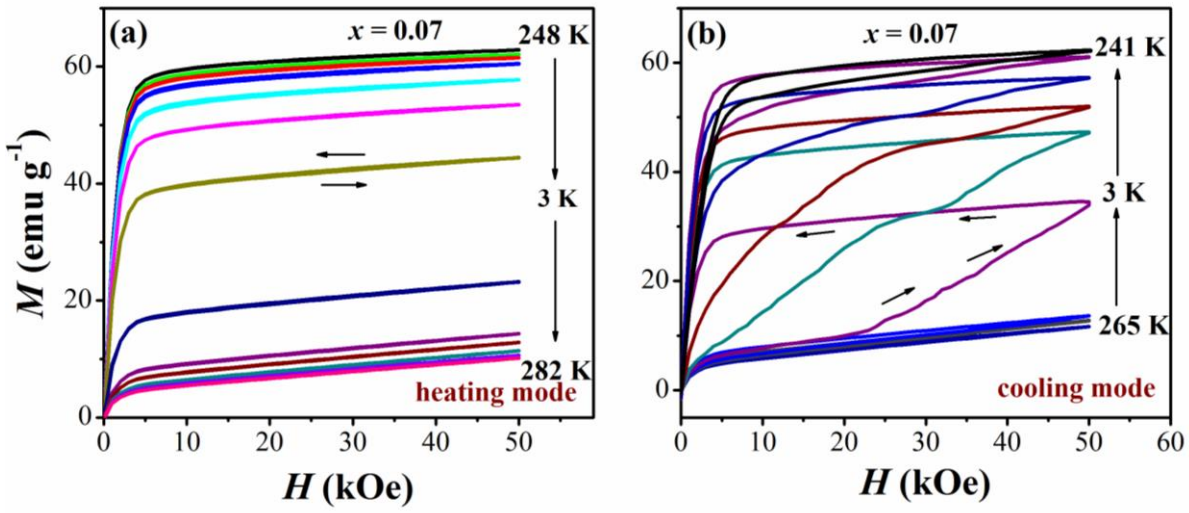

Figure 3.5: Isothermal *M-H* curve for $(Mn_{0.6}Fe_{0.4})NiSi_{0.93}Al_{0.07}$ alloy at selected temperatures with 3 K interval due to application of 50 kOe magnetic field during (a) heating mode and (b) cooling mode

Magnetocaloric properties of any magnetic material are solely associated with the nature of phase transition it undergoes. Therefore, to confirm the order of MST, Arrott plots (M^2 vs. H/M) are plotted for the alloy with x = 0.07 in heating as well as in cooling mode which are shown in **Fig. 3.6**. Based on Banerjee criteria, the slope of the Arrott plot across phase transition takes positive values for a second order transition whereas, for the first order phase transition, the slope of the Arrott plot would take

negative values. The heating mode does not represent the first order nature of MST. Instead, during the cooling mode, such an S-shaped curve present across the transition temperature indicates that the alloy undergoes a first order MST. Therefore, the cooling mode should be followed for the accurate measurement of magnetocaloric parameters for these studied materials.

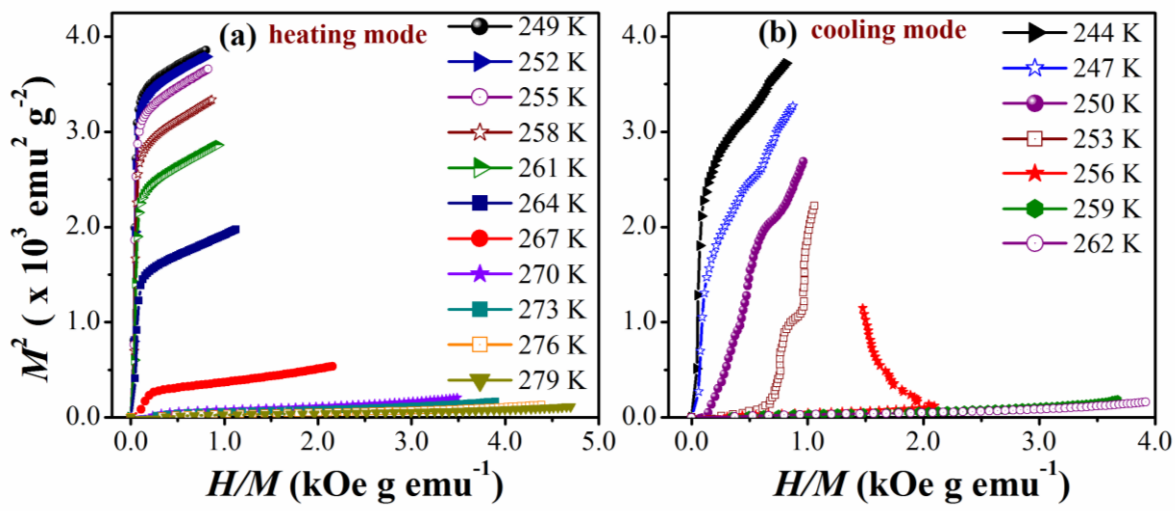

Figure 3.6: Arrott plot for $(Mn_{0.6}Fe_{0.4})NiSi_{0.93}Al_{0.07}$ alloy during (a) heating and (b) cooling mode

To check the viability of the investigated samples as magnetocaloric material, magnetic entropy change is estimated from isothermal *M-H* curves during cooling and field increasing modes using integrated Maxwell equation [24],

$$\Delta S_M(T, \Delta H) = \mu_0 \int_0^H \left(\frac{\partial M(H,T)}{\partial T}\right)_H dH \qquad (3.1)$$

where, μ_0 is the permeability of free space. *M*, *T,* and *H* are the magnetization of the sample, instantaneous temperature, and the applied magnetic field respectively. ΔS_M for the alloy with x = 0.07 as a function of temperature is shown in **Fig. 3.7** for a field variation of 0 – 50 kOe. The estimated peak value of ΔS_M for this alloy is −20.6 J kg^{-1} K^{-1} due to the field change of 50 kOe whereas, for the field change of 20 kOe, it is −9.3 J kg^{-1} K^{-1}. The abrupt change in magnetization across MST from PM to FM phase leads to a

large value of ΔS_M in this alloy. Moreover, ΔS_M is also calculated for heating mode, which is shown in the **inset of Fig. 3.7**. The estimated value of ΔS_M in heating mode is observed to be −35.1 J kg^{-1} K^{-1} which is much larger than the value estimated in cooling mode. During isotherms measurements in cooling mode, a magnetic field induced PM to FM transition occurs due to the application of 50 kOe magnetic field in the vicinity of the MST. However, no such field induced FM to PM transition takes place during heating mode and the sample remains either in FM/PM or in the mixed phase throughout the isothermal *M-H* measurements and as a result, the temperature evolution of the ferromagnetic phase might lead to overestimation of the magnetic entropy change during heating. Hence, cooling mode is preferable to calculate an accurate magnetic entropy change value for these similar materials.

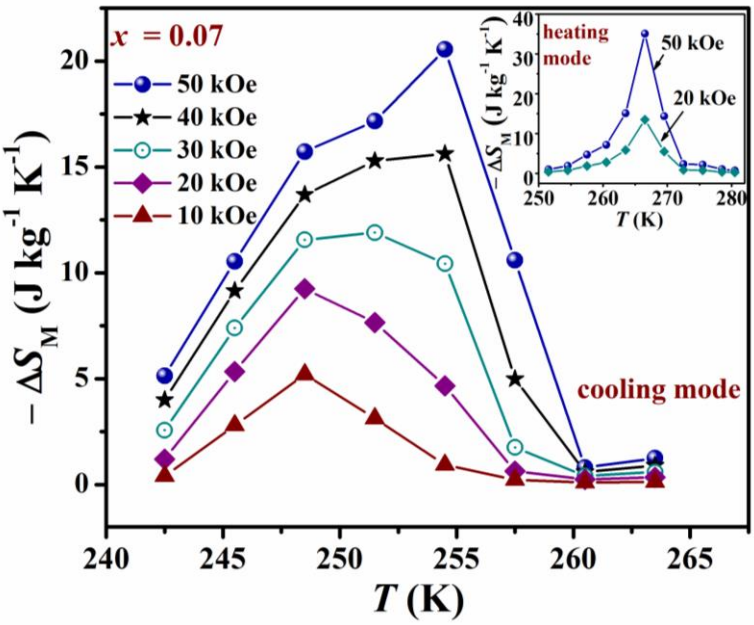

Figure 3.7: Magnetic entropy change (ΔS_M) estimated from isothermal *M-H* curve in cooling and field increasing mode as a function of temperature for the different field variation of x = 0.07 alloy. [Inset: ΔS_M as a function of temperature for x = 0.07 alloy estimated from isothermal *M-H* curve in heating mode]

Further, a comparison of ΔS_M value for the investigated materials in a lower field of 14 kOe is shown in **Fig. 3.8**. ΔS_M is estimated from the isothermal *M-H* curve in cooling and field increasing mode. These materials show large MCE response even at the low magnetic field. Here, ΔS_M reaches a maximum value of about −5.1 and −7.1 J kg^{-1} K^{-1} for the alloys with x = 0.06 and 0.07 respectively due to field change of 14 kOe only. For x = 0.08 alloy, it is expected that ΔS_M will be very low compared to the other two alloys as it shows only magnetic transition at 145 K. The peak value of $|\Delta S_M|$ for x = 0.07 alloy is comparable to other alloys with large MCE for the same field change of 50 kOe, such as $MnCoGeB_{0.02}$ (~47.3 J kg^{-1} K^{-1}) [17], $(MnNiSi)_{0.65}(Fe_2Ge)_{0.35}$ (~36.9 J kg^{-1} K^{-1}) [20], $Ni_{45.5}Co_2Mn_{37.5}Sn_{15}$ (~13.67 J kg^{-1} K^{-1}) [25] and $Ni_{45}Co_5Mn_{38}Sb_{12}$ (~34 J kg^{-1} K^{-1}) [26], $Ni_{35}Co_{15}Mn_{35}Ti_{15}$ (~ 18 J kg^{-1} K^{-1}) [27].

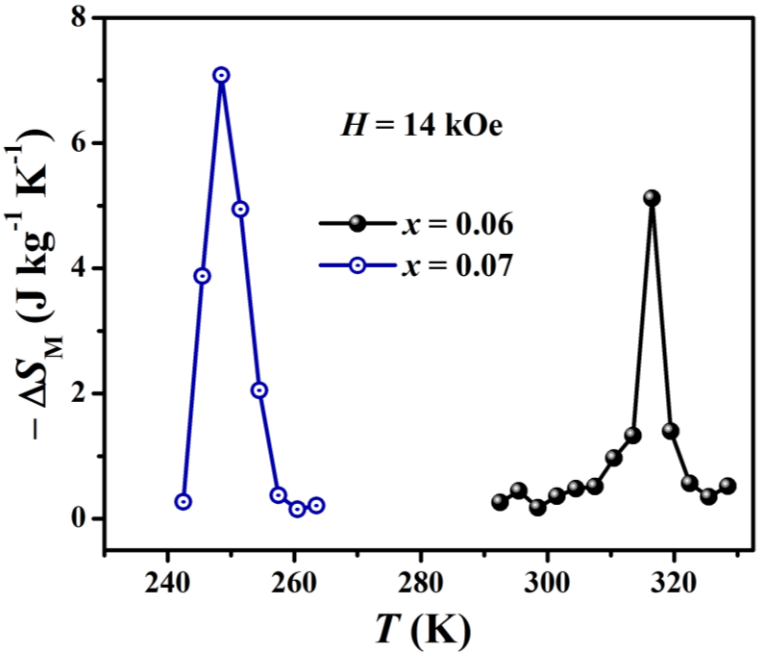

Figure 3.8: Magnetic entropy change (ΔS_M) estimated from isothermal *M-H* curve in cooling and field increasing mode as a function of temperature for x = 0.06 and x = 0.07 alloy due to the application of 14 kOe field.

Relative Cooling Power (RCP) is an important parameter in MCE studies that provides an idea about the efficiency of the material as a magnetic refrigerant. The

relation RCP $= \Delta S_M^{peak} \times \Delta T_{FWHM}$ is employed here to calculate the RCP value of the material. Here, ΔS_M^{peak} is the peak value of ΔS_M of a ΔS_M-T curve plotted for a specific field change and ΔT_{FWHM} stands for the temperature span of full width at half maxima of ΔS_M. The calculated value of RCP for the alloy with x = 0.07 in cooling mode is plotted as a function of an applied magnetic field which is shown in **Fig. 3.9**. The maximum value of RCP for 50 kOe magnetic field changes is about 249.2 J/kg whereas, for 20 kOe magnetic field changes it is 87.6 J/kg.

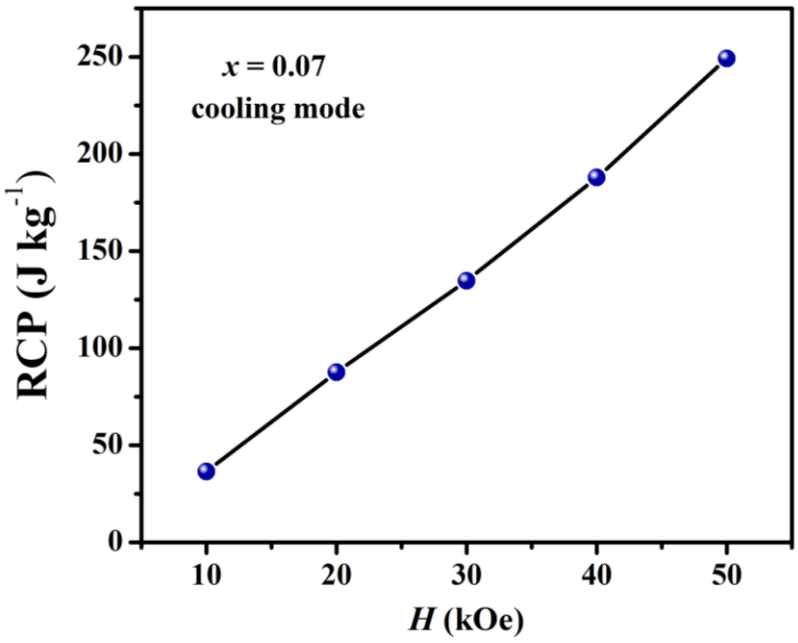

Figure 3.9: Relative cooling power (RCP) as a function of magnetic field change for x = 0.07 alloy in cooling mode

3.4 Conclusion

In summary, we have systematically investigated the tuning of magnetostructural transition from hexagonal Ni_2In-type structure to an orthorhombic TiNiSi-type structure near room temperature and the magnetocaloric properties across it by doping of Fe in place of Mn site and substituting Al for Si site of MnNiSi alloy. For a fixed doping of Fe, enhancement of Al substitution reduces the structural transition temperature

toward lower temperature. For a nominal composition of x = 0.07, the material exhibits the largest MCE response, ΔS_M about 20.6 J kg^{-1} K^{-1} with large RCP $\sim$ 249.2 J/kg due to a magnetic field change of 50 kOe. Cooling mode is favorable to estimate the accurate magnetic entropy changes of these similar types of materials. Our results suggest that the low-cost transition metal based alloy with x = 0.07 of this investigated series with remarkable MCE response can be considered as a promising candidate for magnetic refrigeration.

References

[1] K. Koyama, M. Sakai, T. Kanomata, and K. Watanabe, *Field-Induced Martensitic Transformation in New Ferromagnetic Shape Memory Compound $Mn_{1.07}Co_{0.92}Ge$*, Jpn. J. Appl. Phys. **43**, 8036 (2004).

[2] S. Lin, O. Tegus, E. Bruck, W. Dagula, T. J. Gortenmulder, and K. H. J. Buschow, *Structural and Magnetic Properties of $MnFe_{1-x}Co_xGe$ Compounds*, IEEE Trans. Magn. **42**, 3776 (2006).

[3] Y. K. Fang, C. C. Yeh, C. W. Chang, W. C. Chang, M. G. Zhu, and W. Li, *Large Low-Field Magnetocaloric Effect in $MnCo_{0.95}Ge_{1.14}$ Alloy*, Scr. Mater. **57**, 453 (2007).

[4] Z.-Y. Wei, E.-K. Liu, Y. Li, G.-Z. Xu, X.-M. Zhang, G.-D. Liu, X.-K. Xi, H.-W. Zhang, W.-H. Wang, G.-H. Wu, and X.-X. Zhang, *Unprecedentedly Wide Curie-Temperature Windows as Phase-Transition Design Platform for Tunable Magneto-Multifunctional Materials*, Adv. Electron. Mater. **1**, 1500076 (2015).

[5] T. Samanta, I. Dubenko, A. Quetz, S. Stadler, and N. Ali, *Giant Magnetocaloric Effects near Room Temperature in $Mn_{1-x}Cu_xCoGe$*, Appl. Phys. Lett. **101**, 242405 (2012).

[6] E. Liu, W. Wang, L. Feng, W. Zhu, G. Li, J. Chen, H. Zhang, G. Wu, C. Jiang, H. Xu, and F. de Boer, *Stable Magnetostructural Coupling with Tunable Magnetoresponsive Effects in Hexagonal Ferromagnets*, Nat. Commun. **3**, 873 (2012).

[7] K. G. Sandeman, R. Daou, S. Özcan, J. H. Durrell, N. D. Mathur, and D. J. Fray, *Negative Magnetocaloric Effect from Highly Sensitive Metamagnetism in $CoMnSi_{1-x}Ge_x$*, Phys. Rev. B **74**, 224436 (2006).

[8] E. K. Liu, H. G. Zhang, G. Z. Xu, X. M. Zhang, R. S. Ma, W. H. Wang, J. L. Chen, H. W. Zhang, G. H. Wu, L. Feng, and X. X. Zhang, *Giant Magnetocaloric Effect in Isostructural MnNiGe-CoNiGe System by Establishing a Curie-Temperature Window*, Appl. Phys. Lett. **102**, 122405 (2013).

[9] C. L. Zhang, D. H. Wang, Q. Q. Cao, Z. D. Han, H. C. Xuan, and Y. W. Du, *Magnetostructural Phase Transition and Magnetocaloric Effect in Off-Stoichiometric $Mn_{1.9-x}Ni_xGe$ Alloys*, Appl. Phys. Lett. **93**, 122505 (2008).

[10] T. Samanta, D. L. Lepkowski, A. U. Saleheen, A. Shankar, J. Prestigiacomo, I. Dubenko, A. Quetz, I. W. H. Oswald, G. T. McCandless, J. Y. Chan, P. W. Adams, D. P.

Young, N. Ali, and S. Stadler, *Hydrostatic Pressure-Induced Modifications of Structural Transitions Lead to Large Enhancements of Magnetocaloric Effects in MnNiSi-Based Systems*, Phys. Rev. B **91**, 020401(R) (2015).

[11] E. Liu, Y. Du, J. Chen, W. Wang, H. Zhang, and G. Wu, *Magnetostructural Transformation and Magnetoresponsive Properties of $MnNiGe_{1-x}Sn_x$ Alloys*, IEEE Trans. Magn. **47**, 4041 (2011).

[12] Y. Li, Z. Y. Wei, E. K. Liu, G. D. Liu, H. Z. Luo, X. K. Xi, W. H. Wang, and G. H. Wu, *Coupled Magnetic and Structural Transitions in Fe-Doped MnNiSi Compounds*, IEEE Trans. Magn. **51**, 2502004 (2015).

[13] N. T. Trung, V. Biharie, L. Zhang, L. Caron, K. H. J. Buschow, and E. Brück, *From Single- to Double- First-Order Magnetic Phase Transition in Magnetocaloric $Mn_{1-x}Cr_xCoGe$ Compounds*, Appl. Phys. Lett. **96**, 162507 (2010).

[14] C. L. Zhang, D. H. Wang, Z. D. Han, B. Qian, H. F. Shi, C. Zhu, J. Chen, and T. Z. Wang, *The Tunable Magnetostructural Transition in MnNiSi-FeNiGe System*, Appl. Phys. Lett. **103**, 132411 (2013).

[15] S. C. Ma, Y. X. Zheng, H. C. Xuan, L. J. Shen, Q. Q. Cao, D. H. Wang, Z. C. Zhong, and Y. W. Du, *Large Roomtemperature Magnetocaloric Effect with Negligible Magnetic Hysteresis Losses in $Mn_{1-x}V_xCoGe$ Alloys*, J. Magn. Magn. Mater. **324**, 135 (2012).

[16] W. Bazela, A. Szytuła, J. Todorović, Z. Tomkowicz, and A. Zięba, *Crystal and Magnetic Structure of NiMnGe*, Phys. Status Solidi **38**, 721 (1976).

[17] N. T. Trung, L. Zhang, L. Caron, K. H. J. Buschow, and E. Brück, *Giant Magnetocaloric Effects by Tailoring the Phase Transitions*, Appl. Phys. Lett. **96**, 172504 (2010).

[18] V. Johnson and C. G. Frederick, *Magnetic and Crystallographic Properties of Ternary Manganese Silicides with Ordered Co_2P Structure*, Phys. Status Solidi **20**, 331 (1973).

[19] Y. Li, Z. Y. Wei, E. K. Liu, G. D. Liu, S. G. Wang, W. H. Wang, and G. H. Wu, *Structural Transitions, Magnetic Properties, and Electronic Structures of Co(Fe)-Doped MnNiSi Compounds*, J. Appl. Phys. **117**, 17C117 (2015).

[20] C. L. Zhang, H. F. Shi, E. J. Ye, Y. G. Nie, Z. D. Han, B. Qian, and D. H. Wang, *Magnetostructural Transition and Magnetocaloric Effect in $MnNiSi$-Fe_2Ge System*,

Appl. Phys. Lett. **107**, 212403 (2015).

[21] T. Samanta, D. L. Lepkowski, A. U. Saleheen, A. Shankar, J. Prestigiacomo, I. Dubenko, A. Quetz, I. W. H. Oswald, G. T. McCandless, J. Y. Chan, P. W. Adams, D. P. Young, N. Ali, and S. Stadler, *Effects of Hydrostatic Pressure on Magnetostructural Transitions and Magnetocaloric Properties in* $(MnNiSi)_{1-x}(FeCoGe)_x$, J. Appl. Phys. **117**, 123911 (2015).

[22] Y. T. Prabhu, K. V. Rao, V. S. S. Kumar, and B. S. Kumari, *X-Ray Analysis by Williamson-Hall and Size-Strain Plot Methods of ZnO Nanoparticles with Fuel Variation*, World J. Nano Sci. Eng. **04**, 21 (2014).

[23] A. Ghosh, P. Sen, and K. Mandal, *Measurement Protocol Dependent Magnetocaloric Properties in a Si-Doped Mn-Rich Mn-Ni-Sn-Si off-Stoichiometric Heusler Alloy*, J. Appl. Phys. **119**, 183902 (2016).

[24] K. A. GschneidnerJr, V. K. Pecharsky, and A. O. Tsokol, *Recent Developments in Magnetocaloric Materials*, Reports Prog. Phys. **68**, 1479 (2005).

[25] S. Arumugam, S. Ghosh, A. Ghosh, U. Devarajan, M. Kannan, L. Govindaraj, and K. Mandal, *Effect of Hydrostatic Pressure on the Magnetic, Exchange Bias and Magnetocaloric Properties of* $Ni_{45.5}Co_2Mn_{37.5}Sn_{15}$, J. Alloys Compd. **712**, 714 (2017).

[26] A. K. Nayak, K. G. Suresh, and A. K. Nigam, *Giant Inverse Magnetocaloric Effect near Room Temperature in Co Substituted NiMnSb Heusler Alloys*, J. Phys. D. Appl. Phys. **42**, 035009 (2009).

[27] Z. Y. Wei, E. K. Liu, J. H. Chen, Y. Li, G. D. Liu, H. Z. Luo, X. K. Xi, H. W. Zhang, W. H. Wang, and G. H. Wu, *Realization of Multifunctional Shape-Memory Ferromagnets in All- d -Metal Heusler Phases*, Appl. Phys. Lett. **107**, 022406 (2015).

Chapter 4 | Magnetostructural transition and Giant magnetocaloric effect in $(MnNiSi)_{1-x}(FeCoGa)_x$ alloys

This chapter describes the tuning of magnetostructural transition and the giant magnetocaloric properties across that transition around room temperature in low-cost transition metal based $(MnNiSi)_{1-x}(FeCoGa)_x$ (x = 0.15, 0.16 and 0.17) alloys and our result indicates that these materials are potential candidates for room temperature magnetic refrigerator.

4.1 Preamble

Energy-efficient and eco-friendly magnetic refrigeration (MR) technology based on MCE, which has enormous potential to replace the conventional vapor compression technology, is expected to be applicable in the solid state-based modern refrigeration devices [1,2]. In this regard, it requires potential refrigerant materials with giant MCE response. The materials such as $Gd_5Si_2Ge_2$ [3], $La(Fe,Si)_{13}$-based alloys [4–6], Mn-Fe-based compounds [6,7], and Ni-Mn-based Heusler alloys [8–12] are being already proposed as promising refrigerant material because of their excellent MCE responses around room temperature. All these alloys are accompanied with a magnetic field induced structural transition from antiferromagnetic (AFM) or paramagnetic (PM) to ferromagnetic (FM) phase leading to a strongly coupled magnetostructural transition (MST) which is associated with significant changes in unit cell volume and therefore, a sharp change in magnetization across the phase transition. However, it is a great challenge to discover such giant magnetocaloric materials with transition metal based, less expensive, earth-abundant, and nontoxic elements.

Intermetallic compounds with the general formula Mn*TX* (*T* = Ni, Co and *X* = Si, Ge) have recently grabbed considerable attention to the researchers because of their potential to show interesting multifunctional properties such as temperature induced MST, magnetic shape memory effect, large MCE, giant magnetoresistance, volume anomalies and so on [13–17]. All the above-mentioned stoichiometric materials are found to exhibit a second order magnetic transition followed by a first order structural transformation from low temperature orthorhombic to a high temperature hexagonal structure in the paramagnetic state with no significant changes in magnetization. Magnetoresponsive properties such as MCE and magnetoresistance are associated solely with a change in magnetization. Therefore, shifting of the structural transition of these materials to the ferromagnetic region or coupling it with magnetic transition near room temperature may be the best option to enrich them with the above-mentioned properties. In order to obtain MST for these compounds, several effective methods such as elemental substitution, off-stoichiometry, isostructural substitution, heat treatment, or application of external parameters like hydrostatic pressure are introduced [14,18–

22]. MnNiGe and MnCoGe based systems have closeness in between their magnetic and structural transitions and thus extensively studied materials to achieve MST using the above-mentioned techniques. Stoichiometric MnNiGe [23] shows magnetic transition at Neel temperature (T_N) ~ 346 K and structural transition at T_M ~ 470 K whereas MnCoGe [15] shows magnetic transition at Curie temperature (T_C) ~ 355 K and structural transitions at T_M ~ 650 K.

Besides the above-mentioned systems, ferromagnetic MnNiSi [24] system also exhibits second order FM to PM transition at T_C ~ 622 K and beyond that temperature, a structural transformation from TiNiSi-type orthorhombic to Ni_2In-type hexagonal structure at a higher temperature of about T_M ~ 1210 K. Hence, it is difficult to obtain MST at room temperature for this compound. However, considering the relatively low-cost of raw materials, it will be commercially viable to use them for domestic purposes. In this present work, it is observed that by alloying MnNiSi system with FeCoGa, the hexagonal structure is stabilized near room temperature from 1210 K and for a nominal composition of $(MnNiSi)_{1-x}(FeCoGa)_x$ (x = 0.15 and 0.16) MST is achieved at around room temperature. With subsequent doping for x = 0.17, MST decouples into two separate transitions, structural and magnetic, though the transitions are realized to couple with enhancing the applied magnetic field. Substitution of Fe with a relatively lower atomic radius in place of Mn increases the orthorhombic distortion of the system and stabilizes the hexagonal phase at a lower temperature, resulting both T_C and T_M reduce towards room temperature with lower saturation magnetization [17]. To compensate for the reduction in magnetization, Co can be doped in place of Ni, where Co enhances the ferromagnetic interaction to the system. Ga having a much larger atomic radius than Si again enhances orthorhombic distortion in a faster way to the system which couples T_C and T_M and as a result, MST is obtained in the vicinity of room temperature. The alloys with x = 0.15, 0.16, and 0.17 are found to exhibit isothermal magnetic entropy change (ΔS_M) as large as about −25 J kg^{-1} K^{-1} at 323 K, ~ −31.1 J kg^{-1} K^{-1} at 281 K, and ~ −23.8 J kg^{-1} K^{-1} at 213 K respectively due to a field change of ΔH = 50 kOe. These low-cost materials may be considered as promising candidates for magnetic refrigeration around room temperature due to their giant magnetocaloric properties

with significantly large relative cooling power (RCP = 191.8, 209.6, and 139.2 J/kg respectively for x = 0.15, 0.16, and 0.17 due to ΔH = 50 kOe).

4.2 Experimental

Polycrystalline $(MnNiSi)_{1-x}(FeCoGa)_x$ (x = 0.15, 0.16 and 0.17) samples are prepared by conventional arc-melting technique under 4N purity of argon atmosphere using appropriate amounts of high purity constituent elements from Sigma Aldrich. An additional amount of 3% Mn is taken to compensate for its weight loss during melting. The samples are turned and re-melted several times (seven to eight times) to maintain the compositional homogeneity. All the as-prepared samples are sealed in an evacuated quartz tube and annealed at 1173 K for 96 hours, followed by quenching into ice water. The Compositions of annealed samples are checked by energy dispersive analysis of X-ray (EDAX) and the analyzed compositions are found to be very similar to the starting compositions. X-ray diffraction (XRD) patterns of all the samples are obtained using PANalytical X'Pert PRO with Cu-K_α radiation (wavelength, λ = 1.54 Å). We have prepared the powder form of the annealed samples using a mortar and pastel for XRD measurement. Magnetic measurements such as temperature dependent magnetization and field dependent magnetization are performed using SQUID (MPMS, Quantum Design) with a maximum applied magnetic field of 50 kOe. Differential scanning calorimetry (DSC) heat flow data are measured in cooling mode up to the 10^{th} cycle at a ramp rate of 10 K/min.

4.3 Results and Discussion

Figure 4.1 depicts the X-ray diffraction patterns at room temperature ($RT \sim 300$ K) for all the investigated alloys. On enhancing the doping amount of $(FeCoGa)_x$ to $(MnNiSi)_{1-x}$, from x = 0.15 to 0.17, the structural phase transformation from orthorhombic to hexagonal is observed which indicates the shifting of the structural transition towards room temperature from the structural transition temperature of parent MnNiSi alloy at ~1210 K. Orthorhombic phase with some traces of hexagonal phase is observed for the

x = 0.15 alloy whereas x = 0.16 is found to show a dominating hexagonal phase and x = 0.17 displays pure hexagonal phase. The unit cell lattice parameters in the orthorhombic phase for the alloy with x = 0.15 are found to be a_{ortho} = 5.835 Å, b_{ortho} = 3.71 Å, and c_{ortho} = 6.905 Å whereas for x = 0.17 in the hexagonal phase are a_{hex} = 3.982 Å and c_{hex} = 5.179 Å.

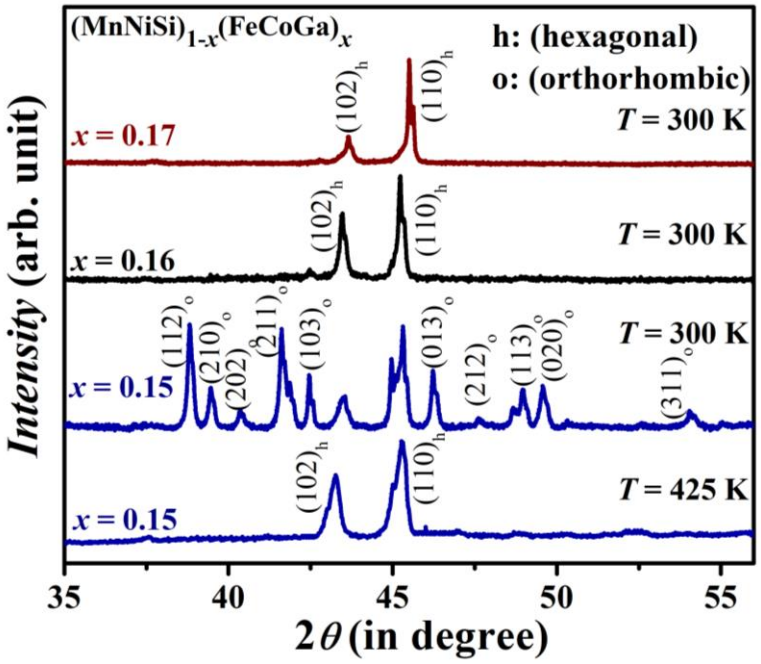

Figure 4.1: X-ray diffraction pattern for $(MnNiSi)_{1-x}(FeCoGa)_x$ (x = 0.15, 0.16, and 0.17) alloys at 300 K and X-ray diffraction pattern for x = 0.15 alloy at 425 K. Here 'o' and 'h' stand for orthorhombic and hexagonal phases respectively.

From the crystallographic study [23], the orthorhombic unit cell is related to the hexagonal unit cell through the following relation, $a_{ortho} = c_{hex}$, $b_{ortho} = a_{hex}$, and $c_{ortho} = \sqrt{3}\, a_{hex}$. Here the decrease in c_{hex}/a_{hex} (or a_{ortho}/b_{ortho}) ratio from 1.573 for x = 0.15 to 1.301 for x = 0.17 can distort the geometry of the orthorhombic structure and makes the hexagonal structure more stable at a lower temperature [26], resulting in the decrease in structural transition temperature with increasing x. Further, an X-ray diffraction pattern is carried out at 425 K for the alloy with x = 0.15 (shown in **Fig. 4.1**) and it is

found to exhibit hexagonal phase only. A large change in unit cell volume about −3.18 % is observed across the structural transformation from high temperature hexagonal phase to low temperature orthorhombic phase.

The temperature dependence of Zero field cooled (ZFC) and Field cooled (FC) magnetization (*M-T* curves) within 100 K - 400 K in presence of 500 Oe magnetic field for $(MnNiSi)_{1-x}(FeCoGa)_x$ (x = 0.15, 0.16 and 0.17) alloys are shown in **Fig. 4.2**. On increasing the doping amount from x = 0.15 to 0.16, the magnetostructural transition temperature (T_t), estimated from the plot of $dM/dT - T$ in the heating mode, is found to shift from $\sim$ 342 K to a lower temperature of $\sim$ 293 K. The presence of thermal hysteresis between heating and cooling cycles in *M-T* curve signifies the coincidence of both the magnetic transition from FM to PM and structural transition from low temperature orthorhombic to high temperature hexagonal at the same temperature, which leads to a first order transition. On further enhancement of doping amount to x = 0.17, MST decouples, and as a result, separated structural transformation in the ferromagnetic region and magnetic transition are observed at T_M = 224 K and T_C = 234 K respectively. However, the separated structural and magnetic transitions are found to coincide with enhancing the magnetic field which is shown in the **inset of Fig. 4.2**. The width of thermal hysteresis between ZFC and FC curves during MST are found to be 23 K and 14 K for the alloys with x = 0.15 and 0.16 respectively. Therefore thermal hysteresis decreases significantly with the increase in doping amount and it is minimum for x = 0.16 which makes it suitable for the application in room temperature magnetic refrigeration. Moreover, T_t for this investigated compound, $(MnNiSi)_{1-x}(FeCoGa)_x$, is tunable from 224 K - 342 K with a broad temperature window of 118 K which will be beneficial for magnetic refrigeration associated with wide and controllable operating temperature.

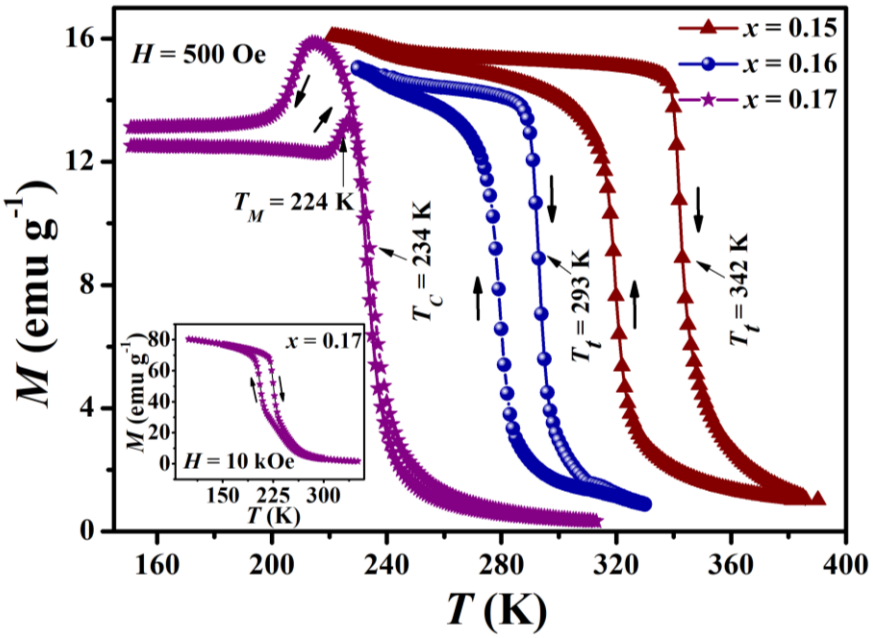

Figure 4.2: *M-T* curves for $(MnNiSi)_{1-x}(FeCoGa)_x$ (x = 0.15, 0.16, and 0.17) alloys in presence of 500 Oe magnetic field. [Inset: *M-T* curve for the alloy with x = 0.17 in presence of 10 kOe field]

Isothermal field dependent magnetization (*M-H*) curves are measured across T_t in heating mode for the sample with x = 0.16 up to a maximum field of 50 kOe and are shown in **Fig. 4.3**. Heating mode is not associated with any field induced metamagnetic transition (FIMMT), resulting in no first order transition takes place from FM to PM phase and it is unusual with the results as obtained from the *M-T* curves. Here, the change of 50 kOe magnetic field is not sufficient to induce FIMMT for these alloys in heating. Therefore, isothermal *M-H* curves are measured during cooling mode for all the samples from PM hexagonal phase to FM orthorhombic phase and are shown in **Fig. 4.4**. To remove the field history effect of the samples, the loop process methods are followed to measure the isotherms [26]. In this loop process method, at first, the sample is heated to a temperature in the PM region and then, under ZFC condition the sample cooled to a selected temperature for isothermal *M-H* measurement. Afterward, the sample is again heated to the temperature in the PM region and then under ZFC condition cooled to the next targeted temperature for *M-H* measurement. This procedure is followed for all the isothermal *M-H* curves shown in **Fig. 4.4**. The graph

clearly shows the observation of FIMMT in the vicinity of the magnetostructural transition temperature which also confirms the first order nature of the MST. The low temperature *M-H* measurement as shown in **Fig. 4.4(d)** is performed at 5 K for all the alloys which shows a typical ferromagnetic ordering. The saturation magnetization (M_S) for the alloy with x = 0.17 due to field change of 50 kOe is found to be ~104.5 emu/g (or ~ 2.79 μ_B/f.u.), which is larger than its parent alloy, MnNiSi [24] (~2.62 μ_B/f.u.).

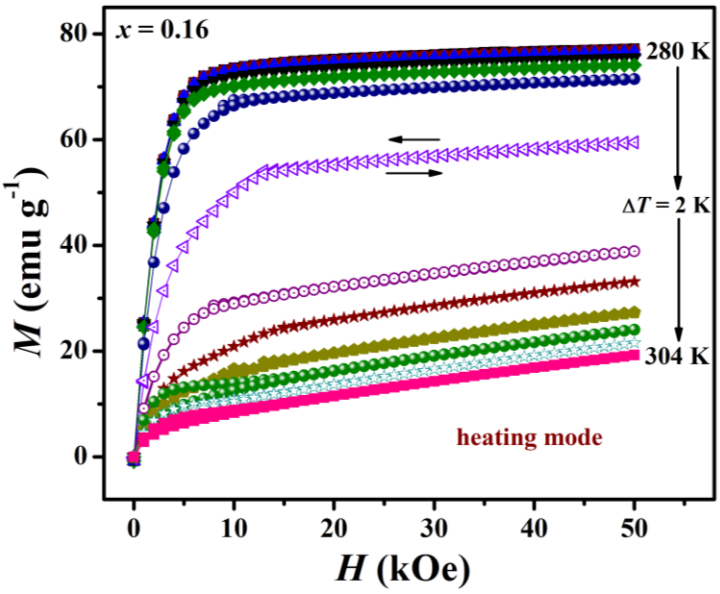

Figure 4.3: Isothermal *M-H* curves during heating mode in the temperature regime of 280 K - 304 K for the alloy with x = 0.16

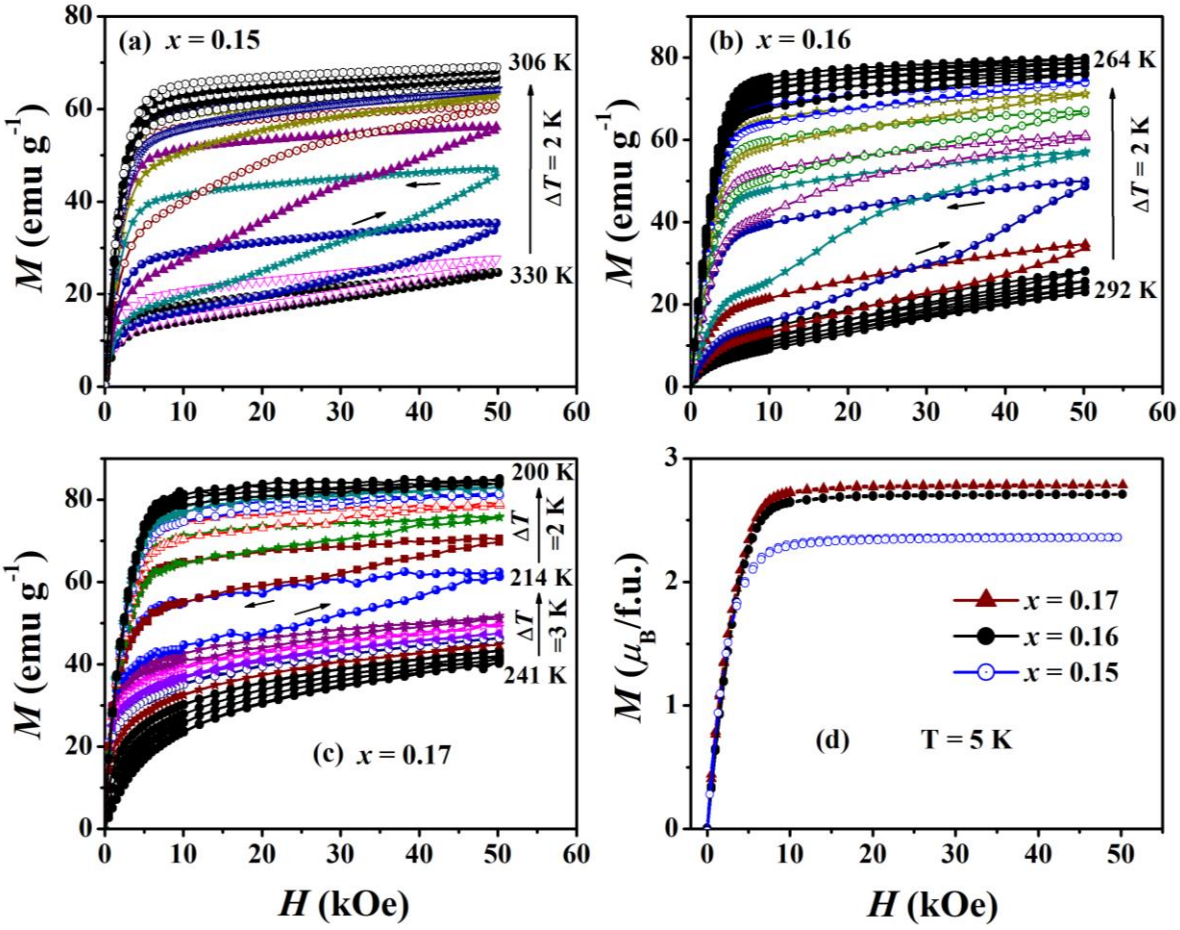

Figure 4.4: Isothermal *M-H* curves at a minimum temperature interval (Δ*T*) of 2 K in cooling mode (PM to FM phase) for the alloy with (a) *x* = 0.15 (b) *x* = 0.16 and (c) *x* = 0.17. (d) Field dependence of magnetization (*M* vs. *H*) at 5 K for all the investigated alloys

Isothermal magnetic entropy change (ΔS_M), an essential parameter of MCE, can be estimated from the isothermal *M-H* curves measured at discrete stable temperatures in the vicinity of their respective MST during cooling mode using the Maxwell equation [1],

$$\Delta S_M(T, \Delta H) = \mu_0 \int_0^H \left(\frac{\partial M(H,T)}{\partial T}\right)_H dH \qquad (4.1)$$

where, μ_0 is the permeability of free space. *M*, *T,* and *H* are the magnetization of the sample, instantaneous temperature, and the applied magnetic field respectively. The

ΔS_M as calculated using the above equation is plotted as a function of temperature for all the investigated alloys in **Fig. 4.5** for a magnetic field change of 10 - 50 kOe. The estimated peaks of ΔS_M are found to be as large as about −25 J kg^{-1} K^{-1} at 323 K, ∼ −31.1 J kg^{-1} K^{-1} at 281 K, and ∼ −23.8 J kg^{-1} K^{-1} at 213 K for the alloys with x = 0.15, 0.16, and 0.17 respectively, due to ΔH = 50 kOe which are associated with the first order MST. The significant jump in magnetization across MST arises from the lattice as well as magnetic structure changes in the coupled transition, developing a giant magnetic entropy change in these investigated alloys. Moreover, ΔS_M for the alloy with x = 0.16 is calculated in heating mode and the estimated value is observed to be −51.2 J kg^{-1}K^{-1} (shown in the **inset of Fig. 4.5(b)**) which is much higher compared to the value obtained during cooling mode. During *M-H* measurements in cooling mode field induced PM to FM transition takes place due to the application of 50 kOe magnetic field in the vicinity of MST. However no such field induced FM to PM transition takes place during heating and the samples remain either in ferromagnetic/paramagnetic or in the mixed phase throughout the isothermal *M-H* measurements and as a result, the temperature evolution of the ferromagnetic phase might be overestimating the magnetic entropy change in heating. Therefore, the cooling mode is preferable to calculate the accurate magnetic entropy change value for these similar materials. The peak values of ΔS_M of the investigated samples have been compared with other promising refrigerant materials in **Table 4.1**. These transition based materials show excellent MCE response in a board and tunable temperature region with a minimum peak value of ΔS_M as 23.8 J kg^{-1} K^{-1} at 213 K due to ΔH = 50 kOe.

Apart from large magnetic entropy change, relative cooling power (RCP) is an important parameter which defines the cooling efficiency of a magnetic refrigerant material. RCP of these investigated alloys have been estimated from the following equation, RCP $= |\Delta S_M^{peak}| \times \Delta T_{FWHM}$, where, ΔS_M^{peak} is the peak of ΔS_M of a ΔS_M -T curve and ΔT_{FWHM} stands for the temperature range of full width at half maxima of ΔS_M (**Fig. 4.5**). The estimated RCPs are plotted with the magnetic field change in **Fig. 4.5(d)** and the maximum RCPs due to field change of 50 kOe are found to be 191.8, 209.6 and 139.2 J/kg for the alloys with x = 0.15, 0.16, and 0.17 respectively.

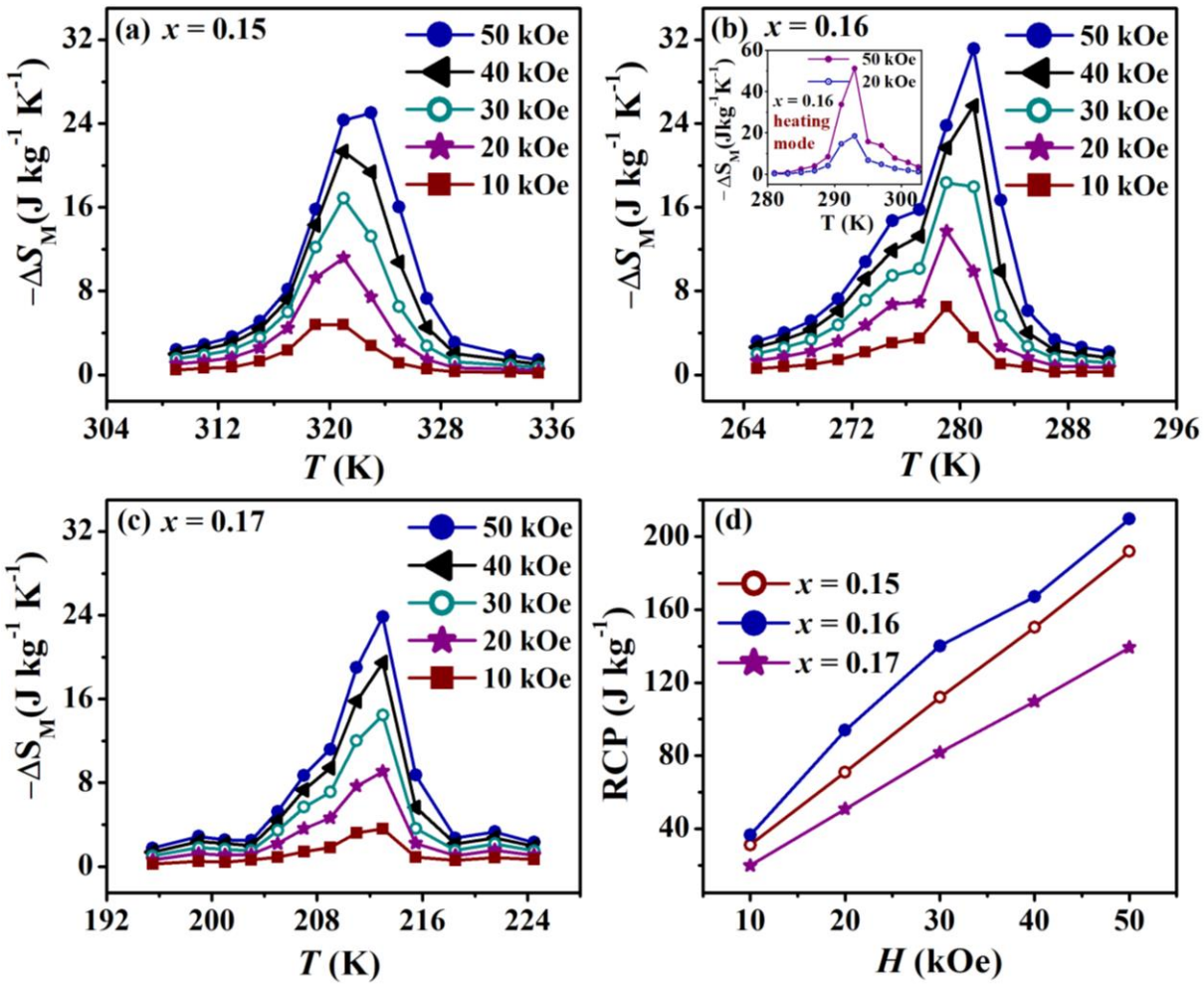

Figure 4.5: Magnetic entropy change (ΔS_M) as a function of temperature due to different field variation for the alloys with (a) x = 0.15 (b) x = 0.16 [Inset: the estimated ΔS_M for x = 0.16 in heating mode due to field change of 20 and 50 kOe] and (c) x = 0.17 during cooling and field increasing mode. (d) Relative cooling power (RCP) as a function of magnetic field change for x = 0.15, 0.16 and 0.17 alloys

Here, these investigated materials exhibit a large change in unit cell volume across the magnetostructural transition that causes a large change in magnetization resulting, in a giant value of ΔS_M. At the same time, the mechanical stability of these materials is reduced when the samples undergo the structural transition. Hence, to check the effect of mechanical stability on the MCE response of the materials, we have

measured DSC heat flow data of the sample with x = 0.15 in the vicinity of MST and repeated the measurement up to the 10th thermal cycle which is shown in **Fig. 4.6**. It is clear from the figure that despite a change in its mechanical properties due to repeated thermal cycles, the value of the entropy change remains the same. Furthermore, we have prepared the powder form of the sample using a mortar-pestle and repeated the heat flow measurement which also exhibits a similar response. Therefore, it can be concluded that the mechanical instability does not change the MCE response of the material. However, some binding material such as epoxy can be used to enhance mechanical stability if required.

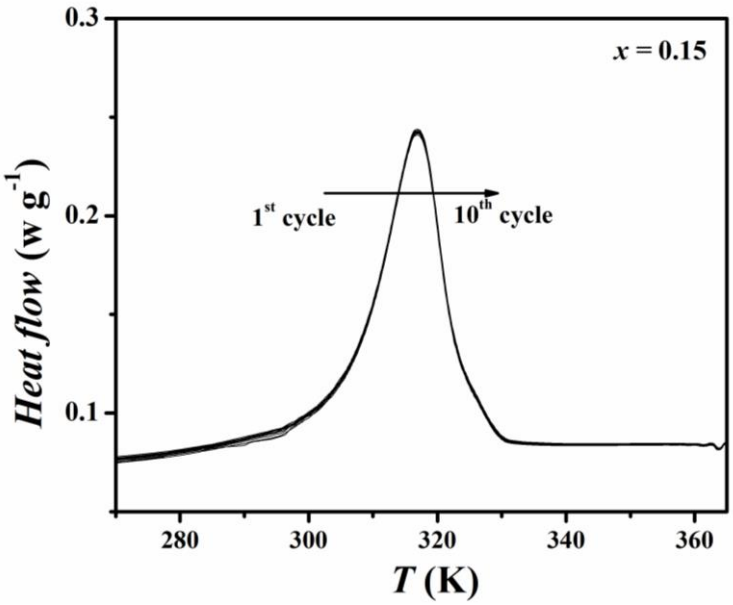

Figure 4.6: DSC heat flow curve of x = 0.15 alloy and repeated up to the 10th cycle in the vicinity of MST.

From the application point of view, the refrigerant material composed of transition metal based low-cost and earth-abundant elements will be commercially cost-effective. In comparison with Mn*TX*-based intermetallic compounds such as MnNiGe- [14,16], MnCoGe- [15,20] and other MnNiSi-based [18,19,21] systems which also exhibit first order MST near room temperature, our investigated system $(MnNiSi)_{1-x}(FeCoGa)_x$ is Ge free and contains very low doping amount of Ga, resulting in the

materials very cheap. Thus the present system made of low-cost abundant materials with large M_S, tunable MST, giant MCE response, and large RCP will be highly attractive for implementation in room temperature magnetic refrigeration technology.

Table 4.1: Comparison of the peak value of isothermal magnetic entropy change $\left(\Delta S_M^{peak}\right)$ due to ΔH = 50 kOe and the temperature where ΔS_M is maximum (T_{peak}) of $(MnNiSi)_{1-x}(FeCoGa)_x$ (x = 0.15 - 0.17) alloys with other promising refrigerant materials.

Materials	$\lvert\Delta S_M^{peak}\rvert$ **(J kg^{-1} K^{-1})**	T_{peak} **(K)**	**References**
Gd	~10.2	294	[27]
$Gd_5Ge_2Si_2$	~18.5	278	[3]
$La(Fe_{0.89}Si_{0.11})_{13}H_{1.3}$	~28.0	291	[4]
$MnFeP_{0.45}As_{0.55}$	~18	308	[28]
$Ni_{40}Co_{10}Mn_{40}Sn_{10}$	~14.9	288	[29]
$Mn_{46}Ni_{39.5}Sn_{10}Si_{4.5}$	~20.0	205	[30]
$Ni_{45}Co_5Mn_{38}Sb_{12}$	~34.0	262	[31]
$Ni_{50}Mn_{37}Sn_{13}$	~18.0	299	[8]
$Ni_{55.2}Mn_{18.6}Ga_{26.2}$	~20.4	317	[32]
$MnNi_{0.77}Fe_{0.23}Ge$	~19.0	267	[16]
$Mn_{0.82}Fe_{0.18}NiGe$	~31.0	205	
$Mn_{0.6}Fe_{0.4}NiSi_{0.93}Al_{0.07}$	~20.6	255	[22]
$Mn_{0.89}Cr_{0.11}CoGe$	~27.7	292	[33]
$(MnNiSi)_{1-x}(FeCoGa)_x$			Present Work
x = 0.15	~25.0	323	
x = 0.16	~31.1	281	
x = 0.17	~23.8	213	

4.4 Conclusion

In summary, the magnetostructural phase transition from a paramagnetic hexagonal to a ferromagnetic orthorhombic structure within a well regulated broad temperature region of 224 K - 342 K surrounding room temperature along with tunable giant magnetocaloric properties are observed in $(MnNiSi)_{1-x}(FeCoGa)_x$ (x = 0.15 - 0.17) alloys. The alloys with x = 0.15, 0.16, and 0.17 show significantly large ΔS_M of about −25, −31.1,

and −23.8 J kg^{-1} K^{-1} respectively for the field change of ΔH = 50 kOe. Here, x = 0.17 is the maximal doping content to keep the magnetostructural transition coupled for this system as the higher doping level splits it into two separate transitions. Moreover, the cooling mode is found to be preferred to estimate the precise magnetic entropy change for this type of material. The investigated compound, $(MnNiSi)_{1-x}(FeCoGa)_x$, can be a very promising refrigerant material for room temperature nature-friendly magnetic refrigeration technology because of its tunable giant magnetocaloric properties around room temperature associated with the large relative cooling power.

References

[1] K. A. GschneidnerJr, V. K. Pecharsky, and A. O. Tsokol, *Recent Developments in Magnetocaloric Materials*, Reports Prog. Phys. **68**, 1479 (2005).

[2] L. Mañosa and A. Planes, *Materials with Giant Mechanocaloric Effects: Cooling by Strength*, Adv. Mater. **29**, 1603607 (2017).

[3] V. K. Pecharsky and K. A. Gschneidner, Jr., *Giant Magnetocaloric Effect in* $Gd_5(Si_2Ge_2)$, Phys. Rev. Lett. **78**, 4494 (1997).

[4] A. Fujita, S. Fujieda, Y. Hasegawa, and K. Fukamichi, *Itinerant-Electron Metamagnetic Transition and Large Magnetocaloric Effects in* $La(FexSi_{1-x})_{13}$ *Compounds and Their Hydrides*, Phys. Rev. B **67**, 104416 (2003).

[5] J. Liu, J. D. Moore, K. P. Skokov, M. Krautz, K. Löwe, A. Barcza, M. Katter, and O. Gutfleisch, *Exploring* $La(Fe,Si)_{13}$*-Based Magnetic Refrigerants towards Application*, Scr. Mater. **67**, 584 (2012).

[6] O. Gutfleisch, T. Gottschall, M. Fries, D. Benke, I. Radulov, K. P. Skokov, H. Wende, M. Gruner, M. Acet, P. Entel, and M. Farle, *Mastering Hysteresis in Magnetocaloric Materials*, Philos. Trans. R. Soc. A **374**, 20150308 (2016).

[7] H. Wada and Y. Tanabe, *Giant Magnetocaloric Effect of* $MnA_{s1-x}Sb_x$, Appl. Phys. Lett. **79**, 3302 (2001).

[8] T. Krenke, E. Duman, M. Acet, E. F. Wassermann, X. Moya, L. Mañosa, and A. Planes, *Inverse Magnetocaloric Effect in Ferromagnetic Ni–Mn–Sn Alloys*, Nat. Mater. **4**, 450 (2005).

[9] R. Kainuma, Y. Imano, W. Ito, Y. Sutou, H. Morito, S. Okamoto, O. Kitakami, K. Oikawa, A. Fujita, T. Kanomata, and K. Ishida, *Magnetic-Field-Induced Shape Recovery by Reverse Phase Transformation*, Nature **439**, 957 (2006).

[10] A. Ghosh and K. Mandal, *Effect of Fe Substitution on the Magnetic and Magnetocaloric Properties of Mn-Rich Mn-Ni-Fe-Sn off-Stoichiometric Heusler Alloys*, J. Appl. Phys. **117**, 093909 (2015).

[11] L. Huang, D. Y. Cong, L. Ma, Z. H. Nie, Z. L. Wang, H. L. Suo, Y. Ren, and Y. D. Wang, *Large Reversible Magnetocaloric Effect in a Ni-Co-Mn-In Magnetic Shape Memory Alloy*, Appl. Phys. Lett. **108**, 032405 (2016).

[12] J. Liu, T. Gottschall, K. P. Skokov, J. D. Moore, and O. Gutfleisch, *Giant Magnetocaloric Effect Driven by Structural Transitions*, Nat Mater **11**, 620 (2012).

[13] N. T. Trung, L. Zhang, L. Caron, K. H. J. Buschow, and E. Brück, *Giant Magnetocaloric Effects by Tailoring the Phase Transitions*, Appl. Phys. Lett. **96**, 172504 (2010).

[14] T. Samanta, I. Dubenko, A. Quetz, S. Temple, S. Stadler, and N. Ali, *Magnetostructural Phase Transitions and Magnetocaloric Effects in $MnNiGe_{1-x}Al_x$*, Appl. Phys. Lett. **100**, 052404 (2012).

[15] S. C. Ma, Y. X. Zheng, H. C. Xuan, L. J. Shen, Q. Q. Cao, D. H. Wang, Z. C. Zhong, and Y. W. Du, *Large Room temperature Magnetocaloric Effect with Negligible Magnetic Hysteresis Losses in $Mn_{1-x}V_xCoGe$ Alloys*, J. Magn. Magn. Mater. **324**, 135 (2012).

[16] E. Liu, W. Wang, L. Feng, W. Zhu, G. Li, J. Chen, H. Zhang, G. Wu, C. Jiang, H. Xu, and F. de Boer, *Stable Magnetostructural Coupling with Tunable Magnetoresponsive Effects in Hexagonal Ferromagnets*, Nat. Commun. **3**, 873 (2012).

[17] Y. Li, Z. Y. Wei, E. K. Liu, G. D. Liu, S. G. Wang, W. H. Wang, and G. H. Wu, *Structural Transitions, Magnetic Properties, and Electronic Structures of Co(Fe)-Doped MnNiSi Compounds*, J. Appl. Phys. **117**, 17C117 (2015).

[18] J.-H. Chen, A. Us Saleheen, S. K. Karna, D. P. Young, I. Dubenko, N. Ali, and S. Stadler, *Tuning Martensitic Transitions in $(MnNiSi)_{0.65}(Fe_2Ge)_{0.35}$ through Heat Treatment and Hydrostatic Pressure*, J. Appl. Phys. **124**, 203903 (2018).

[19] T. Samanta, D. L. Lepkowski, A. U. Saleheen, A. Shankar, J. Prestigiacomo, I. Dubenko, A. Quetz, I. W. H. Oswald, G. T. McCandless, J. Y. Chan, P. W. Adams, D. P. Young, N. Ali, and S. Stadler, *Hydrostatic Pressure-Induced Modifications of Structural Transitions Lead to Large Enhancements of Magnetocaloric Effects in MnNiSi-Based Systems*, Phys. Rev. B **91**, 020401(R) (2015).

[20] C. L. Zhang, H. F. Shi, E. J. Ye, Y. G. Nie, Z. D. Han, and D. H. Wang, *Magnetostructural Transition and Magnetocaloric Effect in MnCoGe–NiCoGe System*, J. Alloys Compd. **639**, 36 (2015).

[21] C. L. Zhang, H. F. Shi, E. J. Ye, Y. G. Nie, Z. D. Han, B. Qian, and D. H. Wang, *Magnetostructural Transition and Magnetocaloric Effect in MnNiSi-Fe_2Ge System*, Appl. Phys. Lett. **107**, 212403 (2015).

[22] S. Ghosh, P. Sen, and K. Mandal, *Magnetostructural Transition and Large Magnetocaloric Effect in* $(Mn_{0.6}Fe_{0.4})NiSi_{1-x}Al_x$ *(x = 0.06–0.08) Alloys*, J. Magn. Magn. Mater. **500**, 166345 (2020).

[23] W. Bazela, A. Szytuła, J. Todorović, Z. Tomkowicz, and A. Zięba, *Crystal and Magnetic Structure of NiMnGe*, Phys. Status Solidi **38**, 721 (1976).

[24] V. Johnson and C. G. Frederick, *Magnetic and Crystallographic Properties of Ternary Manganese Silicides with Ordered* Co_2P *Structure*, Phys. Status Solidi **20**, 331 (1973).

[25] G. A. Landrum, R. Hoffmann, J. Evers, and H. Boysen, *The TiNiSi Family of Compounds: Structure and Bonding*, Inorg. Chem. **37**, 5754 (1998).

[26] L. Caron, Z. Q. Ou, T. T. Nguyen, D. T. Cam Thanh, O. Tegus, and E. Brück, *On the Determination of the Magnetic Entropy Change in Materials with First-Order Transitions*, J. Magn. Magn. Mater. **321**, 3559 (2009).

[27] S. Y. Dan'kov, A. M. Tishin, V. K. Pecharsky, and K. A. Gschneidner, *Magnetic Phase Transitions and the Magnetothermal Properties of Gadolinium*, Phys. Rev. B **57**, 3478 (1998).

[28] O. Tegus, E. Brück, K. H. J. Buschow, and F. R. de Boer, *Transition-Metal-Based Magnetic Refrigerants for Room-Temperature Applications*, Nature **415**, 150 (2002).

[29] L. Huang, D. Y. Cong, H. L. Suo, and Y. D. Wang, *Giant Magnetic Refrigeration Capacity near Room Temperature in* $Ni_{40}Co_{10}Mn_{40}Sn_{10}$ *Multifunctional Alloy*, Appl. Phys. Lett. **104**, 132407 (2014).

[30] A. Ghosh, P. Sen, and K. Mandal, *Measurement Protocol Dependent Magnetocaloric Properties in a Si-Doped Mn-Rich Mn-Ni-Sn-Si off-Stoichiometric Heusler Alloy*, J. Appl. Phys. **119**, 183902 (2016).

[31] A. K. Nayak, K. G. Suresh, and A. K. Nigam, *Giant Inverse Magnetocaloric Effect near Room Temperature in Co Substituted NiMnSb Heusler Alloys*, J. Phys. D. Appl. Phys. **42**, 035009 (2009).

[32] X. Zhou, W. Li, H. P. Kunkel, and G. Williams, *A Criterion for Enhancing the Giant Magnetocaloric Effect: (Ni–Mn–Ga)—a Promising New System for Magnetic Refrigeration*, J. Phys. Condens. Matter **16**, L39 (2004).

[33] N. T. Trung, V. Biharie, L. Zhang, L. Caron, K. H. J. Buschow, and E. Brück, *From Single- to Double-First-Order Magnetic Phase Transition in Magnetocaloric $Mn_{1-x}Cr_xCoGe$ Compounds*, Appl. Phys. Lett. **96**, 162507 (2010).

Chapter 5

Effect of hydrostatic pressure on the magnetocaloric response of $Ni_{45.5}Co_2Mn_{37.5}Sn_{15}$ Heusler alloy

The present chapter describes the effect of hydrostatic pressure on the magnetic, structural phase transition, exchange bias, and magnetocaloric properties of Co doped $Ni_{45.5}Co_2Mn_{37.5}Sn_{15}$ Heusler alloy.

5.1 Preamble

During the last decade, the study on Co-doped Ni-Mn-based Heusler alloys has already attracted immense attention to the researchers due to its potential multifunctional properties such as magnetic shape memory effect (MSME) [1,2], the large magnetocaloric effect [1–10], magnetoresistance [11–13], EB effect [14–18], and so on. The Co doping in place of Ni site of NiMn- based Heusler alloys works as a ferromagnetic activator in the system and enhance the magnetic activities for even better possible applications in magnetic refrigeration and memory devices [13,19,20]. Till date, plenty of such works have been carried out on Co-doped Heusler alloys with Ga, Sn, In, or Sb as a post transition element in search of better magnetocaloric materials [1,3,13,15,19,21–24]. For instance; Han et al. reported the enhancement of MCE response in Mn-rich $Mn_2Ni_{1.64-x}Co_xSn_{0.36}$ alloys for optimal doping concentrations [3]. Other examples are such as the observation of giant MCE near room temperature in Co substituted Ni-Mn-Sb Heusler alloys [4], the role of Co and Fe doping in the MCE in Ni-Mn-Sn alloys [21] and so on.

Besides, having all the above-mentioned properties in Co-doped such alloys, a very few percentages of doping content is found to be effective in MCE [3,13,19]. To understand the fact, it is necessary to know about the structural properties of Heusler alloys [25]. Ni-Mn-based off-stoichiometric ferromagnetic Heusler alloys have cubic ($L2_1$) austenite structure which can undergo a first order magnetostructural transition (MST) to a lower symmetric and magnetically weak tetragonal martensite phase during cooling depending upon the materials' compositions [6,7]. Most of the magneto-coupled effects of these materials depend on the change in magnetization across the first order MST, which starts to decrease for highly Co-doped Heusler alloys. There is another important magnetocaloric parameter called the relative cooling power (RCP), which measures the approximate amount of heat that can be extracted during a complete refrigeration cycle [26,27]. RCP in Co-doped materials decreases due to an increase in magnetic hysteresis. Moreover, the observation of exchange bias (EB) in bulk polycrystalline Ni-Mn-Sb and Ni-Mn-Sn Heusler alloys made them promising in other ways [16–18,28].

There is another possibility to add the hydrostatic pressure (P) as a stimulus to modify the electronic structure of a material which may lead to a significant change in the magnetic properties. The pressure dependence of the Curie temperature (T_C) provides important information on the ferromagnetic system and is an object of intensive studies in experimental and theoretical fields [29–33]. From the earlier work of our group [13], we have investigated the structural, magnetic, magnetocaloric, and magneto-transport properties of Co-doped Ni-Co-Mn-Sn off-stoichiometric Heusler alloys under ambient pressure. We have observed that the magnetic entropy change (ΔS_M) increases with increasing the Co content (replacing Ni). However, due to the appearance of larger field induced hysteresis, the RCP decreases rapidly in higher doping concentrations.

In the present work, we have investigated the effect of pressure on the structural phase transition, magnetic and magnetocaloric properties of $Ni_{45.5}Co_2Mn_{37.5}Sn_{15}$ sample chosen from the previous work of our group [13]. The effect of magnetic field on MST is found to be opposite to that of hydrostatic pressure. At ambient pressure, the martensitic transition temperature (T_M) shifts toward lower temperature and it is found to decrease with a shift rate of 3.29 K/T. On the other hand, T_M increases rapidly towards higher temperatures with a shift rate of 31.9 K/GPa when the hydrostatic pressure is applied. The applied pressure does not affect the field induced metamagnetic transition (FIMMT) significantly. The sample exhibits a peak value of isothermal magnetic entropy change (ΔS_M) about 13.67 J kg^{-1} K^{-1} due to a magnetic field change of ΔH = 50 kOe and it is found to decrease with increasing the pressure. The coercivity of the sample at a given temperature merely changes, but the exchange bias effect is improved by applying hydrostatic pressure. RCP of the sample is found to reduce a little bit with the hydrostatic pressure for a constant magnetic field.

5.2 Experimental

Polycrystalline $Ni_{45.5}Co_2Mn_{37.5}Sn_{15}$ alloy is prepared by conventional arc-melting technique under 4N purity of argon atmosphere using high purity constituent elements.

The ingots are re-melted six times to ensure the compositional homogeneity. Extra 3% Mn was taken to compensate for the weight loss during melting. Each ingot is sealed in an evacuated quartz tube along with a tantalum foil for annealing. After 24 hours of heat treatment at 1173 K, the ampoules are quenched in ice water. The final compositions of samples are checked by energy dispersive analysis of X-ray (EDAX). X-ray diffraction (XRD) is carried out in Rigaku MiniFlex II using Cu-K_α radiation at room temperature to detect the crystallographic parent phase of the prepared samples. The magnetization measurements have been performed at various hydrostatic pressures in a 9 Tesla Physical Property Measurement System (PPMS-9T) -Vibrating Sample Magnetometer (VSM) (Quantum Design, USA) module equipped with the Cu-Be clamp-type pressure cell with a maximum pressure of 1 GPa [34]. The thermomagnetic data are recorded with VSM for both zero field cooled (ZFC) heating and field cooled (FC) cooling mode in the temperature range of 2 K to 320 K under the ambient and high pressures up to 0.9 GPa for $Ni_{45.5}Co_2Mn_{37.5}Sn_{15}$ alloy in presence of a constant magnetic field of 100 Oe and also under different magnetic fields (~ 10, 40, 70, 90 kOe) at a temperature interval of 2 K. The isothermal magnetizations (*M-H* curves) are measured up to 50 kOe field at ambient and in presence of hydrostatic pressure in different temperatures across the martensitic transition temperature (T_M) during both the cooling and warming modes. To identify exchange bias properties in the sample, field cooled *M-H* curves are measured at different temperatures between 10 K and 130 K.

5.3 Results and discussion

Figure 5.1 shows the XRD pattern for the $Ni_{45.5}Co_2Mn_{37.5}Sn_{15}$ sample measured at room temperature (RT ~300 K). The sample is to be in the cubic austenite phase. The estimated lattice parameter in the cubic phase is about 5.92 Å.

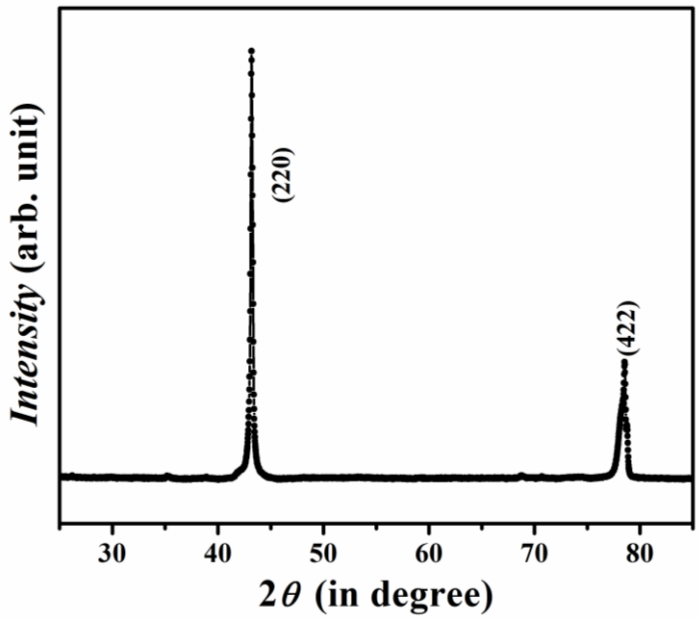

Figure 5.1: Room temperature XRD pattern for $Ni_{45.5}Co_2Mn_{37.5}Sn_{15}$ alloy

The temperature dependent magnetization (*M-T*) measurements are performed within the temperature range between 120 K and 320 K at different applied magnetic fields (100 Oe, 10 kOe, 40 kOe, 70 kOe, and 90 kOe) under ambient and 0.9 GPa pressure for $Ni_{45.5}Co_2Mn_{37.5}Sn_{15}$ which are shown in **Fig. 5.2**. The cooling (closed symbol) and warming (open symbol) curves are plotted in the same color for the same field *M-T* curves for the sake of clarity. A sudden drop in magnetization in cooling curves for various magnetic fields indicates the austenite to martensite transition. The exact values of characteristic transition temperatures (austenite start (A_s), austenite finish (A_f), martensite-austenite transition temperature, $T_A = (A_S+A_f)/2$, martensite start (M_s) and martensite finish (M_f), and austenite-martensite transition temperature, $T_M = (M_S+M_f)/2$) by varying different magnetic fields at constant ambient pressure are noted from the inflection point of the derivative of *M-T* curves and summarized in **Table 5.1**. At temperatures below M_f, the magnetization remains almost constant. Similarly, a sudden rise in the magnetization in the warming curve at different magnetic fields is an indication of the forward transition from martensite to austenite. The region between

martensite and austenite transition is represented as the thermal hysteresis (ΔT_{hys}) which confirms the first order nature of the transition.

With increasing the magnetic field, the first order transition shifts towards lower temperatures and exhibits field induced magnetostructural transition. The applied magnetic field prefers to stabilize the magnetically more sensitive phase, which is here the cubic austenite phase and as a result, T_M decreases with the increase in the magnetic field. To understand the effect of pressure and magnetic field on the first order MST, 0.9 GPa pressure is kept constant and the magnetic field then varied up to 90 kOe which is shown in **Fig. 5.2(b)** and these characteristic values are also tabulated in **Table 5.2**. It is found that T_M shifts to lower temperature as 3.29 K shifting for the field change of 10 kOe at ambient pressure which slightly decreases to 3.22 K under P = 0.9 GPa.

Further, the *M*-*T* curves are measured at selected values of hydrostatic pressures (0, 0.4, 0.7, and 0.9 GPa) in presence of a constant magnetic field (100 Oe) within the temperature range between 150 K and 300 K, which are shown in **Fig. 5.3**. It reveals that the effect of pressure retains the first order transition and it is similar to the effect of the magnetic field at ambient *P*. However, T_M shifts towards higher temperature with a shift rate of about $dT_M/dP \sim +31.9$ K/GPa. The applied hydrostatic pressure reduces the Mn-Mn separation which in turn favors antiferromagnetic coupling and stabilizes the martensite phase at higher temperatures. Therefore, we observe that magnetic and hydrostatic pressure provides an opposite effect on the martensitic transformation temperature. The effect of pressure on T_M and characteristic transformation temperatures are listed in **Table 5.3**. A similar effect has been observed in Ni-Mn-Ga compounds [34].

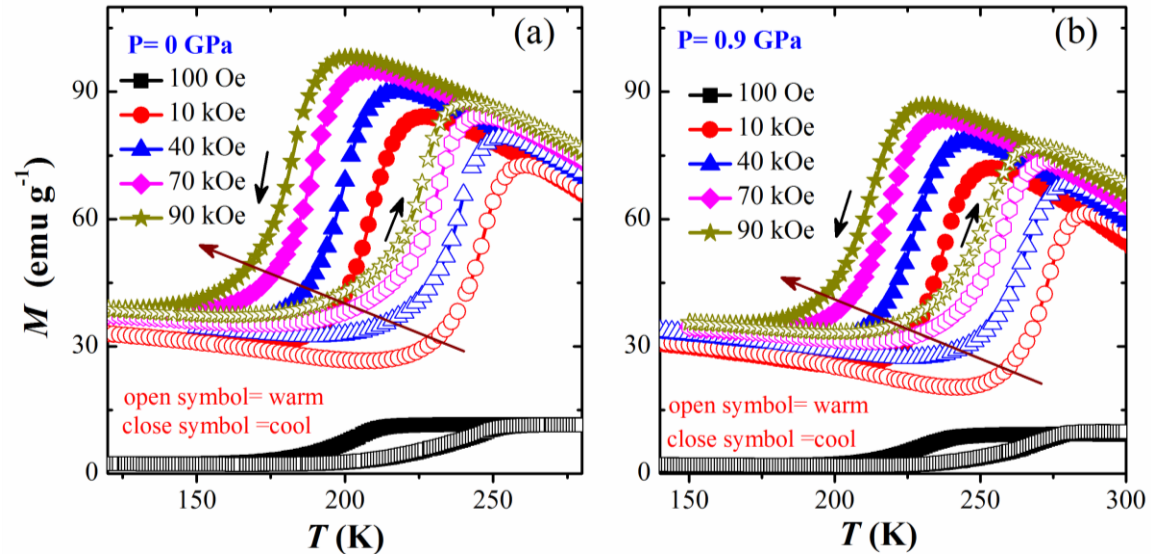

Figure 5.2: Temperature dependent magnetization (*M-T* curves) on warming and cooling at selected values of applied magnetic field under (a) ambient pressure and (b) P = 0.9 GPa of $Ni_{45.5}Co_2Mn_{37.5}Sn_{15}$ alloy (arrows indicate the warming and cooling paths).

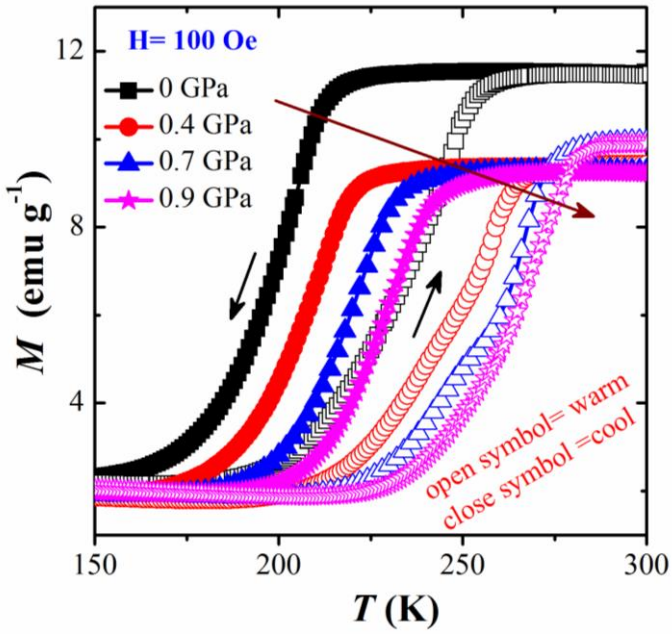

Figure 5.3: *M-T* curves on warming and cooling at different hydrostatic pressures (0, 0.4, 0.7, and 0.9 GPa) in presence of a constant magnetic field of 100 Oe.

Table 5.1: Characteristic transition temperatures of $Ni_{45.5}Co_2Mn_{37.5}Sn_{15}$ sample at ambient pressure in presence of different applied magnetic fields.

H	***P* = 0 Gpa**				***T_M* (K) =(M_s+M_f)/2**	***T_A* (K) =(A_s+A_f)/2**
	M_s (K)	M_f (K)	A_s (K)	A_f (K)		
100 Oe	215	180	209	254	198	232
10 kOe	219	196	232	255	208	244
40 kOe	211	187	225	248	199	237
70 kOe	200	176	217	241	188	229
90 kOe	195	168	212	236	182	224

Table 5.2: Characteristic transition temperatures of $Ni_{45.5}Co_2Mn_{37.5}Sn_{15}$ at 0.9 GPa pressure in presence of different applied magnetic fields.

H	***P* = 0.9 Gpa**				***T_M* (K) =(M_s+M_f)/2**	***T_A* (K) =(A_s+A_f)/2**
	M_s (K)	M_f (K)	A_s (K)	A_f (K)		
100 Oe	245	209	239	281	227	260
10 kOe	249	222	258	283	236	271
40 kOe	238	214	250	277	226	264
70 kOe	232	202	241	267	217	254
90 kOe	223	197	236	263	210	250

Table 5.3: Characteristic transition temperatures of $Ni_{45.5}Co_2Mn_{37.5}Sn_{15}$ sample under different applied pressures.

***P* (GPa)**	***H* = 100 Oe**				***T_M* (K) =(M_S+M_f)/2**	***T_A* (K) =(A_S+A_f)/2**
	M_S (K)	M_f (K)	A_S (K)	A_f (K)		
0	215	180	209	254	198	232
0.4	220	190	219	271	205	245
0.7	232	202	236	277	217	257
0.9	245	209	239	281	227	260

The *M-H* measurements are carried out for $Ni_{45.5}Co_2Mn_{37.5}Sn_{15}$ around its first order MST in the field range of 0 – 50 kOe at selected values of pressures (0, 0.7 GPa, 0.9 GPa), spanning 150 – 250 K and 190 – 300 K with 5 K intervals during cooling and warming respectively obeying discontinuous heating and cooling protocol [35], shown in **Fig. 5.4**. The field sweeping is performed as follows: 0 → 50 kOe → 0. The FIMMT is present only in the warming mode for all the applied pressure values in the temperature region from 190 K to 300 K as shown in **Fig. 5.4(d-f).** During cooling mode, no such FIMMT is observed for the applied magnetic field up to 50 kOe which clearly indicates that the first order transition takes place only in warming mode. The hydrostatic pressure merely affects the FIMMT, but significantly diminishes the saturation magnetization in the austenite and martensite phases as the applied pressure resists the moments from aligning along the direction of the magnetic field.

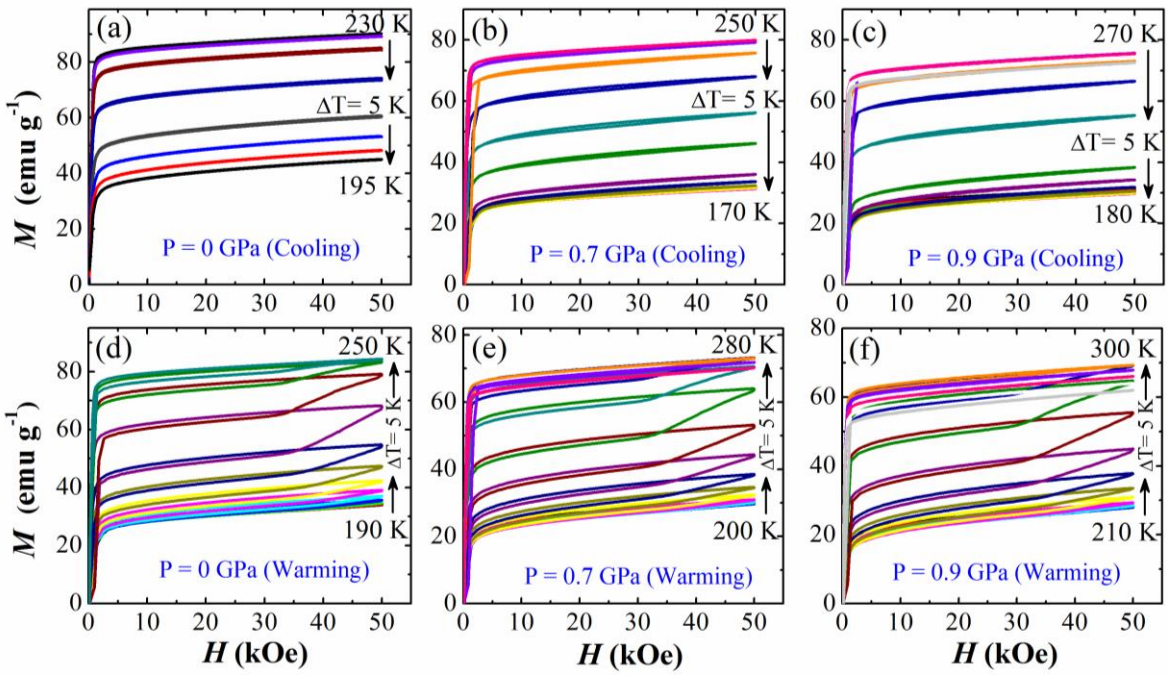

Figure 5.4: Field dependence of magnetization (*M-H* curves) of $Ni_{45.5}Co_2Mn_{37.5}Sn_{15}$ alloy at different temperatures across the martensitic transition for selected values of hydrostatic pressures (0, 0.7, and 0.9 GPa) during (a-c) cooling and during (d-f) warming mode.

Furthermore, to confirm the order of MST, Arrott plots (M^2 vs. H/M) are plotted for the alloy in warming mode under ambient pressure which is shown in **Fig. 5.5**. Based on Banerjee criteria, the slope of the Arrott plot across phase transition takes positive values for a second order transition whereas, for the first order phase transition, the slope of the Arrott plot would take negative values. During warming mode, such an S-shaped curve present across the transition temperature indicates that the alloy undergoes a first order MST. Therefore, warming mode should be followed for accurate measurement of magnetocaloric parameters for these studied materials.

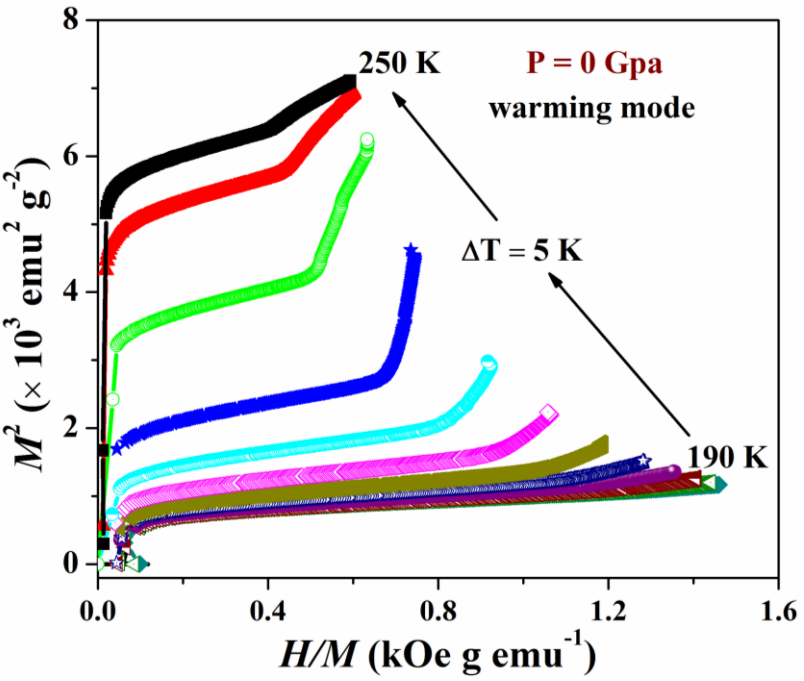

Figure 5.5: Arrott plot for $Ni_{45.5}Co_2Mn_{37.5}Sn_{15}$ alloy during warming mode under ambient pressure

To understand the exchange bias behavior in the studied sample, the field cooled hysteresis loops (full looped *M-H* curves) are measured at different temperatures between 10 K and 130 K under ambient and 0.9 GPa pressure which are shown in **Fig. 5.6.** The sample is first cooled to the targeted temperatures in presence of a high magnetic field from 300 K and then the field sweeping is done as follows: 30 kOe → 0→

−30 kOe → 0 → 30 kOe (for the sake of clarity, only the region between −7.5 kOe and +7.5 kOe is shown in the figure. The width of the hysteresis increases initially resulting in higher coercivity (H_C) as the temperature increases from 10 K to the EB blocking temperature (T_{EB} ~ 80 K) and then starts to decrease. T_{EB} is defined by the temperature above which the EB field almost vanishes in a material. As the temperature increases, the thermal energy diminishes the interfacial exchange interaction between the ferro and antiferro sites, which in turn results in a decrease in the EB field. Here we have observed the FC EB behavior at ambient as well as higher pressure. These results can be analyzed by calculating EB parameters like EB field (H_E). The values of H_E and H_C are calculated using $H_E = |(H_1 + H_2)|/2$ and $H_C = |(H_1 - H_2)|/2$ respectively, where H_1 denotes the field for zero magnetization during positive to reverse field sweeping and H_2 denotes the same during opposite field sweeping. These values are shown in **Fig. 5.6(k) and 5.6(l)** for ambient and high pressure measurements. Here, H_C remains almost independent of the hydrostatic pressure, whereas H_E shows a small decrease in magnitude with the increase in pressure at 10 K. H_E increases at 50 K and 80 K with applied high pressure. It can be observed that the curvature of the temperature dependent H_E curve switches from negative to positive as the pressure is applied. This signifies that the hydrostatic pressure stabilizes EB behavior. Here, the applied pressure compresses the unit cell of the sample, and the Mn-Mn inter-site separation decreases. This might leads to an enhancement in the AFM-FM interfacial coupling but also decrease the volume of the FM domains. The cumulative result comes out as the increase in H_E at 50 K and 80 K with applied high pressure whereas the same decreases at 10 K.

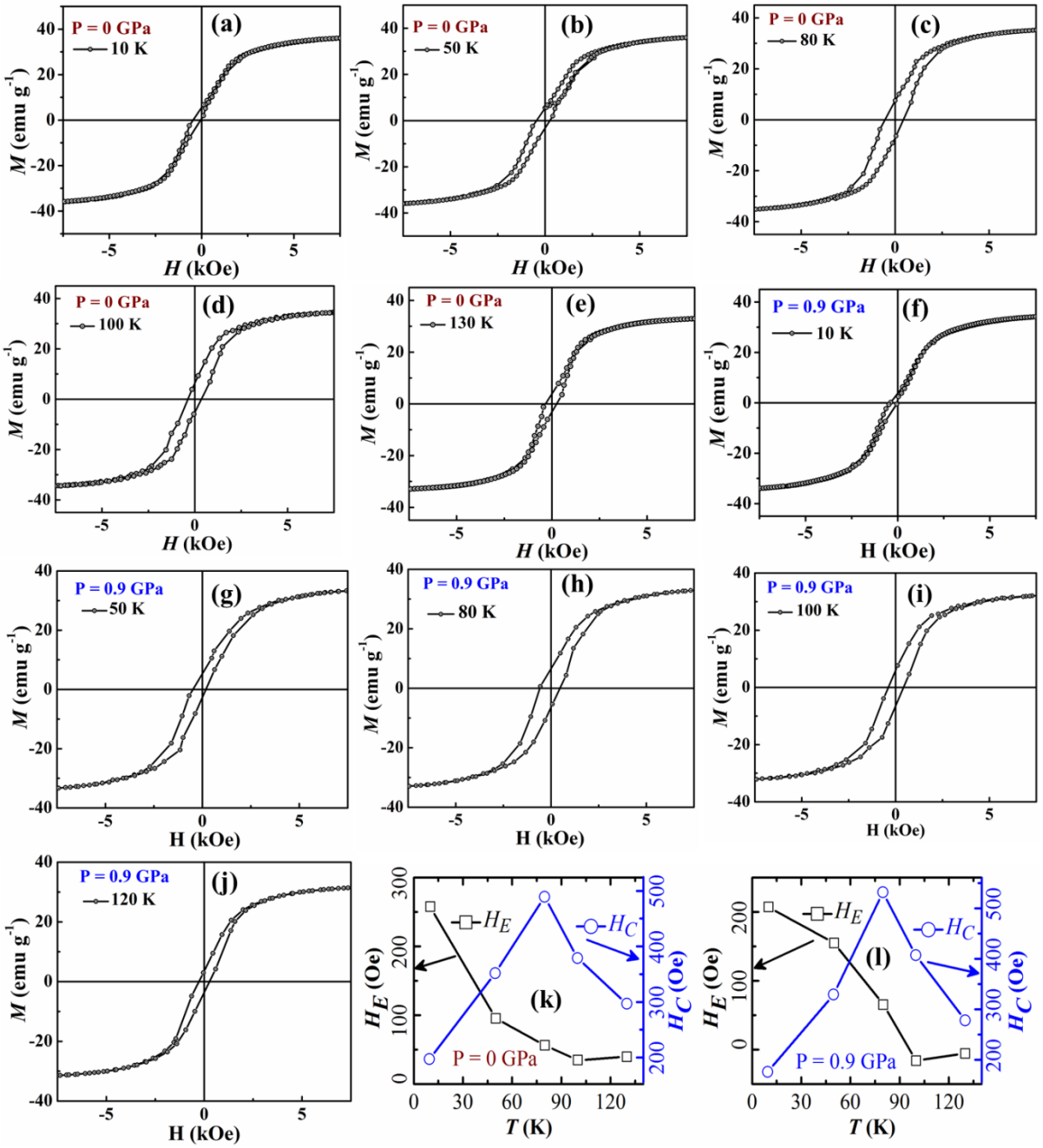

Figure 5.6: Field cooled (FC) magnetic hysteresis loops of $Ni_{45.5}Co_2Mn_{37.5}Sn_{15}$ alloy measured at different temperatures for (a) 10 K, (b) 50 K, (c) 80 K, (d) 100 K, and (e) 130 K under ambient pressure and for the same set of temperatures (f-j) under high pressure (P = 0.9 Gpa). Temperature dependent exchange bias field and coercivity of $Ni_{45.5}Co_2Mn_{37.5}Sn_{15}$ alloy at (k) ambient pressure and at (l) P = 0.9 GPa.

The MCE of $Ni_{45.5}Co_2Mn_{37.5}Sn_{15}$ alloy has been estimated by calculating the ΔS_M for various pressures from the isothermal M-H curves in warming using the Maxwell equation [6],

$$\Delta S_M(T, \Delta H) = \mu_0 \int_0^H \left(\frac{\partial M(H,T)}{\partial T}\right)_H dH \quad (5.1)$$

where, M, T, H, and μ_0 are respectively the magnetization of the sample, instantaneous temperature, applied magnetic field, and permeability of free space. ΔS_M is calculated using the above equation by numerical integration of the isothermal *M-H* curves, measure during warming. The Maxwell equation cannot be used to calculate ΔS_M for an ideal first order transition (FOT), being discontinuous. However, most of these similar alloys do not show ideal FOT, i.e. the changes in $\left(\frac{\partial M}{\partial T}\right)_H$ is finite and hence, ΔS_M can be evaluated using equation (5.1). ΔS_M is plotted as a function of temperature at selected values of the magnetic field in **Fig. 5.7(a)** during warming mode. The same parameter is also calculated for various magnetic fields at selected values of applied pressure during warming, which is shown in **Fig. 5.7(b)**. The results are also given in **Table 5.4**.

Table 5.4: Magnetic entropy changes (ΔS_M) of $Ni_{45.5}Co_2Mn_{37.5}Sn_{15}$ under different applied magnetic field and hydrostatic pressure.

Pressure applied (Gpa)	Peak value of ΔS_M (J kg^{-1} K^{-1}) for different field near T_M, during the warming cycle	
	ΔH = 10 kOe	ΔH = 50 kOe
0	3.11	13.4
0.7	2.0	10.2
0.9	2.78	11.0

Magnetic entropy change monotonically increases with the increase in ΔH due to the motion of magnetic domain walls, twin boundary motion, and the magnetic spin rotation. On the other hand, the peak values of ΔS_M for a particular ΔH decreases as the higher hydrostatic pressure is applied. As the pressure increases, it compresses the lattice stags and as a result, both the intra and inter-site Mn-Mn separation decreases.

This turns out to be a decrease in FM and an increase in AFM interaction in the system. In addition to that, the pressurized sample finds more crystalline anisotropy which suppresses the total magnetization of the sample and makes the first order MST less sharp (decrease in dM/dT). All these are cumulatively responsible for the decrease in ΔS_M.

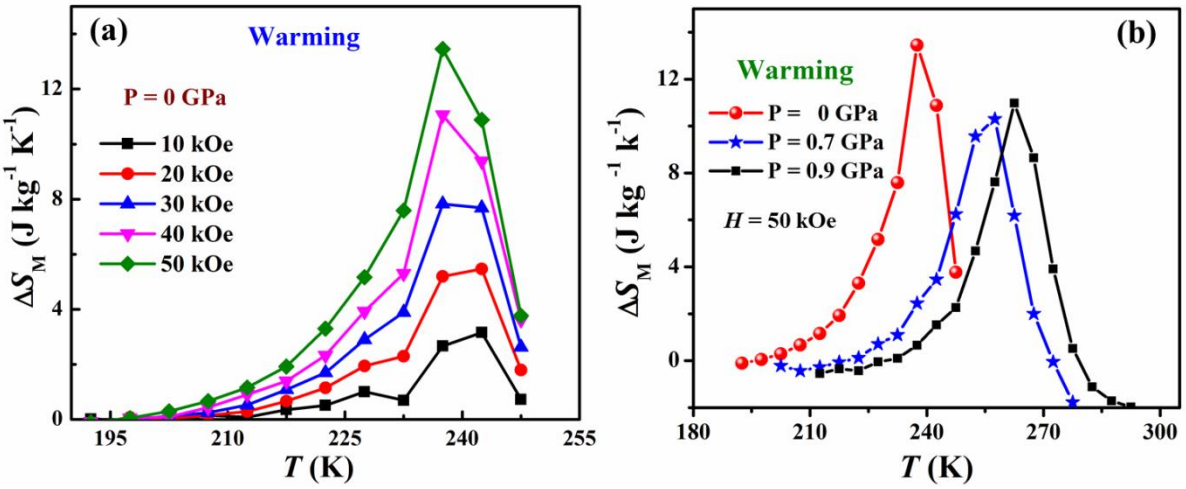

Figure 5.7: (a) Magnetic entropy change as a function of the temperature of $Ni_{45.5}Co_2Mn_{37.5}Sn_{15}$ alloy at ambient pressure under different magnetic fields applied during warming mode. (b) Temperature dependent magnetic entropy change of $Ni_{45.5}Co_2Mn_{37.5}Sn_{15}$ alloy at selected hydrostatic pressures (0, 0.7, and 0.9 GPa) associated with a field change from 0 to 50 kOe during warming.

Relative cooling power is one of the most important parameters to quantify MCE. The RCP is a measure of the amount of heat that can be transferred between the hot and cold sinks during one ideal refrigeration cycle and it is calculated from the temperature dependent ΔS_M curves using the following equation [27]

$$\mathrm{RCP} = |\Delta S_M^{peak}| \times \Delta T_{FWHM} \tag{5.2}$$

where, ΔS_M^{peak} is the peak value of ΔS_M of a ΔS_M-T curve plotted for a specific field change value and the ΔT_{FWHM} is the temperature window of the full width at half

maxima (FWHM) of the same $\Delta S_M - T$ curve. The field dependence of RCP for the sample at different pressures during warming is shown in **Fig. 5.8**. It is found that RCP increases almost linearly with the increase of fields for all pressure values. It is observed that the RCP during warming decreases with increasing pressure. The FIMMT and decrease in ΔS_M^{Max} reduce the RCP as the pressure is increased. These materials suffer from large hysteresis loss (HL) due to the presence of FIMMT. Therefore, it is necessary to subtract the average HL from RCP to obtain the net RCP of these materials. The average HL under 50 kOe due to the field induced hysteresis are found to be about 53.09, ~ 39.8, and ~ 40.93 J/kg respectively under ambient, 0.7 GPa, and 0.9 GPa pressure which in turn minimizes the net RCP during warming to its net value as 147.04, 146.6 and 130.14 J/kg.

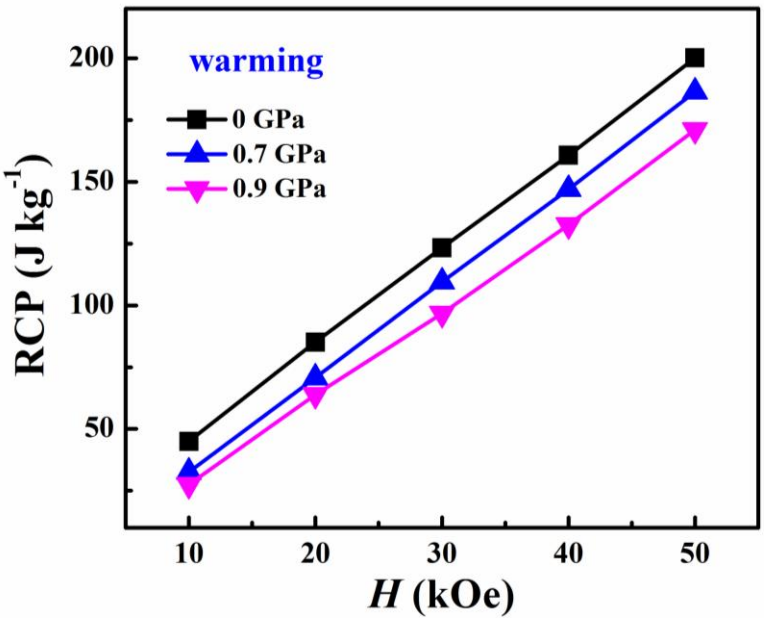

Figure 5.8: Field dependent relative cooling power of $Ni_{45.5}Co_2Mn_{37.5}Sn_{15}$ alloy at various hydrostatic pressures (0, 0.7, and 0.9 GPa) during warming.

5.4 Conclusion

In summary, we have observed that the hydrostatic pressure and magnetic field can drastically change the martensitic transformation temperatures in Ni-Co-Mn-Sn alloys. The first order magnetostructural transition of similar materials can be tuned by applying both the pressure and magnetic field as they influence the transition temperature oppositely. The exchange bias property of these materials can be enhanced by applying hydrostatic pressure. Although the magnetic entropy changes, as well as net relative cooling power, are found to reduce slightly with enhancing pressure, a fine control of operating temperature is possible by simultaneous application of magnetic field and hydrostatic pressure which is very advantageous in the context of the application of the similar type of materials as a potential magnetic refrigerant.

References

[1] K. Ito, W. Ito, R. Y. Umetsu, S. Tajima, H. Kawaura, R. Kainuma, and K. Ishida, *Metamagnetic Shape Memory Effect in Polycrystalline NiCoMnSn Alloy Fabricated by Spark Plasma Sintering*, Scr. Mater. **61**, 504 (2009).

[2] F. Chen, Y. X. Tong, B. Tian, L. Li, Y. F. Zheng, and Y. Liu, *Magnetic-Field-Induced Reverse Transformation in a NiCoMnSn High Temperature Ferromagnetic Shape Memory Alloy*, J. Magn. Magn. Mater. **347**, 72 (2013).

[3] Z. Han, J. Chen, B. Qian, P. Zhang, X. Jiang, D. Wang, and Y. Du, *Phase Diagram and Magnetocaloric Effect in $Mn_2Ni_{1.64-x}Co_xSn_{0.36}$ Alloys*, Scr. Mater. **66**, 121 (2012).

[4] A. K. Nayak, K. G. Suresh, and A. K. Nigam, *Giant Inverse Magnetocaloric Effect near Room Temperature in Co Substituted NiMnSb Heusler Alloys*, J. Phys. D. Appl. Phys. **42**, 35009 (2009).

[5] S. E. Muthu, N. V. R. Rao, M. M. Raja, D. M. R. Kumar, D. M. Radheep, and S. Arumugam, *Influence of Ni/Mn Concentration on the Structural, Magnetic and Magnetocaloric Properties in $Ni_{50-x}Mn_{37+x}Sn_{13}$ Heusler Alloys*, J. Phys. D. Appl. Phys. **43**, 425002 (2010).

[6] A. Planes, L. Mañosa, and M. Acet, *Magnetocaloric Effect and Its Relation to Shape-Memory Properties in Ferromagnetic Heusler Alloys.*, J. Phys. Condens. Matter **21**, 1 (2009).

[7] V. D. Buchelnikov and V. V Sokolovskiy, *Magnetocaloric Effect in Ni–Mn–X(X=Ga, In, Sn, Sb) Heusler Alloys*, Phys. Met. Metallogr. **112**, 633 (2011).

[8] M. Kohl, V. Chernenko, D. Bourgault, J. Tillier, P. Courtois, X. Chaud, N. Caillault, and L. Carbone, *3rd International Symposium on Shape Memory Materials for Smart Systems/E-MRS 2010 Spring Meeting Large Magneto-Caloric Effect in Ni–Co–Mn–In Systems at Room Temperature*, Phys. Procedia **10**, 120 (2010).

[9] T. Krenke, E. Duman, M. Acet, E. F. Wassermann, X. Moya, L. Manosa, and A. Planes, *Inverse Magnetocaloric Effect in Ferromagnetic Ni-Mn-Sn Alloys*, Nat. Mater. **4**, 450 (2005).

[10] J. Liu, T. Gottschall, K. P. Skokov, J. D. Moore, and O. Gutfleisch, *Giant Magnetocaloric Effect Driven by Structural Transitions*, Nat Mater **11**, 620 (2012).

[11] A. K. Nayak, K. G. Suresh, and A. K. Nigam, *Irreversibility of Field-Induced Magnetostructural Transition in NiCoMnSb Shape Memory Alloy Revealed by Magnetization, Transport and Heat Capacity Studies*, Appl. Phys. Lett. **96**, 2010 (2010).

[12] W. Ito, K. Ito, R. Y. Umetsu, R. Kainuma, K. Koyama, K. Watanabe, A. Fujita, K. Oikawa, K. Ishida, and T. Kanomata, *Kinetic Arrest of Martensitic Transformation in the NiCoMnIn Metamagnetic Shape Memory Alloy*, Appl. Phys. Lett. **92**, 1 (2008).

[13] A. Ghosh and K. Mandal, *Large Magnetoresistance Associated with Large Inverse Magnetocaloric Effect in Ni-Co-Mn-Sn Alloys*, Eur. Phys. J. B (2013).

[14] S. Esakki Muthu, N. V. Rama Rao, D. V. Sridhara Rao, M. Manivel Raja, U. Devarajan, and S. Arumugam, *Effect of Ni/Mn Concentration on Exchange Bias Properties in Bulk $Ni_{50-x}Mn_{37+x}Sn_{13}$ Heusler Alloys*, J. Appl. Phys. **110**, 023904 (2011).

[15] B. Wang and Y. Liu, *Exchange Bias and Inverse Magnetocaloric Effect in Co and Mn Co-Doped Ni_2MnGa Shape Memory Alloy*, Metals (Basel). **3**, 69 (2013).

[16] Z. Li, C. Jing, J. Chen, S. Yuan, S. Cao, and J. Zhang, *Observation of Exchange Bias in the Martensitic State of $Ni_{50}Mn_{36}Sn_{14}$ Heusler Alloy*, Appl. Phys. Lett. **91**, (2007).

[17] M. Khan, I. Dubenko, S. Stadler, and N. Ali, *Exchange Bias in Bulk Mn Rich Ni–Mn–Sn Heusler Alloys*, J. Appl. Phys. **102**, 113914 (2007).

[18] M. Khan, I. Dubenko, S. Stadler, and N. Ali, *Exchange Bias Behavior in Ni–Mn–Sb Heusler Alloys*, Appl. Phys. Lett. **91**, (2007).

[19] A. Ghosh and K. Mandal, *Large Inverse Magnetocaloric Effect in $Ni_{48.5-x}Co_xMn_{37}Sn_{14.5}$ (x = 0, 1 and 2) with Negligible Hysteresis*, J. Alloys Compd. **579**, 295 (2013).

[20] R. Y. Umetsu, A. Sheikh, W. Ito, B. Ouladdiaf, K. R. A. Ziebeck, T. Kanomata, and R. Kainuma, *The Effect of Co Substitution on the Magnetic Properties of the Heusler Alloy $Ni_{50}Mn_{33}Sn_{17}$*, Appl. Phys. Lett. **98**, (2011).

[21] T. Krenke, E. Duman, M. Acet, X. Moya, L. Mañosa, and A. Planes, *Effect of Co and Fe on the Inverse Magnetocaloric Properties of Ni-Mn-Sn*, J. Appl. Phys. **102**, 033903 (2007).

[22] R. Y. Umetsu, A. Sheikh, W. Ito, B. Ouladdiaf, K. R. A. Ziebeck, T. Kanomata, and R. Kainuma, *The Effect of Co Substitution on the Magnetic Properties of the Heusler Alloy $Ni_{50}Mn_{33}Sn_{17}$*, Appl. Phys. Lett. **98**, 10 (2011).

[23] M. Pan, B. You, Y. Zhao, S. Wang, M. Lu, A. Hu, H. Zhai, and S. Zhou, *The Effect of Interfacial Coupling in Co/CoO Exchange-Bias Bilayers with Special Field Cooling*, Phys. Lett. A **313**, 442 (2003).

[24] F. Chen, Y.-X. Tong, B. Tian, L. Li, and Y.-F. Zheng, *Martensitic Transformation and Magnetic Properties of Ti-Doped NiCoMnSn Shape Memory Alloy*, Rare Met. **33**, 511 (2014).

[25] M. Khan, I. Dubenko, S. Stadler, and N. Ali, *Magnetic and Structural Phase Transitions in Heusler Type Alloys $Ni_2MnGa_{1-x}In_x$*, J. Phys. Condens. Matter **16**, 5259 (2004).

[26] J.-H. Chen, N. M. Bruno, I. Karaman, Y. Huang, J. Li, and J. H. Ross, *Calorimetric and Magnetic Study for $Ni_{50}Mn_{36}In_{14}$ and Relative Cooling Power in Paramagnetic Inverse Magnetocaloric Systems*, J. Appl. Phys. **116**, (2014).

[27] P. Gorria, J. L. S. Llamazares, P. Álvarez, M. J. Pérez, J. S. Marcos, and J. A. Blanco, *Relative Cooling Power Enhancement in Magneto-Caloric Nanostructured Pr_2Fe_{17}*, J. Phys. D. Appl. Phys. **41**, 192003 (2008).

[28] J. Nogués and I. K. Schuller, *Exchange Bias*, J. Magn. Magn. Mater. **192**, 203 (1999).

[29] S. Morán, C. Ederer, and M. Fähnle, *Ab Initio Electron Theory for Magnetism in Fe: Pressure Dependence of Spin-Wave Energies, Exchange Parameters, and Curie Temperature*, Phys. Rev. B **67**, 12407 (2003).

[30] H. Yamada, K. Terao, K. Kondo, and T. Goto, *Strong Pressure Dependences of the Magnetization and Curie Temperature for CrTe and MnAs with NiAs-Type Structure*, J. Phys. Condens. Matter **14**, 11785 (2002).

[31] H. Yamada, K. Fukamichi, and T. Goto, *Itinerant-Electron Metamagnetism and Strong Pressure Dependence of the Curie Temperature*, Phys. Rev. B **65**, 24413 (2001).

[32] A. Kashyap, A. K. Solanki, T. Nautiyal, and S. Auluck, *Effect of Pressure on the Curie Temperature of Fe_3Pt*, Phys. Rev. B **52**, 13471 (1995).

[33] S. Wei, R. Duraj, R. Zach, M. Matsushita, A. Takahashi, H. Inoue, F. Ono, H. Maeta, A. Iwase, and S. Endo, *The Effect of Pressure on the Curie Temperature in Fe–Ni Invar Mechanical Alloys*, J. Phys. Condens. Matter **14**, 11081 (2002).

[34] U. Devarajan, S. Esakki Muthu, S. Arumugam, S. Singh, and S. R. Barman, *Investigation of the Influence of Hydrostatic Pressure on the Magnetic and Magnetocaloric Properties of $Ni_{2-x}Mn_{1+x}Ga$ (x = 0, 0.15) Heusler Alloys*, J. Appl. Phys. **114**, (2013).

[35] A. Ghosh, P. Sen, and K. Mandal, *Measurement Protocol Dependent Magnetocaloric Properties in a Si-Doped Mn-Rich Mn-Ni-Sn-Si off-Stoichiometric Heusler Alloy*, J. Appl. Phys. **119**, 183902 (2016).

Chapter 6 Magnetocaloric effect in Si doped Ni-Co-Mn-Sn Heusler alloys

This chapter describes the magnetic, exchange bias, and magnetocaloric properties of Si doped polycrystalline $Ni_{48}Co_{1.5}Mn_{35}Sn_{15.5-x}Si_x$ (x = 0, 1, 2, and 4) alloys, and the results indicate that Si doped in place of post transition element of these similar type of materials can be an effective way to reduce thermal as well as magnetic hysteresis across first order transition and thus, enhances the net relative cooling power of the material as a refrigerant.

6.1 Preamble

During the last decade, off-stoichiometric Ni-Mn-X (X = In, Sb, Sn) Heusler alloys are found to exhibit a large inverse magnetocaloric effect (MCE) across their first order magnetostructural transition (MST) [1–5]. Depending on the composition (Mn/X ratio), these alloys undergo MST from cubic austenite to tetragonal martensite phase [6] on reducing temperature. Along with the change in alloy composition, several external parameters like magnetic field, hydrostatic pressure may stabilize one phase by dominating over the other one [7,8]. Several strategies are introduced to increase MCE response either by varying Mn/X, Ni/Mn ratios, or by substituting the fourth element like Co or Fe in place of Ni/Mn [5,6,9–15]. Apart from MCE, these alloys also exhibit some interesting multifunctional properties such as magnetic shape memory effect [16,17], large magnetoresistance [18,19], exchange bias (EB) effect [20,21], and so on.

However, the Heusler alloys exhibiting first order MST possesses large field induced hysteresis which reduces the net relative cooling power (RCP) of that material. It has been observed that the addition of a small amount of Co replacing Ni in these alloys enhances the ΔS_M value but the appearance of field induced hysteresis across the first order MST reduces the net RCP of that material in higher doping concentrations [12]. Therefore to improve the inverse MCE of Heusler alloys, we have to reduce the hysteresis loss (HL) significantly to make their commercial use as refrigerant material. Recently, Si substitution in place of Sb is found to be effective to reduce the average HL which makes the net RCP higher [22]. Similar properties are also observed in Ge doped Ni–Mn–Sb alloys [23].

In the present study, we have investigated the magnetic, EB, and magnetocaloric properties of Si doped polycrystalline $Ni_{48}Co_{1.5}Mn_{35}Sn_{15.5-x}Si_x$ (x = 0, 1, 2, and 4) alloys due to a field change of 50 kOe. All these alloys are found to undergo a first order structural phase transition from martensite to austenite along with a second order ferromagnetic (FM) to paramagnetic (PM) transition. It is observed that martensitic transition temperature shifts to lower temperature with increasing Si substitution in

place of Sn whereas the Curie temperature (T_C) is insensitive to the doping amount. Isothermal magnetic entropy change (ΔS_M) and net RCP are measured across martensite to austenite transition and the corresponding values are found to be about 11.99, ~ 10.86, ~ 5.46, ~ 2.42 J kg^{-1} K^{-1} and ~ 136.1, ~ 130.1, ~ 141.8, ~ 63 J kg^{-1} for x = 0, 1, 2 and 4 alloys due to a field change of 50 kOe respectively. Interestingly, with increasing Si substitution in place of Sn, average magnetic HL reduces significantly from 49.7 J/kg (x = 0) to 8.6 J/kg (x = 4). However, the EB property of these alloys does not change significantly due to the doping amount.

6.2 Experimental

Polycrystalline Ni-rich $Ni_{48}Co_{1.5}Mn_{35}Sn_{15.5-x}Si_x$ (x = 0, 1, 2, and 4) alloys are prepared by conventional arc-melting technique under a 4N purity argon atmosphere using high purity constituents. The ingots are re-melted several times to ensure the compositional homogeneity. Extra 3% Mn is taken to compensate for the weight loss during melting. Each ingot is sealed in an evacuated quartz tube along with a tantalum foil for annealing. After 24 hours of heat treatment at 1173 K, the ampoules are quenched in ice water. The final compositions of samples are checked by energy dispersive analysis of X-ray (EDAX). X-ray diffraction (XRD) is carried out in Rigaku MiniFlex II using Cu-K_α radiation (wavelength, λ = 1.54 Å) at room temperature to detect the crystallographic parent phase of the prepared samples. All the magnetic measurements are performed in a Physical Property Measurement System (PPMS, Cryogenic Limited) up to 50 kOe magnetic field. The thermomagnetic data are taken under zero field cooled (ZFC), field cooled (FC) and field heating (FH) mode in the presence of 100 Oe field at an interval of 2 K. The isothermal curves are measured up to 50 kOe across their magnetostructural transition during heating mode.

6.3 Results and Discussion

Figure 6.1 shows the XRD patterns for all the investigated alloys at room temperature (~ 300 K). All the alloys are observed to be in the cubic austenite phase. The peak (220)

shifts toward a higher angle with increasing Si content which signifies that the lattice parameter decreases with increase in *x*. The obtained value of lattice parameters are 5.99 Å, 5.97 Å, 5.94 Å, and 5.92 Å for the alloys with *x* = 0, 1, 2, and 4 respectively.

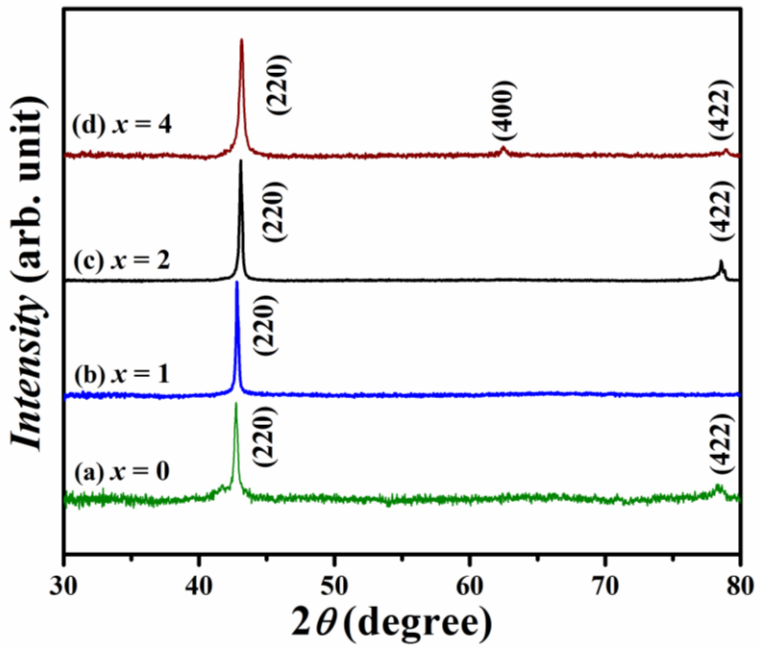

Figure 6.1: XRD patterns for $Ni_{48}Co_{1.5}Mn_{35}Sn_{15.5-x}Si_x$ (x =0, 1, 2, and 4) alloys at 300 K.

The temperature dependent magnetization (*M-T* curve) measurements of $Ni_{48}Co_{1.5}Mn_{35}Sn_{15.5-x}Si_x$ (x = 0, 1, 2, and 4) alloys are measured during ZFC, FC cooling, and FH mode in the presence of a constant 100 Oe magnetic field, within the temperature range of 5 K - 400 K and are shown in **Fig. 6.2**. The alloys exhibit a structural transition from low temperature martensite to high temperature austenite structure associated with a magnetic transition from FM to PM phase at T_C. The appearance of thermal hysteresis between heating and cooling confirms the transition is of the first order in nature. The characteristic transition temperatures: austenite start (A_S), austenite finish (A_f), martensite-austenite transition temperature [$T_A = (A_S+A_f)/2$], martensite start (M_S), martensite finish (M_f) and austenite-martensite transition temperature [$T_M = (M_S+M_f)/2$] are determined from the inflection point of *M-T* curves which are shown in **Fig. 6.3** and are also mentioned in **Table 6.1**. It can be seen that the

structural transition temperature shifts to the lower temperature with increasing Si substitution. The thermal hysteresis, defined by $\Delta T_{hys} = T_A - T_M$, is found to decrease with increasing x value. T_C values are calculated from the plot of dM/dT vs. T curve which are listed in **Table 6.1**. One can notice that T_C is insensitive to Si substitution.

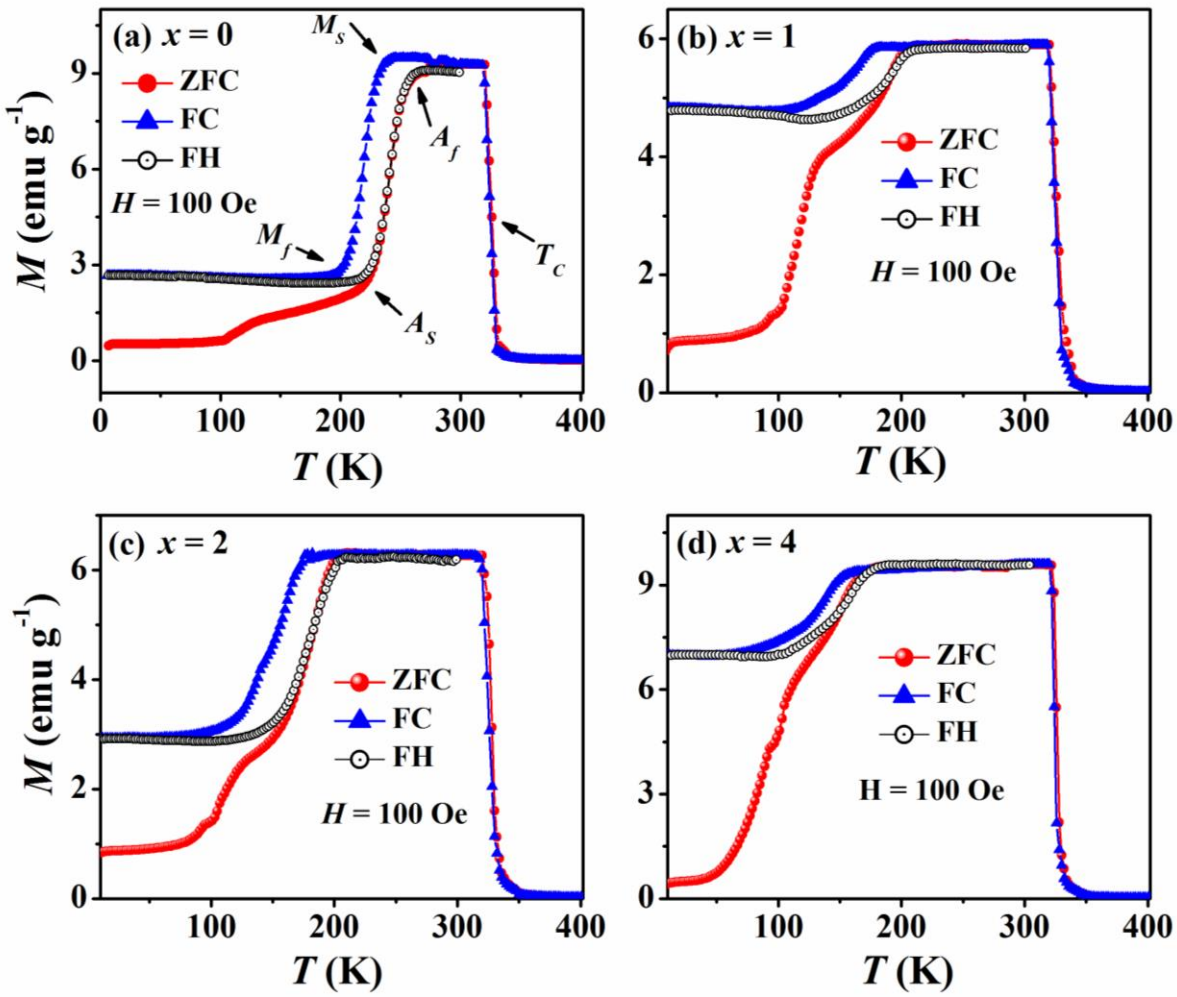

Figure 6.2: *M-T* curve during ZFC, FC and FH mode for (a) x = 0, (b) x = 1, (c) x = 2 and (d) x= 4 alloys in the presence of 100 Oe magnetic field.

It is well known that the decrease in valence electron concentration (e/a ratio) and as well as the increase in cell volume lowers the structural transition temperature in Heusler alloys. Here the substitution of Si with a lower atomic radius in place of Sn does not change the valence electron number but reduces the cell volume. Therefore, in

our case an opposite effect has been observed, i.e, a decrease in cell volume reduces T_M as the substitution of Si with lower atomic radius in place of Sn enhances the crystallographic disorder to the system [24]. A similar effect has been observed in other reported Si doped Heusler alloys [24,25].

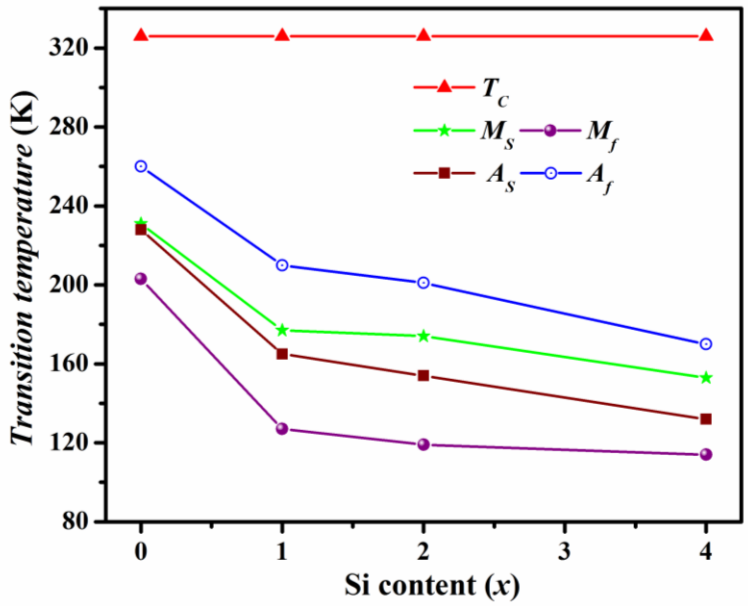

Figure 6.3: Variation of characteristic transition temperatures with Si content.

Table 6.1: Characteristic transition temperatures of $Ni_{48}Co_{1.5}Mn_{35}Sn_{15.5-x}Si_x$ (x = 1, 2, 4) alloys.

Sample	M_s (in K)	M_f (in K)	A_s (in K)	A_f (in K)	T_M (in K)	T_A (in K)	ΔT_{hys} (in K)	T_C (in K)
x =0	231	203	228	260	217	244	27	326
x = 1	177	127	165	210	152	188	36	326
x = 2	174	119	149	201	147	175	28	326
x = 4	153	114	132	170	134	152	18	326

To understand the exchange bias behavior of our samples, the FC hysteresis loops are carried out at low temperature (~ 5 K) for all the alloys (x = 0, 1, 2, and 4). To measure the hysteresis loop, the sample is first cooled at a targeted temperature from room temperature under the application of 50 kOe field, and then field sweeping is done as follows: 50 kOe → 0 → −50 kOe → 0 → 50 kOe. For the sake of clarity, only −5 kOe to +5 kOe regions are shown in **Fig. 6.4**. Noticeably, a finite shift of hysteresis loop is observed in the negative direction, which is the signature of the EB effect. The EB parameter, H_E can be calculated using the equation, $H_E = |(H_1+H_2)|/2$, where H_1 denotes the field for zero magnetization during positive to reverse field sweeping and H_2 denotes the same during opposite field sweeping. The obtained values are shown in **Fig. 6.4** with 161 Oe, 154 Oe, 152 Oe, and 141 Oe for the samples with x = 0, 1, 2, and 4 respectively. Here, with increasing Si substitution the AFM-FM interfacial coupling decreases and due to that a small decrease in H_E value is observed with increasing x.

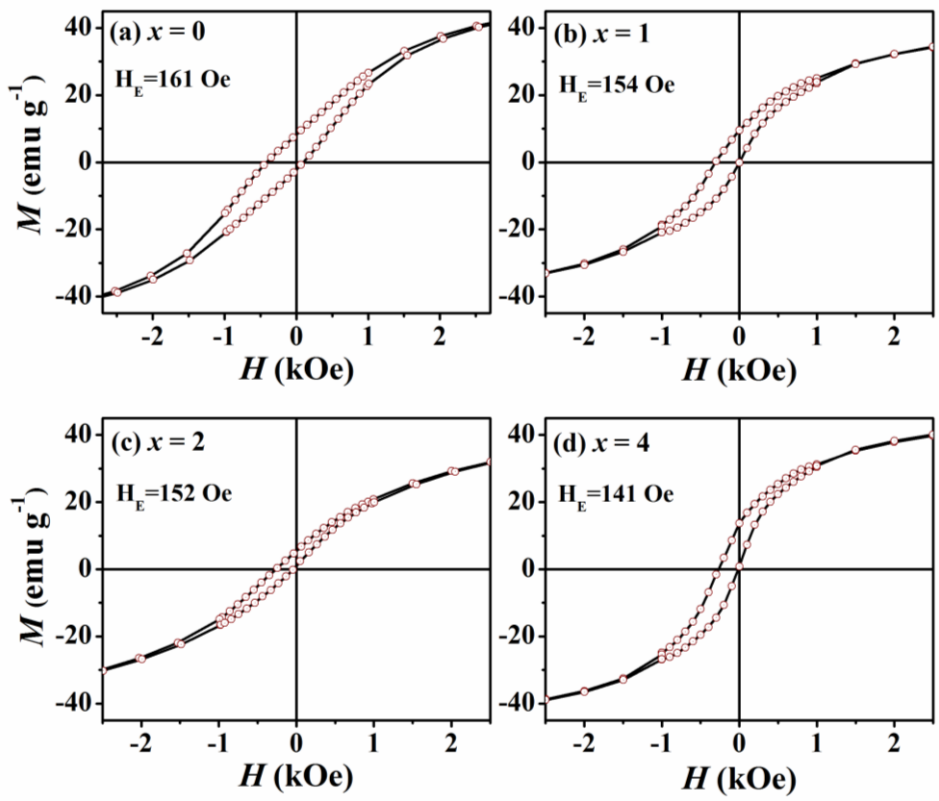

Figure 6.4: Field cooled (FC) hysteresis loop at 5 K for (a) x = 0, (b) x = 1, (c) x = 2 and (d) x = 4 alloys.

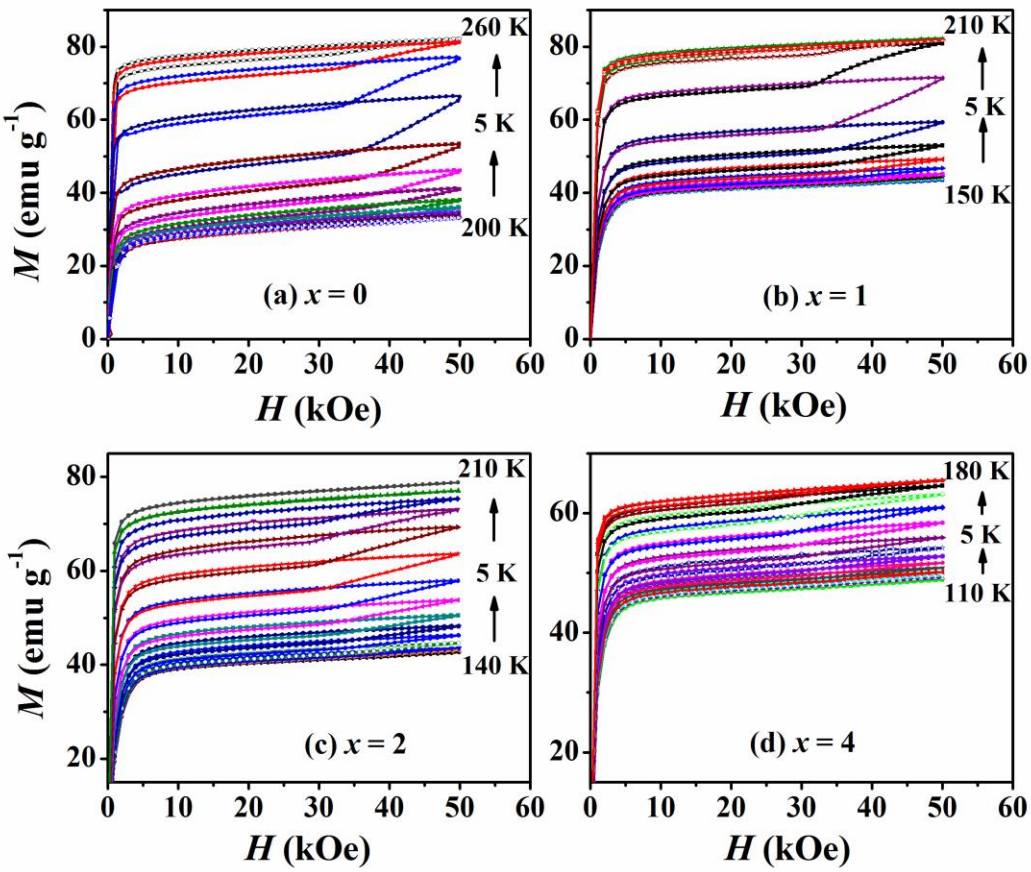

Figure 6.5: Field dependence of magnetization (*M-H* curve) at different temperatures across T_A for (a) x =0, (b) x = 1, (c) x = 2 and (d) x = 4 alloys.

Field dependent magnetization (*M-H*) measurements of $Ni_{48}Co_{1.5}Mn_{35}Sn_{15.5-x}Si_x$ (x = 0, 1, 2, and 4) alloys are performed at different temperatures across the martensite to austenite transition in the field range of 0 - 50 kOe at 5 K interval during heating which is shown in **Fig. 6.5**. To remove the field history effect of the sample, loop process methods are followed to measure the isothermal *M-H* curves [26]. In this method, the sample is cooled to a temperature (~ 80 K) well below of its M_f and then heated to a temperature near A_S for isothermal *M-H* measurement at that temperature. After that, the sample is again cooled to ~ 80 K and heated to a temperature, 5 K higher than the previous temperature for *M-H* measurement. This method has been followed for all the *M-H* measurements taken within the above-mentioned temperature region. All the samples show field induced metamagnetic transition (FIMMT) near T_A, where the

magnetization shows a sudden increase beyond a critical field (~ 32 kOe) which is consistent with the *M-T* curves and is the signature of a first order phase transition. Interestingly, the field induced hysteresis diminishes with increasing Si content. The saturation magnetization (M_S) is found to decrease in the austenite phase and an increase in the martensite phase with increasing *x*.

To confirm the order of phase transition, the Arrott plot (M^2 vs. H/M) has been plotted for all the samples which are shown in **Fig. 6.6**. Since the slope of the Arrott plot takes negative values in the vicinity of the phase transition temperature, the transition is of first order type according to Banerjee criteria.

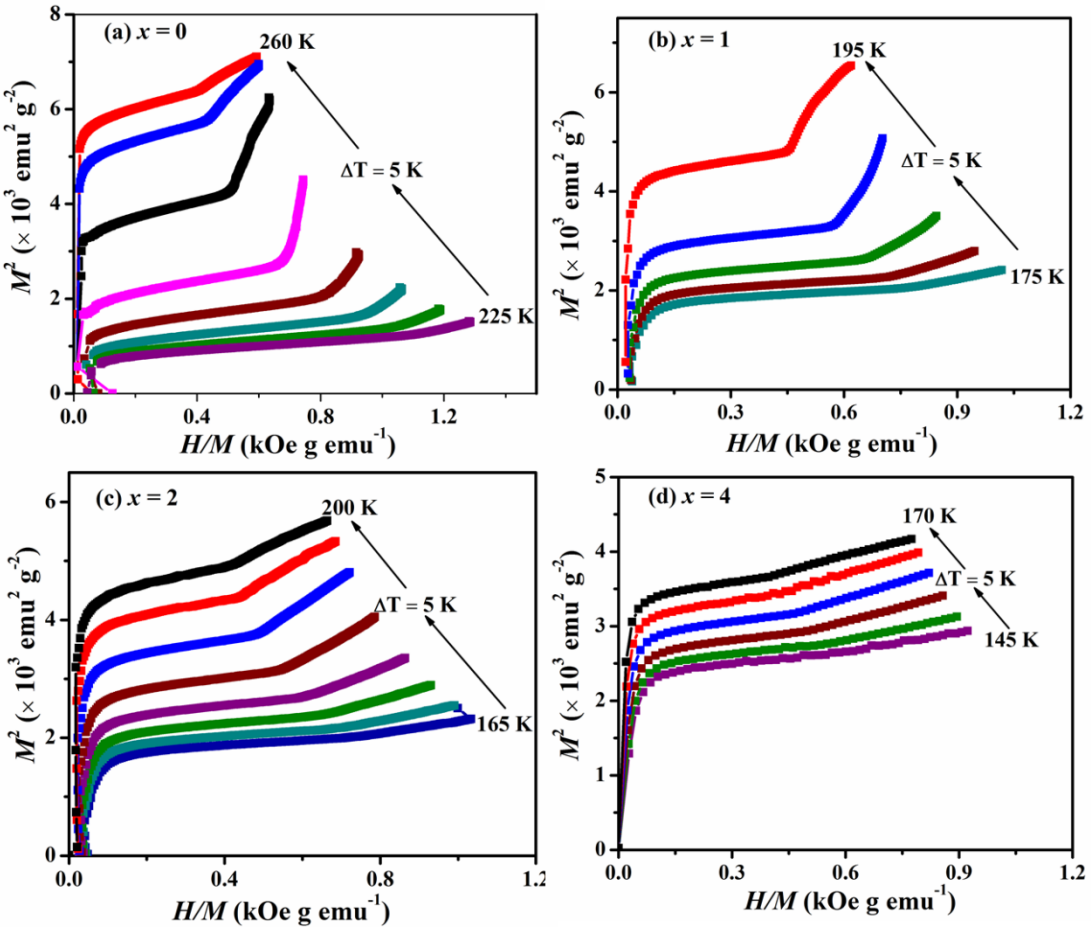

Figure 6.6: Arrott plot (M^2 vs. H/M) for the alloys with (a) *x* = 0, (b) *x* = 1, (c) *x* = 2 and (d) *x* = 4 alloy

Isothermal magnetic entropy change (ΔS_M), an important parameter in MCE studies, can be calculated using Maxwell equation [27],

$$\Delta S_M(T, \Delta H) = \mu_0 \int_0^H \left(\frac{\partial M(H,T)}{\partial T}\right)_H dH \quad (6.1)$$

where, M, T, and H are the magnetization of the sample, instantaneous temperature, and the applied magnetic field respectively. μ_0 is the permeability of free space. ΔS_M is calculated using equation (6.1) by numerical integration of the isothermal M-H curves. The relation cannot be used to calculate ΔS_M for an ideal first order transition (FOT), being discontinuous. However, most of these similar alloys do not show ideal FOT, i.e. the changes in $\left(\frac{\partial M}{\partial T}\right)_H$ is finite and therefore ΔS_M can be evaluated using equation (6.1). ΔS_M of all the alloys are plotted as a function of temperature for the different field changes in **Fig. 6.7**. The obtained values of the peak of ΔS_M are about 11.99, ~ 10.86, ~ 5.46, and ~ 2.42 J kg^{-1} K^{-1} for x = 0, 1, 2, and 4 respectively due to a field change of 50 kOe. It is found that with enhancing of Si substitution, ΔS_M decreases to a lower value due to being the less sharp of $\frac{\partial M}{\partial T}$ across martensitic transition with increasing x. The obtained ΔS_M values are comparable to other reported similar kinds of alloys, shown in **Table 6.2**.

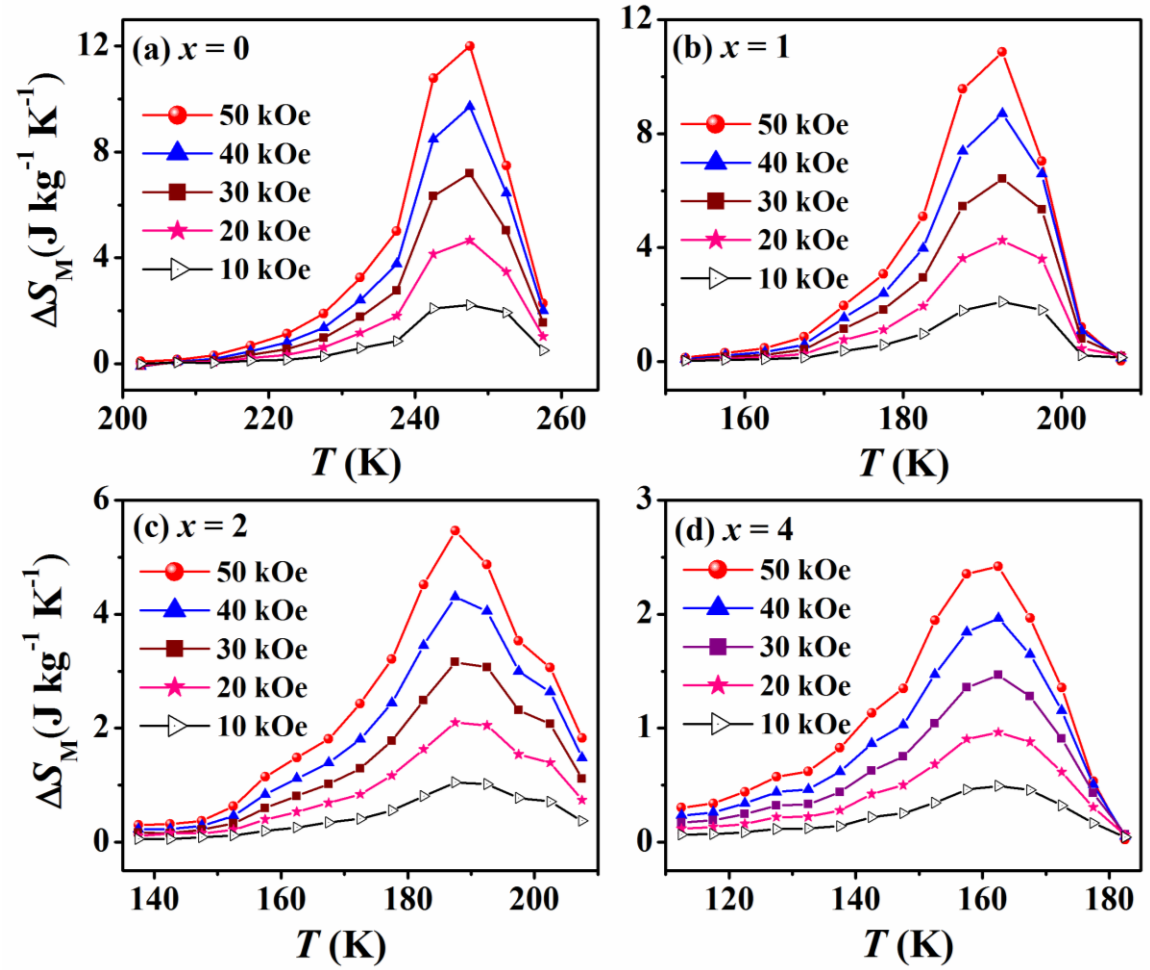

Figure 6.7: Magnetic entropy change as a function of temperature for of (a) $x = 0$, (b) $x = 1$, (c) $x = 2$ and (d) $x = 4$ alloy

Table 6.2: Peak value of magnetic entropy change (ΔS_M^{peak}), AHL and net RCP values of $Ni_{48}Co_{1.5}Mn_{35}Sn_{15.5-x}Si_x$ (x = 1, 2, 4) alloys due to field change of 50 kOe, on comparison with other alloys.

Sample Name	$\lvert\Delta S_M^{peak}\rvert$ (J kg^{-1} K^{-1})	Average HL (J/kg)	RCP/RC (J/kg)	Reference
Gd	10.2	-	410	[27]
$Gd_5Ge_2Si_2$	20	65	200	[28]
$Gd_5Ge_{1.9}Si_2Fe_{0.1}$	7	4	235	
$Fe_{51}Rh_{49}$	16.37	53	148	[29]
$Ni_{48}Co_{1.5}Mn_{35}Sn_{15.5-x}Si_x$				
x = 0	11.99	49.7	136.1	
x = 1	10.86	41.6	130.1	Present
x = 2	5.46	19.3	141.8	Work
x = 4	2.42	8.6	63	
$Ni_{45}Co_5Mn_{38}Sb_{11}Ge_1$	39	39	53	[23]
$Ni_{45}Co_5Mn_{38}Sb_9Ge_3$	28	23	54	
$Ni_{48.5}Co_{1.5}Mn_{37}Sn_{13}$	9.8	-	-	[30]
$Ni_{45.5}Co_2Mn_{37.5}Sn_{15}$	13.4	53.09	147.04	[8]
$Ni_{50}Mn_{34}In_{16}$	19	77.01	103.79	[2]
$Ni_{50}Mn_{36}Sn_{14}$	20	11	69	[31]
$Ni_{50}Mn_{37}Sb_{13}$	9.1	-	37.7	[1]

Relative Cooling Power, another key parameter in MCE studies that estimates the usefulness of the material as a refrigerant, can be calculated from the temperature dependence of the ΔS_M curve using the following equation,

$$\mathrm{RCP} = \Delta S_M^{peak} \times \Delta T_{FWHM} \tag{6.2}$$

where, ΔS_M^{peak} represents the peak value of ΔS_M of a $\Delta S_M - T$ curve plotted for a specific field change value and the ΔT_{FWHM} is the temperature window of the full width at half maxima of the same curve. The calculated RCP values for x = 0, 1, 2 and 4 are about

185.8, ~ 171.7, ~ 161.1, and ~ 71.6 J/kg respectively. Due to first order transition, the hysteresis loss should be subtracted from the RCP value to get the net RCP of these studied materials. The magnetic hysteresis losses of x = 0, 1, 2 and 4 alloys are obtained from their respective *M-H* curves and are plotted in **Fig. 6.8**. The average HL is computed by taking the average over the integral area under FWHM of **Fig. 6.8** and found to be about 49.7, ~ 41.6, ~ 19.3, and ~ 8.6 J/kg for x = 0, 1, 2, and 4 respectively under field change of 50 kOe which in turn reduces the RCP value to its net values 136.1 130.1, 141.8 and 63 J/kg. It is interesting to observe that due to Si substitution average HL drastically decreases to 8.6 J/kg for x = 4 which is very much lower than other reported values of the same family. A large net RCP is found for x = 2 alloy which is compared to other reported alloys, shown in **Table 6.2**.

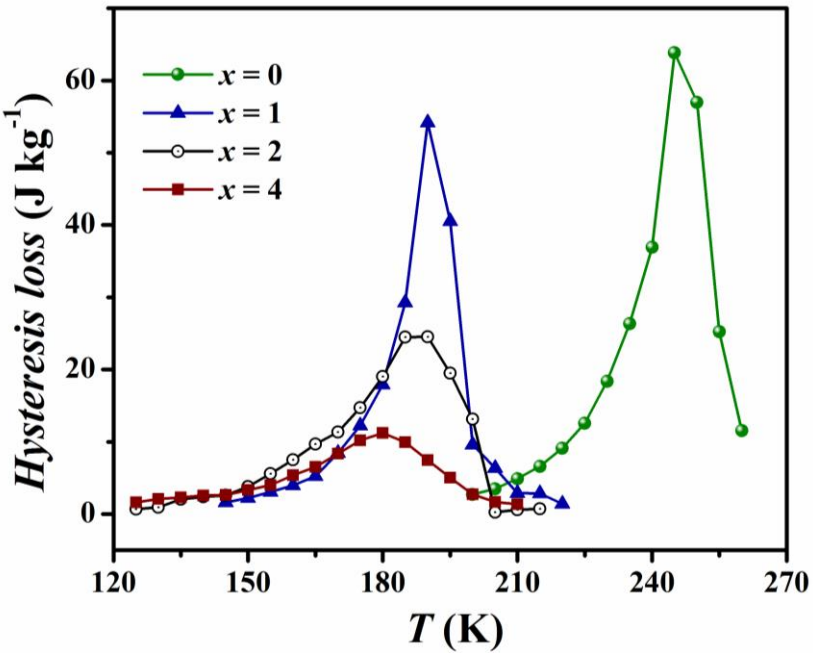

Figure 6.8: Average hysteresis loss (HL) for all the alloys across T_A due to the field change of 50 kOe.

6.4 Conclusion

In summary, the influence of Si doping in place of Sn on magnetic, exchange bias, and magnetocaloric properties of $Ni_{48}Co_{1.5}Mn_{35}Sn_{15.5-x}Si_x$ (x = 0, 1, 2, and 4) have been studied experimentally. The addition of Si in place of Sn reduces the martensitic transition to the lower temperature and broadens the operating temperature region. Magnetic entropy change across martensite to austenite transition also decreases to a lower value with Si content. Interestingly, the average hysteresis loss decreases drastically from 49.7 J/kg to 8.6 J/kg with increasing Si substitution from x = 0 to x = 4, which can enhance the effective relative cooling power. A maximum RCP of 141.8 J/kg has been observed for x = 2 alloy. Therefore a small amount of Si substituent can enhance the effective efficiency of these similar kinds of alloys which can make them good refrigerant material for practical application.

References

[1] J. Du, Q. Zheng, W. J. Ren, W. J. Feng, X. G. Liu, and Z. D. Zhang, *Magnetocaloric Effect and Magnetic-Field-Induced Shape Recovery Effect at Room Temperature in Ferromagnetic Heusler Alloy Ni-Mn-Sb*, J. Phys. D. Appl. Phys. **40**, 5523 (2007).

[2] V. K. Sharma, M. K. Chattopadhyay, and S. B. Roy, *Large Inverse Magnetocaloric Effect in $Ni_{50}Mn_{34}In_{16}$*, J. Phys. D. Appl. Phys. **40**, 1869 (2007).

[3] P. A. Bhobe, K. R. Priolkar, and A. K. Nigam, *Room Temperature Magnetocaloric Effect in Ni-Mn-In*, Appl. Phys. Lett. **91**, 89 (2007).

[4] T. L. Phan, P. Zhang, N. H. Dan, N. H. Yen, P. T. Thanh, T. D. Thanh, M. H. Phan, and S. C. Yu, *Coexistence of Conventional and Inverse Magnetocaloric Effects and Critical Behaviors in $Ni_{50}Mn_{50-x}Sn_x$ (x = 13 and 14) Alloy Ribbons*, Appl. Phys. Lett. **101**, (2012).

[5] N. H. Dan, N. H. Duc, N. H. Yen, P. T. Thanh, L. V Bau, N. M. An, D. T. K. Anh, N. A. Bang, N. T. Mai, P. K. Anh, T. D. Thanh, T. L. Phan, and S. C. Yu, *Magnetic Properties and Magnetocaloric Effect in Ni-Mn-Sn Alloys*, J. Magn. Magn. Mater. **374**, 372 (2015).

[6] T. Krenke, M. Acet, E. F. Wassermann, X. Moya, L. Mañosa, and A. Planes, *Ferromagnetism in the Austenitic and Martensitic States of Ni-Mn-In Alloys*, Phys. Rev. B **73**, 174413 (2006).

[7] L. Mañosa, D. González-Alonso, A. Planes, E. Bonnot, M. Barrio, J. L. Tamarit, S. Aksoy, and M. Acet, *Giant Solid-State Barocaloric Effect in the Ni-Mn-In Magnetic Shape-Memory Alloy*, Nat. Mater. **9**, 478 (2010).

[8] S. Arumugam, S. Ghosh, A. Ghosh, U. Devarajan, M. Kannan, L. Govindaraj, and K. Mandal, *Effect of Hydrostatic Pressure on the Magnetic, Exchange Bias and Magnetocaloric Properties of $Ni_{45.5}Co_2Mn_{37.5}Sn_{15}$*, J. Alloys Compd. **712**, 714 (2017).

[9] T. Krenke, E. Duman, M. Acet, X. Moya, L. Mañosa, and A. Planes, *Effect of Co and Fe on the Inverse Magnetocaloric Properties of Ni-Mn-Sn*, J. Appl. Phys. **102**, 1 (2007).

[10] R. Y. Umetsu, A. Sheikh, W. Ito, B. Ouladdiaf, K. R. A. Ziebeck, T. Kanomata, and R. Kainuma, *The Effect of Co Substitution on the Magnetic Properties of the Heusler Alloy $Ni_{50}Mn_{33}Sn_{17}$*, Appl. Phys. Lett. **98**, (2011).

[11] C. Jing, X. L. Wang, P. Liao, Z. Li, Y. J. Yang, B. J. Kang, D. M. Deng, S. X. Cao, J. C. Zhang, and J. Zhu, *Martensitic Phase Transition, Inverse Magnetocaloric Effect, and Magnetostrain in $Ni_{50}Mn_{37-x}Fe_xIn_{13}$ Heusler Alloys*, J. Appl. Phys. **114**, 063907 (2013).

[12] A. Ghosh and K. Mandal, *Large Magnetoresistance Associated with Large Inverse Magnetocaloric Effect in Ni-Co-Mn-Sn Alloys*, Eur. Phys. J. B **86**, (2013).

[13] A. K. Nayak, K. G. Suresh, and A. K. Nigam, *Giant Inverse Magnetocaloric Effect near Room Temperature in Co Substituted NiMnSb Heusler Alloys*, J. Phys. D. Appl. Phys. **42**, 035009 (2009).

[14] A. Ghosh and K. Mandal, *Large Inverse Magnetocaloric Effect in $Ni_{48.5-x}Co_xMn_{37}Sn_{14.5}$ (x = 0, 1 and 2) with Negligible Hysteresis*, J. Alloys Compd. **579**, 295 (2013).

[15] A. Ghosh and K. Mandal, *Effect of Fe Substitution on the Magnetic and Magnetocaloric Properties of Mn-Rich Mn-Ni-Fe-Sn off-Stoichiometric Heusler Alloys*, J. Appl. Phys. **117**, 093909 (2015).

[16] Z. H. Liu, M. Zhang, Y. T. Cui, Y. Q. Zhou, W. H. Wang, G. H. Wu, X. X. Zhang, and G. Xiao, *Martensitic Transformation and Shape Memory Effect in Ferromagnetic Heusler Alloy Ni2FeGa*, Appl. Phys. Lett. **82**, 424 (2003).

[17] R. Kainuma, Y. Imano, W. Ito, H. Morito, Y. Sutou, K. Oikawa, A. Fujita, K. Ishida, S. Okamoto, O. Kitakami, and T. Kanomata, *Metamagnetic Shape Memory Effect in a Heusler-Type $Ni_{43}Co_7Mn_{39}Sn_{11}$ Polycrystalline Alloy*, Appl. Phys. Lett. **88**, 192513 (2006).

[18] K. Inomata, S. Okamura, A. Miyazaki, M. Kikuchi, N. Tezuka, M. Wojcik, and E. Jedryka, *Structural and Magnetic Properties and Tunnel Magnetoresistance for $Co_2(Cr,Fe)Al$ and Co_2FeSi Full-Heusler Alloys*, J. Phys. D. Appl. Phys. **39**, 816 (2006).

[19] M. Oogane, Y. Sakuraba, J. Nakata, H. Kubota, Y. Ando, A. Sakuma, and T. Miyazaki, *Large Tunnel Magnetoresistance in Magnetic Tunnel Junctions Using Co_2MnX (X = Al, Si) Heusler Alloys*, J. Phys. D Appl. Phys. **39**, 834 (2006).

[20] M. Khan, I. Dubenko, S. Stadler, and N. Ali, *Exchange Bias in Bulk Mn Rich Ni-Mn-Sn Heusler Alloys*, J. Appl. Phys. **102**, (2007).

[21] R. Chapai and M. Khan, *Magnetism and Associated Exchange Bias in Ni_{2-}*

$_xCo_xMn_{1.4}Ga_{0.6}$, J. Magn. Magn. Mater. **403**, 97 (2016).

[22] R. Zhang, M. Qian, X. Zhang, F. Qin, L. Wei, D. Xing, X. Cui, J. Sun, L. Geng, and H. Peng, *Magnetocaloric Effect with Low Magnetic Hysteresis Loss in Ferromagnetic Ni-Mn-Sb-Si Alloys*, J. Magn. Magn. Mater. **428**, 464 (2017).

[23] R. Sahoo, A. K. Nayak, K. G. Suresh, and A. K. Nigam, *Structural, Magnetic, Magnetocaloric and Magnetotransport Properties in Ge Doped NiMnSb Heusler Alloys*, J. Magn. Magn. Mater. **324**, 1267 (2012).

[24] G. R. Raji, A. P. Paulose, R. B. Job, S. Thomas, K. G. Suresh, and M. R. Varma, *Phase Transformations, Inverse Magnetocaloric Effect and Critical Behavior of $Ni_{50}Mn_{36}Sn_{14-x}Si_x$ Heusler Alloys*, Intermetallics **82**, 59 (2017).

[25] S. Esakki Muthu, S. Singh, R. Thiyagarajan, G. Kalai Selvan, N. V Rama Rao, M. Manivel Raja, and S. Arumugam, *Influence of Si Substitution on the Structure, Magnetism, Exchange Bias and Negative Magnetoresistance in $Ni_{48}Mn_{39}Sn_{13}$ Heusler Alloys*, J. Phys. D. Appl. Phys. **46**, 205001 (2013).

[26] L. Caron, Z. Q. Ou, T. T. Nguyen, D. T. Cam Thanh, O. Tegus, and E. Brück, *On the Determination of the Magnetic Entropy Change in Materials with First-Order Transitions*, J. Magn. Magn. Mater. **321**, 3559 (2009).

[27] K. A. GschneidnerJr, V. K. Pecharsky, and A. O. Tsokol, *Recent Developments in Magnetocaloric Materials*, Reports Prog. Phys. **68**, 1479 (2005).

[28] V. Provenzano, A. J. Shapiro, and R. D. Shull, *Reduction of Hysteresis Losses in the Magnetic Refrigerant $Gd_5Ge_2Si_2$ by the Addition of Iron*, Nature **429**, 853 (2004).

[29] R. Barua, F. Jiménez-Villacorta, and L. H. Lewis, *Towards Tailoring the Magnetocaloric Response in FeRh-Based Ternary Compounds*, J. Appl. Phys. **115**, 17A903 (2014).

[30] X. Chen, V. B. Naik, R. Mahendiran, and R. V. Ramanujan, *Optimization of Ni-Co-Mn-Sn Heusler Alloy Composition for near Room Temperature Magnetic Cooling*, J. Alloys Compd. **618**, 187 (2015).

[31] T. L. Phan, P. Zhang, N. H. Dan, N. H. Yen, P. T. Thanh, T. D. Thanh, M. H. Phan, and S. C. Yu, *Coexistence of Conventional and Inverse Magnetocaloric Effects and Critical Behaviors in $Ni_{50}Mn_{50-x}Sn_x$ (x = 13 and 14) Alloy Ribbons*, Appl. Phys. Lett. **101**, 0 (2012).

Chapter 7 Reversible magnetocaloric effect and Critical behavior in Mn-Fe-Ni-Sn Heusler alloys

This chapter illustrates the magnetic, magnetocaloric properties, and critical behavior analysis across the second order ferromagnetic to the paramagnetic transition of $Mn_{48-x}Fe_xNi_{41}Sn_{11}$ (x = 8.5, 10.5) Heusler alloys.

7.1 Preamble

Ni-Mn-based Heusler alloys have been found to show a large inverse magnetocaloric effect (MCE) across their first order magnetostructural transition (MST) [1–4]. A small amount of Co or Fe substitution in the place of Ni/Mn enhances the magnetocaloric parameter, isothermal magnetic entropy change (ΔS_M) value, along with relative cooling power (RCP) of these materials [5–14]. Apart from this, they shows multifunctional properties like magnetic shape memory effect [15,16], large magnetoresistance [17,18], exchange bias (EB) effect [11,19]. Moreover, Heusler alloys are non-toxic and cheaper compared to the rare earth materials and thus can be used as a refrigerant for commercial applications.

Due to the presence of field induced hysteresis across the first order MST of Ni-Mn-based Heusler alloys, an excess energy is required to overcome the potential barrier between the two phases: austenite and martensite. This in turn makes the ΔS_M and adiabatic temperature change (ΔT_{ad}) irreversible. The presence of thermal hysteresis reduces the net RCP of that material. On the other hand, the ΔS_M and ΔT_{ad} of the materials associated with second order magnetic transition (SOMT) are fully reversible. The materials associated with SOMT shows a lower value of ΔS_M compared to that of the materials associated with first order phase transition (FOPT) but the observed RCP is higher in the materials with SOMT due to broad transition under high magnetic fields and the absence of thermal as well as magnetic hysteresis [20,21]. For example; T. L. Phan *et al* [22] studied the conventional and inverse MCE of Ni-Mn-Sn alloys and ribbons and they showed ΔS_M value associated first order MST is larger compared to the value associated with SOMT but the net RCP is smaller in the case of first order MST than that of SOMT. This is because of hysteresis loss in first order MST due to the presence of field induced transition. Similar effects are observed in Si doped Ni-Mn-Sn alloy [21], Ba doped Ni-Mn-In alloy [23] and in Cu doped Ni-Mn-Sn alloys [24]. Therefore to develop inverse MCE response of Heusler alloys, we have to reduce the thermal hysteresis significantly. Otherwise, we can improve the reversible MCE of these alloys across their second order transition to make their real use as refrigerant material.

In one of our previous work from our group, we have studied the magnetocaloric properties of Fe doped $Mn_{50-y}Fe_yNi_{39.5}Sn_{10.5}$ (y = 0, 1, 2, 3, 4, 5, and 6) alloys [13]. The substitution of Fe in place of Mn results in the shifting of martensitic transition temperature towards higher temperatures, whereas the Curie temperature (T_C) merely increases with doping amount and remains close to the room temperature. In the present chapter, we have studied the magnetic and magnetocaloric properties of $Mn_{48-x}Fe_xNi_{41}Sn_{11}$ (x = 8.5, 10.5) alloys by increasing the doping amount of Fe further in place of Mn. The temperature dependent magnetization curve (M–T curve) reveals that these alloys show only second order ferromagnetic (FM) to paramagnetic (PM) transition at their respective T_C and no structural transformation is observed. A large value of saturation magnetization (M_S) ~ 72.76 Am^2/kg is observed at 80 K for x = 8.5 alloy as the alloy becomes purely austenite for this composition. A reversible of ΔS_M about 1.02 J kg^{-1} K^{-1} with moderate RCP ~ 40.2 J/kg are obtained near room temperature (~305 K) for x = 8.5, across its T_C due to a magnetic field change of 14 kOe only. The critical exponents are calculated for both the samples and found to exhibit long range FM ordering in their austenite phase.

7.2 Experimental

Polycrystalline $Mn_{48-x}Fe_xNi_{41}Sn_{11}$ (x = 8.5, 10.5) alloys were prepared by arc-melting technique under a 4N purity Argon atmosphere using high purity constituent elements. The ingots were re-melted several times to ensure homogeneity. Extra 3% Mn was taken to compensate for the weight loss during melting. Each ingot was sealed in an evacuated quartz tube along with a tantalum foil for annealing. After 24 hours of heat treatment at 1173 K the ampoules were quenched in ice water. The final compositions of samples were verified by energy dispersive analysis of X-ray (EDAX) analysis. X-ray diffraction (XRD) was carried out in Rigaku MiniFlex II using Cu-K_α radiation to detect the crystallographic parent phase of the prepared samples. The magnetization measurements were performed using a Vibrating Sample Magnetometer (Lake Shore Cryotronics) in a 14 kOe magnetic field. The thermo-magnetic data were taken in both heating and cooling mode in the presence of 100 Oe field at an interval of 3 K. The

isothermal magnetization measurements are measured up to 14 kOe across magnetic FM to PM transition. Differential scanning calorimetry (DSC) heat flow measurements are performed in heating and cooling mode to detect the phase transition temperature of the sample with a ramp rate of 10 K/min.

7.3 Result & Discussions:

Room temperature (RT ~ 300 K) XRD patterns are plotted in **Fig. 7.1.** Both the samples are found to be in the cubic austenite phase at 300 K. temperature dependence of magnetization (M-T curves) of $Mn_{48-x}Fe_xNi_{41}Sn_{11}$ (x = 8.5, 10.5) alloys in both zero field cooled (ZFC) and field cooled (FC) mode in the presence of 100 Oe field within the temperature range of 80 K to 400 K, are shown in **Fig. 7.2(a)**. Both the samples undergo a FM to PM transition in the austenite phase at T_C ~ 305 K for x = 8.5 and at T_C ~318 K for x = 10.5 alloy. The M-T curves clearly show that there is no magnetostructural transition exists between 80 K and T_C of both the alloys. In the low external magnetic field (~ 100 Oe) a splitting between ZFC and FC below T_C indicates that some antiparallel moments exist in the sample.

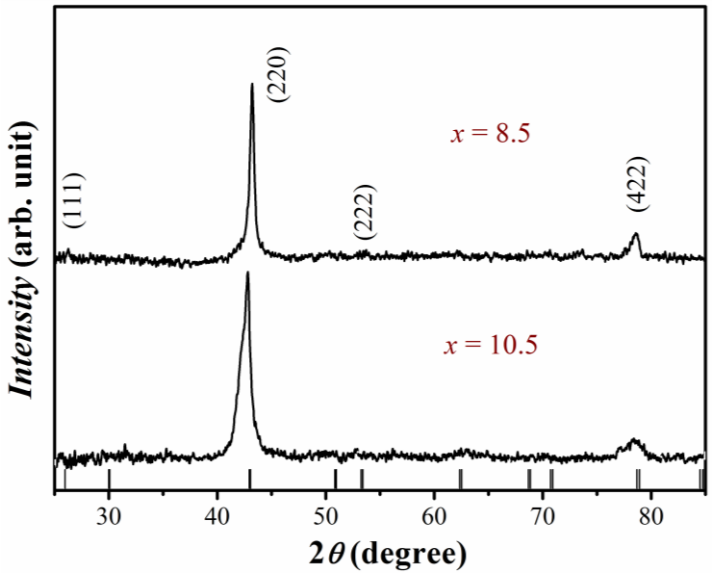

Figure 7.1: Room temperature XRD patterns of $Mn_{48-x}Fe_xNi_{41}Sn_{11}$ (x = 8.5, 10.5) alloys

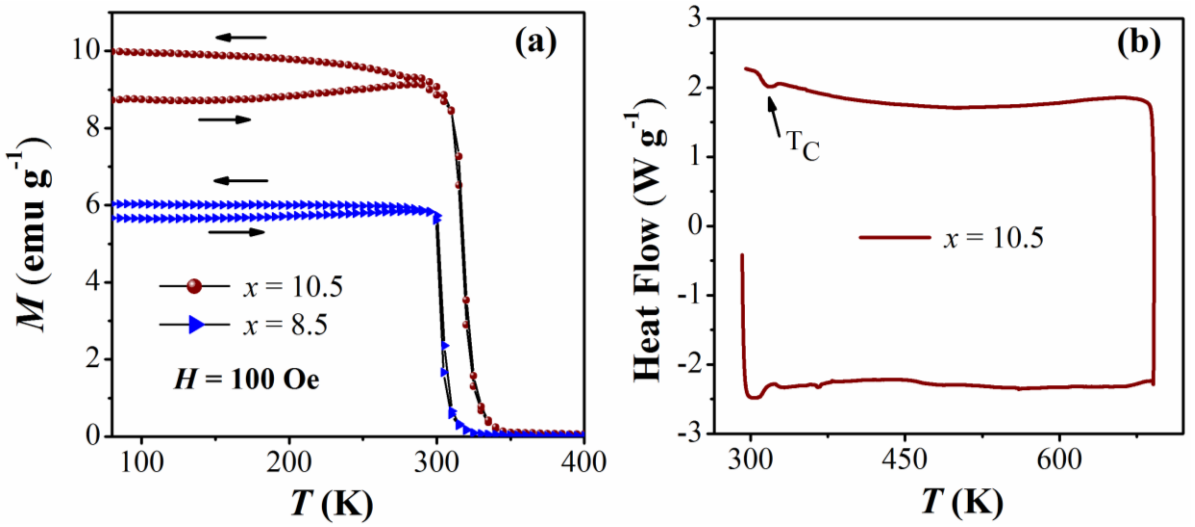

Figure 7.2: (a) Temperature dependent magnetization (M–T curves) for $Mn_{48-x}Fe_xNi_{41}Sn_{11}$ (x = 8.5, 10.5) alloys in the presence of 100 Oe field. (Arrows indicate the warming and cooling path). (b) DSC heat flow vs temperature curve for x = 10.5 alloy.

Differential scanning calorimetry (DSC) curve for x = 10.5 alloy has been performed upon both heating and cooling with a ramp rate of 10 K/min to check whether any first order transition is present at elevated temperatures as shown in **Fig. 7.2(b)**. The inflection point present during both cooling and heating at ~ 318 K corresponds to the curie temperature of the sample and is optimal for MCE applications. However, any first order transition has not been found at high temperature range between 300 K and 700 K.

To understand the magnetic behavior of these samples, we have measured ZFC hysteresis loops at 80 K under ± 14 kOe field for both alloys as shown in **Fig. 7.3**. A large saturation magnetization (M_S) about 72.76 emu/g is obtained for the alloy with x = 8.5 and M_S decreases to 63.8 emu/g for x = 10.5. As Mn atoms carry most of the magnetic moment in the Ni-Mn-based Heusler alloys, the decrease in Mn concentration reduces the total magnetic moment in the austenite phase and as a result, M_S decreases with increasing x value. As well as with increasing Fe content, Mn-Fe antiferromagnetic interaction enhances which in turn reduces the M_S value.

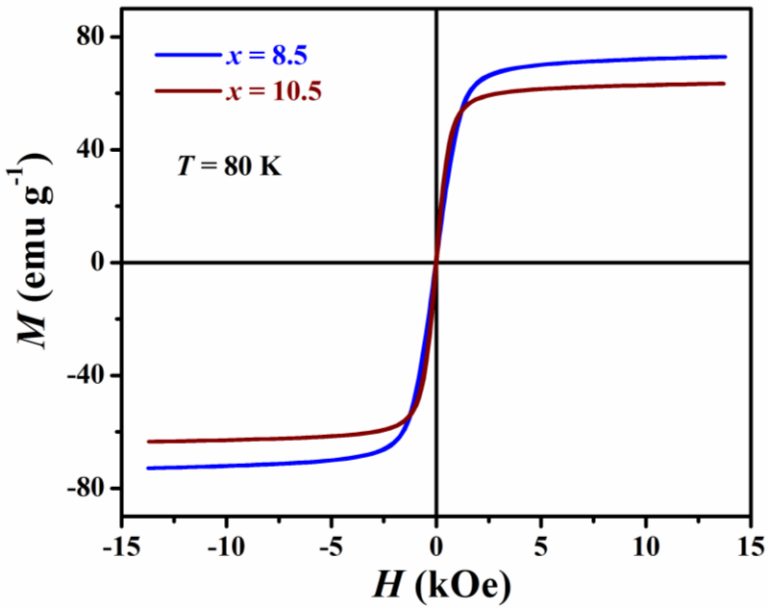

Figure 7.3: Magnetic hysteresis loop (M–H curve) of x = 8.5 and x = 10.5 alloys under 14 kOe field at 80 K.

The isothermal magnetization curves (M–H) for both the alloys are carried out across their magnetic phase transition in the field range of 0–14 kOe, spanning temperature from 277 K –325 K for x = 8.5 alloy at 3 K interval and 306 K–336 K for x = 10.5 alloy at 2 K interval during warming, shown in **Fig. 7.4(a) & 7.4(b)**. Clearly, there is no field induced hysteresis in the isothermal M–H curves which is a signature of typical second order transition.

It is well known that MCE is strongly correlated to the order of magnetic phase transition. Therefore to confirm the second order transition, Arrott plots ($M^{1/\beta}$ *vs.* $(H/M)^{1/\gamma}$ curve, β = 0.5, γ = 1.0) are plotted in **Fig. 7.5**. According to Banerjee criteria, the slope of Arrott plot would be positive for a second order transition whereas for the first order transition the slopes would take negative values [25]. Therefore, the positive slope of the Arrott plot indicates the second order nature of the phase transition.

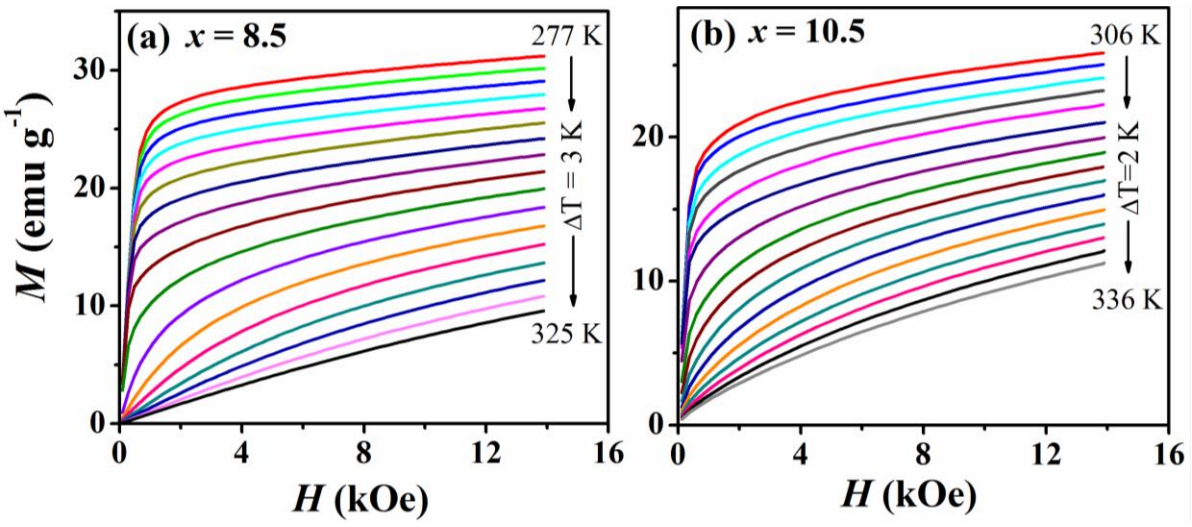

Figure 7.4: Field dependence of magnetization (M–H curves) for the alloy with (a) x = 8.5 and for (b) x = 10.5 at different temperatures across T_C under application of 14 kOe magnetic field.

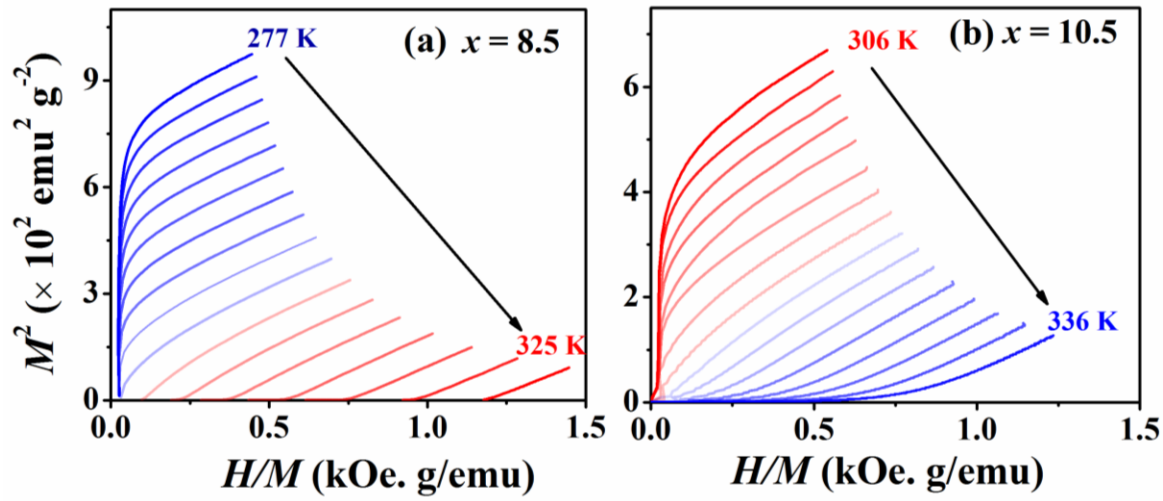

Figure 7.5: Arrott plot from field dependence of magnetization curve for (a) x = 8.5 and for (b) x = 10.5 alloy

The magnetic entropy change is a key parameter in the study of the magnetocaloric effect of Heusler alloys. ΔS_M of these alloys can be calculated from isothermal curves using Maxwell equation [26],

$$\Delta S_M(T, \Delta H) = \int_0^H \left(\frac{\partial M(H,T)}{\partial T}\right)_H dH \qquad (7.1)$$

where, M, T, and H are respectively the magnetization of the sample, instantaneous temperature, and applied magnetic field. ΔS_M is calculated using the above equation by numerical integration of the isothermal M–H curves. Since the alloys show second order phase transition, we can comfortably use the Maxwell equation to calculate the magnetic entropy change. ΔS_M as a function of temperature are plotted in **Fig. 7.6** for both the alloys. These curves are broad and ΔS_M reaches to a maximum value of about −1.02 J kg^{-1} K^{-1} for x = 8.5 alloy and of ~ −1.0 J kg^{-1} K^{-1} for x = 10.5 alloy under a field change of 14 kOe only. As expected, ΔS_M increases monotonically with the applied field changes till the peak of ΔS_M occurs across T_C. This is due to the twin boundary motion and motion of the spin walls. The obtained values of ΔS_M are compared with other alloys in **Table 7.1.**

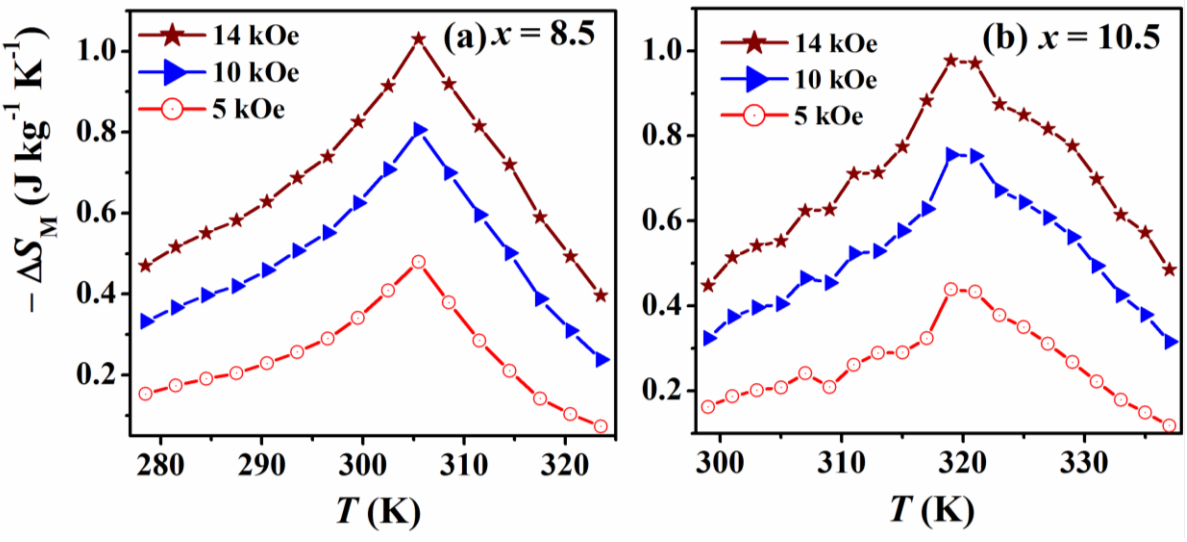

Figure 7.6: Magnetic entropy change as a function of temperature (ΔS_M -T curve) of (a) x = 8.5 alloy and of (b) x = 10.5 alloy under different magnetic field applied during warming cycle.

Table 7.1: Comparison of peak value of Magnetic entropy change ($|\Delta S_M^{peak}|$) and Relative cooling power (RCP) of $Mn_{48-x}Fe_xNi_{41}Sn_{11}$ (x = 8.5, 10.5) alloys with other alloys.

Sample Name	Field change (kOe)	$\|\Delta S_M^{peak}\|$ (J kg^{-1} K^{-1})	RCP (J/kg)	Reference
Gd	50	10.2	410	[26]
$Gd_5Ge_2Si_2$	50	20	200	[27]
$Ni_{50}Mn_{36}Sn_{14-x}Si_x$				[21]
x = 1	50	3.4$^{\#}$ / 2.8*	45$^{\#}$ / 80*	
x = 2	50	2.5$^{\#}$ / 2.7*	40$^{\#}$ / 100*	
x = 3	50	1.3$^{\#}$ / 2.3*	12$^{\#}$ / 65*	
$Ni_{45.5}Co_2Mn_{37.5}Sn_{15}$$^{\#}$	50	13.4	147.04	[28]
$Ni_{47}Mn_{40}Sn_{13}$	20	4.3$^{\#}$ / 2.3*	22.2$^{\#}$ / 57*	[29]
$Mn_{50}Ni_{40}Sn_{10}$$^{\#}$	50	8.6	39.8	[30]
$Ni_{50}Mn_{34}In_{16}$$^{\#}$	50	19	103.79	[31]
$Mn_{48-x}Fe_xNi_{41}Sn_{11}$				Present
x = 8.5	14	1.02	40.2	Work
x = 10.5	14	1.00	36.7	

$^{\#}$ ΔS_M calculated across first order MST; * ΔS_M calculated across SOMT.

To understand the ferromagnetic interaction of second order transition we have studied the critical behavior for these alloys. The critical behavior around T_C can be expressed by a set of critical exponents β, γ, and δ which are associated with the spontaneous magnetization (M_{sp}), initial magnetic susceptibility (χ_0) and critical isotherm magnetization at $T = T_C$ respectively [32]. The critical exponents can be calculated from the magnetic measurements by the following equations:

$$M_{sp}(T) = M_0|\epsilon|^{\beta} \qquad \epsilon < 0, T < T_C \tag{7.2}$$

$$\chi_0^{-1}(T) = \frac{h_0}{M_0}\epsilon^{\gamma} \qquad \epsilon > 0, T > T_C \tag{7.3}$$

$$M = DH^{\frac{1}{\delta}} \qquad \epsilon = 0, T = T_C \tag{7.4}$$

where 'ϵ' is the reduced temperature, defined as, $\epsilon = \frac{T-T_C}{T_C}$. '$M_0$', '$h_0$' and '$D$' are the critical amplitudes. We have used here the mean-field model for long range order (β = 0.5, γ = 1.0) to calculate the critical exponent β and γ values experimentally using the above equation. The value of β describes how the order moment grows below T_C. The value of γ describes the divergence of susceptibility above T_C and δ defines the curvature of *M(H)* at $T = T_C$. These three critical exponents are related to each other by Widom scaling relation as,

$$\delta = 1 + \frac{\gamma}{\beta} \tag{7.5}$$

From **Fig. 7.5**, by linearly fitting the high field isotherms we have determined the $M_{sp}(T)$ and $\chi_0^{-1}(T)$ values. The intercepts with the axis M^2 for $T < T_C$ give the M_{sp} values and the intercepts with the axis $\left(\frac{H}{M}\right)$ give χ_0^{-1} values which are plotted as a function of temperature in **Fig. 7.7**. The β and γ values are calculated by fitting the equation (7.2) and (7.3) using the M_{sp} and χ_0^{-1} values. The optimal values are β = 0.43, γ = 1.09, T_C = 307 K for the alloy with x = 0.85 and β = 0.40, γ = 1.02, T_C = 319.8 K for the alloy with x =10.5.

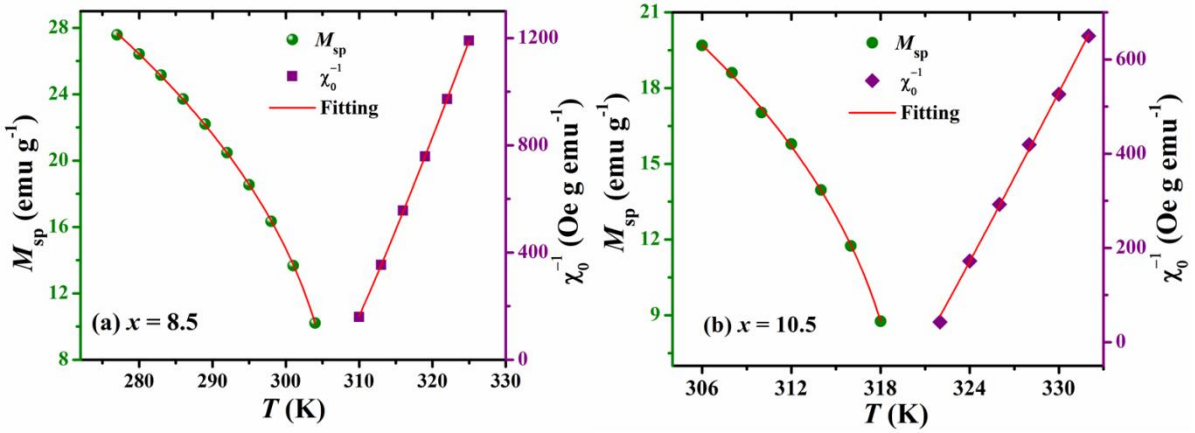

Figure 7.7: M_{sp} and $\boldsymbol{\chi_0^{-1}}$ values as a function of temperature along with the fits (solid lines) following equations (7.2) and (7.3), which give the values of the exponents and T_C as (a) β = 0.43, γ = 1.09, T_C = 307 K for the alloy with x = 0.85 and (b) β = 0.40, γ = 1.02, T_C = 319.8 K for the alloy with x =10.5.

The values of critical exponents along with T_C can also be calculated using Kouvel-Fisher technique [33]. According to this method, the critical exponents can be estimated from the following equation,

$$M_{sp}\left(\frac{dM_{sp}}{dT}\right)^{-1} = \frac{T-T_C}{\beta} \tag{7.6}$$

$$\chi_0^{-1}\left(\frac{d\chi_0^{-1}}{dT}\right)^{-1} = \frac{T-T_C}{\gamma} \tag{7.7}$$

From the above equation, $M_{sp}\left(\frac{dM_{sp}}{dT}\right)^{-1}$ vs. T and, $\chi_0^{-1}\left(\frac{d\chi_0^{-1}}{dT}\right)^{-1}$ vs. T should be straight lines with slope $1/\beta$ and $1/\gamma$ respectively and their intercept with the T-axis provide the T_C values. The linear fit of these plots, shown in **Fig. 7.8**, yield the value of critical exponents as, β = 0.42, γ = 1.08, T_C = 306.7 K for the alloy with x = 0.85 and β = 0.40, γ = 0.99, T_C = 319.9 K for the alloy with x =10.5.

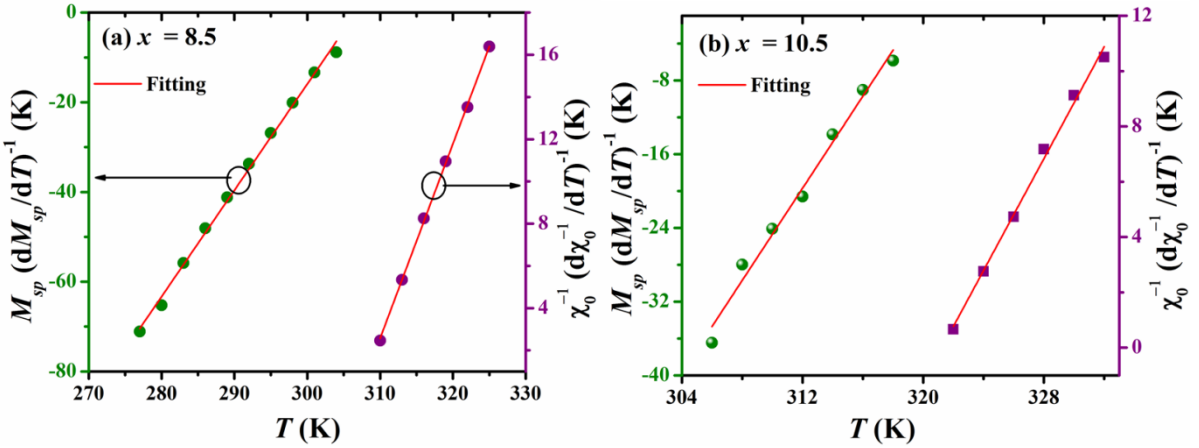

Figure 7.8: Kouvel-Fisher plot of M_{sp} and $\boldsymbol{\chi_0^{-1}}$ values for (a) x = 8.5 and (b) x = 10.5 alloy. The linear fits (solid lines) of the data yield the values of the exponents and T_C as β = 0.42, γ = 1.08, T_C = 306.7 K for the alloy with x = 0.85 and β = 0.40, γ = 0.99, T_C = 319.9 K for the alloy with x =10.5.

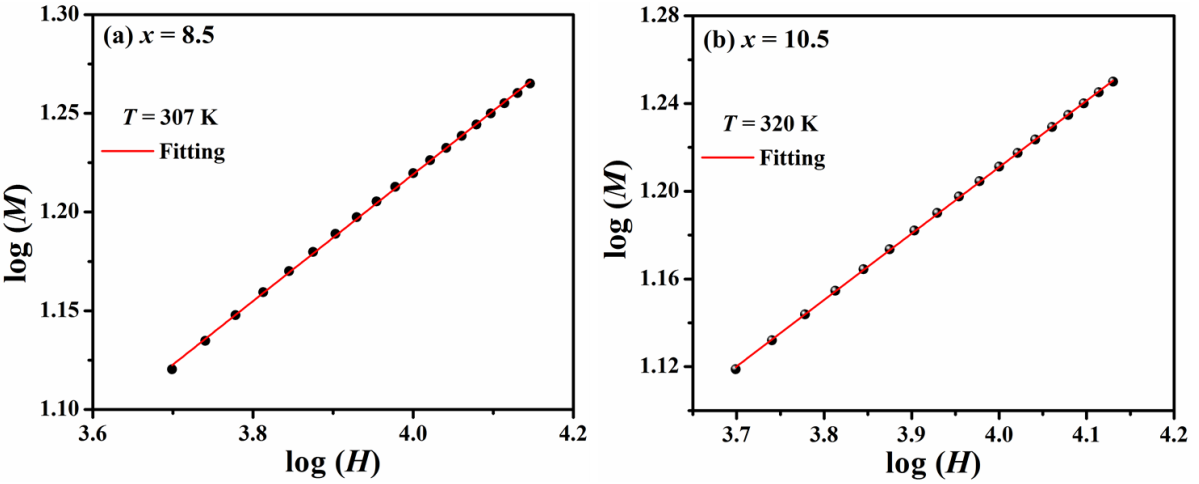

Figure 7.9: log M vs. log H plot for (a) x = 8.5 alloy at T = 307 K (near estimated T_C) and for (b) x = 8.5 alloy at T = 320 K which provide the value of δ as 3.11 for x =8.5 alloy and ~3.33 for x = 10.5 alloy.

Third critical exponent, δ is obtained independently using equation (7.4) from the linear fit of log M vs. log H (shown in **Fig. 7.9**) for the alloy with for x = 8.5 at T = 307 K (~ estimated T_C) and for x = 10.5 alloy at T = 320 K. The determined value of δ is found to be about 3.11 for x =8.5 alloy and ~3.33 for x = 10.5 alloy. Further, using β =

0.42, γ = 1.08 for x = 8.5 and β = 0.40, γ = 0.99 for x = 10.5 from Fig. 7.8, δ is obtained using Widom scaling relation (equation 7.5) and is found to be 3.57 and 3.47 for x = 8.5 and x = 10.5 alloy respectively. These values are close to the obtained values from the critical isotherms which suggest the self-consistency of the critical exponents and T_C.

Moreover, we can expect, the peak value of magnetic entropy change (ΔS_M^{peak}) across the phase transition increases with the increase in a magnetic field following a power law,

$$|\Delta S_M^{peak}| \propto H^n \tag{7.8}$$

where the exponent n is related to the magnetic order and depends on the temperature and magnetic field. The local exponent n is determined by fitting the ΔS_M^{peak} vs. H plot (shown in **Fig. 7.10**) which is found to be 0.77 for x = 8.5 and ~ 0.79 for x = 10.5 alloy. The estimated values of n are in agreement with several reports in similar alloy systems [21,34].

The obtained values of critical exponents suggest the presence of long range ferromagnetic order around the austenite phase transition in these investigated alloys.

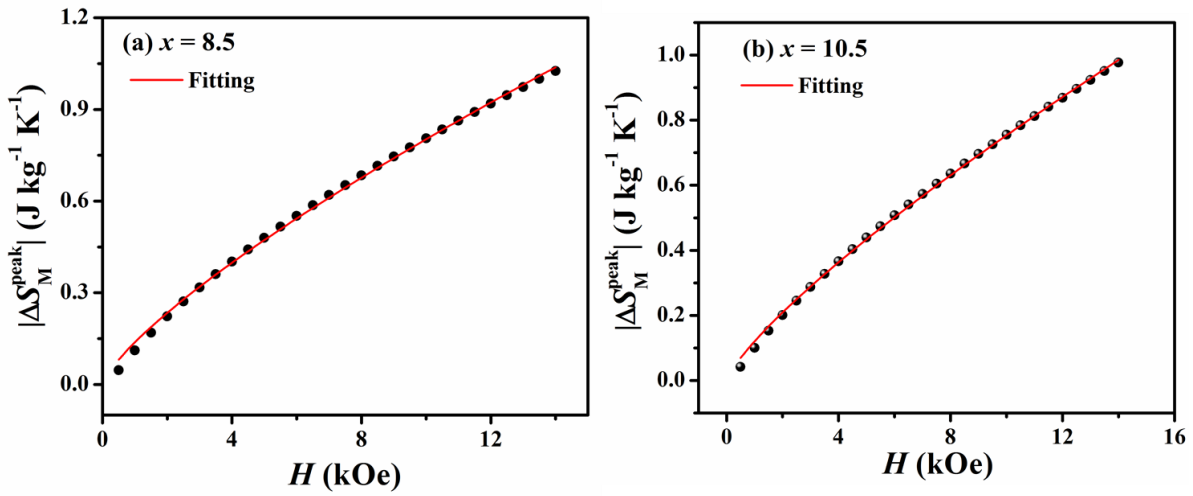

Figure 7.10: Field dependent ΔS_M^{peak} values for the alloy with (a) x = 8.5 and (b) x = 10.5. The linear fits (solid lines) of the data yield the value of exponent n as 0.77 for x = 8.5 and ~ 0.79 for x = 10.5 alloy

Relative cooling power is another important parameter in MCE studies, defined as a measure of the amount of heat transfer between the hot and cold sinks during one ideal refrigeration cycle. It can be calculated from the temperature dependence of ΔS_M curve using the following equation

$$\mathrm{RCP} = |\Delta S_M^{peak}| \times \Delta T_{FWHM} \tag{7.9}$$

where, ΔS_M^{peak} represents the peak value of ΔS_M of a ΔS_M −T curve plotted for a specific field change value and the ΔT_{FWHM} is the temperature window of the full width at half maxima of the same curve. The obtained values of RCP are tabulated in **Table 7.1**. A maximum value of RCP of about 40.2 J/Kg is obtained for x = 8.5 alloy due to field change of 14 kOe whereas it is ~ 36.7 J/kg for the alloy with x = 10.5 due to the same field changes. Hence, RCP decreases with increasing the values of x from 8.5 to 10.5. The observed value of RCPs are comparatively larger than the other reported RCP values of Heusler alloys across their first order structural transition such as $Ni_{47}Mn_{40}Sn_{13}$ (22.2 J/kg for the field change of 20 kOe) [29], $Mn_{50}Ni_{40}Sn_{10}$ (39.8 J/kg due to 50 kOe magnetic field change) [30], $Ni_{50}Mn_{34}In_{16}$ (103.79J/kg for a field change of 50 kOe) [31] and $Ni_{50}Mn_{37}Sb_{13}$ (37.7 J/kg for 50 kOe field change) [35] but it is a bit lower than that of $Gd_5Ge_2Si_2$ (200 J/kg at 5T) [27] which are also tabulated in **Table 7.1**.

7.4 Conclusion

In Summary, we have observed the magnetic, magnetocaloric properties and critical behavior of $Mn_{48-x}Fe_xNi_{41}Sn_{11}$ (x = 8.5, 10.5) alloys across their second order magnetic transition. An increase in Fe concentration in place of Mn decreases the Mn-Mn antiferromagnetic interaction resulting in only austenite phase for $x \geq 8.5$. Large saturation magnetization and a moderate value of room temperature reversible magnetocaloric effect (ΔS_M reaches to a maximum value of ~1.02 J kg^{-1} K^{-1} for x = 8.5 alloy and of ~1.0 J kg^{-1} K^{-1} for x = 10.5 alloy under a field change of 14 kOe only) are found for the investigated alloys along with a large relative cooling power (RCP about

40.2 J/Kg for x = 8.5 and RCP ~ 36.7 J/kg for x =10.5 due to field change of 14 kOe). The Curie temperature of these samples is less sensitive to the doping amount of Fe. The less consumption of energy in the applicability of MCE across second order transition in these materials can make them a good candidate for the magnetic refrigerant. Further, the critical behavior for both alloys has been studied around their second order magnetic transition and the obtained critical exponents confirm the presence of long range ferromagnetic ordering in their austenite phase.

References

[1] T. Krenke, M. Acet, E. F. Wassermann, X. Moya, L. Mañosa, and A. Planes, *Ferromagnetism in the Austenitic and Martensitic States of Ni-Mn-In Alloys*, Phys. Rev. B **73**, 174413 (2006).

[2] N. H. Dan, N. H. Duc, N. H. Yen, P. T. Thanh, L. V Bau, N. M. An, D. T. K. Anh, N. A. Bang, N. T. Mai, P. K. Anh, T. D. Thanh, T. L. Phan, and S. C. Yu, *Magnetic Properties and Magnetocaloric Effect in Ni-Mn-Sn Alloys*, J. Magn. Magn. Mater. **374**, 372 (2015).

[3] T. L. Phan, P. Zhang, N. H. Dan, N. H. Yen, P. T. Thanh, T. D. Thanh, M. H. Phan, and S. C. Yu, *Coexistence of Conventional and Inverse Magnetocaloric Effects and Critical Behaviors in $Ni_{50}Mn_{50-x}XSn_x$ (x = 13 and 14) Alloy Ribbons*, Appl. Phys. Lett. **101**, (2012).

[4] V. D. Buchelnikov and V. V Sokolovskiy, *Magnetocaloric Effect in Ni–Mn–X(X=Ga, In, Sn, Sb) Heusler Alloys*, Phys. Met. Metallogr. **112**, 633 (2011).

[5] S. Fabbrici, J. Kamarad, Z. Arnold, F. Casoli, A. Paoluzi, F. Bolzoni, R. Cabassi, M. Solzi, G. Porcari, C. Pernechele, and F. Albertini, *From Direct to Inverse Giant Magnetocaloric Effect in Co-Doped NiMnGa Multifunctional Alloys*, Acta Mater. **59**, 412 (2011).

[6] Z. D. Han, D. H. Wang, C. L. Zhang, H. C. Xuan, J. R. Zhang, B. X. Gu, and Y. W. Du, *The Phase Transitions, Magnetocaloric Effect, and Magnetoresistance in Co Doped Ni-Mn-Sb Ferromagnetic Shape Memory Alloys*, J. Appl. Phys. **104**, (2008).

[7] A. Ghosh and K. Mandal, *Large Magnetoresistance Associated with Large Inverse Magnetocaloric Effect in Ni-Co-Mn-Sn Alloys*, Eur. Phys. J. B **86**, (2013).

[8] C. Jing, X. L. Wang, P. Liao, Z. Li, Y. J. Yang, B. J. Kang, D. M. Deng, S. X. Cao, J. C. Zhang, and J. Zhu, *Martensitic Phase Transition, Inverse Magnetocaloric Effect, and Magnetostrain in $Ni_{50}Mn_{37-x}Fe_xIn_{13}$ Heusler Alloys*, J. Appl. Phys. **114**, 063907 (2013).

[9] S. C. Ma, Y. Su, M. Yang, F. Yang, Y. L. Huang, K. Liu, L. Zhang, and Z. C. Zhong, *Magnetic Phase Transition and Magnetocaloric Effect in Mn-Fe-Ni-Ge Ribbons*, J. Alloys Compd. **629**, 322 (2015).

[10] L. Chen, F. X. Hu, J. Wang, L. F. Bao, J. R. Sun, B. G. Shen, J. H. Yin, and L. Q. Pan,

Magnetoresistance and Magnetocaloric Properties Involving Strong Metamagnetic Behavior in Fe-Doped $Ni_{45}(Co_{1-x}Fe_x)_5Mn_{36.6}In_{13.4}$ Alloys, Appl. Phys. Lett. **101**, (2012).

[11] M. Khan, I. Dubenko, S. Stadler, and N. Ali, *Exchange Bias in Bulk Mn Rich Ni-Mn-Sn Heusler Alloys*, J. Appl. Phys. **102**, (2007).

[12] A. Ghosh and K. Mandal, *Large Inverse Magnetocaloric Effect in $Ni_{48.5-x}Co_xMn_{37}Sn_{14.5}$ (x = 0, 1 and 2) with Negligible Hysteresis*, J. Alloys Compd. **579**, 295 (2013).

[13] A. Ghosh and K. Mandal, *Effect of Fe Substitution on the Magnetic and Magnetocaloric Properties of Mn-Rich Mn-Ni-Fe-Sn off-Stoichiometric Heusler Alloys*, J. Appl. Phys. **117**, 093909 (2015).

[14] B. Wang and Y. Liu, *Exchange Bias and Inverse Magnetocaloric Effect in Co and Mn Co-Doped Ni2MnGa Shape Memory Alloy*, Metals (Basel). **3**, 69 (2013).

[15] R. Kainuma, Y. Imano, W. Ito, H. Morito, Y. Sutou, K. Oikawa, A. Fujita, K. Ishida, S. Okamoto, O. Kitakami, and T. Kanomata, *Metamagnetic Shape Memory Effect in a Heusler-Type $Ni_{43}Co_7Mn_{39}Sn_{11}$ Polycrystalline Alloy*, Appl. Phys. Lett. **88**, 192513 (2006).

[16] K. Ullakko, J. K. Huang, V. V. Kokorin, and R. C. O'Handley, *Magnetically Controlled Shape Memory Effect in Ni_2MnGa Intermetallics*, Scr. Mater. **36**, 1133 (1997).

[17] M. Oogane, Y. Sakuraba, J. Nakata, H. Kubota, Y. Ando, A. Sakuma, and T. Miyazaki, *Large Tunnel Magnetoresistance in Magnetic Tunnel Junctions Using Co_2MnX (X = Al, Si) Heusler Alloys*, J. Phys. D Appl. Phys. **39**, 834 (2006).

[18] K. Inomata, S. Okamura, A. Miyazaki, M. Kikuchi, N. Tezuka, M. Wojcik, and E. Jedryka, *Structural and Magnetic Properties and Tunnel Magnetoresistance for $Co_2(Cr,Fe)Al$ and Co_2FeSi Full-Heusler Alloys*, J. Phys. D. Appl. Phys. **39**, 816 (2006).

[19] A. K. Nayak, K. G. Suresh, and a. K. Nigam, *Observation of Enhanced Exchange Bias Behavior in NiCoMnSb Heusler Alloys*, J. Phys. D. Appl. Phys. **42**, 115004 (2010).

[20] S. Singh, L. Caron, S. W. D'Souza, T. Fichtner, G. Porcari, S. Fabbrici, C. Shekhar, S. Chadov, M. Solzi, and C. Felser, *Large Magnetization and Reversible Magnetocaloric Effect at the Second-Order Magnetic Transition in Heusler Materials*, Adv. Mater. **28**, 3321 (2016).

[21] G. R. Raji, A. P. Paulose, R. B. Job, S. Thomas, K. G. Suresh, and M. R. Varma, *Phase Transformations, Inverse Magnetocaloric Effect and Critical Behavior of $Ni_{50}Mn_{36}Sn_{14-x}Si_x$ Heusler Alloys*, Intermetallics **82**, 59 (2017).

[22] T. L. Phan, P. Zhang, N. H. Dan, N. H. Yen, P. T. Thanh, T. D. Thanh, M. H. Phan, and S. C. Yu, *Coexistence of Conventional and Inverse Magnetocaloric Effects and Critical Behaviors in $Ni_{50}Mn_{50-x}Sn_x$ (x = 13 and 14) Alloy Ribbons*, Appl. Phys. Lett. **101**, 0 (2012).

[23] S. Pandey, A. Quetz, A. Aryal, I. Dubenko, D. Mazumdar, S. Stadler, and N. Ali, *Magnetocaloric, Thermal, and Magnetotransport Properties of $Ni_{50}Mn_{35}In_{13.9}B_{1.1}$ Heusler Alloy*, J. Magn. Magn. Mater. **444**, 98 (2017).

[24] D. H. Wang, C. L. Zhang, H. C. Xuan, Z. D. Han, J. R. Zhang, S. L. Tang, B. X. Gu, and Y. W. Du, *The Study of Low-Field Positive and Negative Magnetic Entropy Changes in $Ni_{43}Mn_{46-x}Cu_xSn_{11}$ Alloys*, J. Appl. Phys. **102**, (2007).

[25] N. G. Bebenin, R. . Zainullina, V. . Ustinov, and Y. M. Mukovskii, *Magnetic Properties of $La_{0.7-x}Pr_xCa_{0.3}MnO_3$ Single Crystals: When Is Banerjee Criterion Applicable?*, J. Magn. Magn. Mater. **354**, 76 (2014).

[26] K. A. GschneidnerJr, V. K. Pecharsky, and A. O. Tsokol, *Recent Developments in Magnetocaloric Materials*, Reports Prog. Phys. **68**, 1479 (2005).

[27] V. Provenzano, A. J. Shapiro, and R. D. Shull, *Reduction of Hysteresis Losses in the Magnetic Refrigerant $Gd_5Ge_2Si_2$ by the Addition of Iron*, Nature **429**, 853 (2004).

[28] S. Arumugam, S. Ghosh, A. Ghosh, U. Devarajan, M. Kannan, L. Govindaraj, and K. Mandal, *Effect of Hydrostatic Pressure on the Magnetic, Exchange Bias and Magnetocaloric Properties of $Ni_{45.5}Co_2Mn_{37.5}Sn_{15}$*, J. Alloys Compd. **712**, 714 (2017).

[29] A. G. Varzaneh, P. Kameli, F. Karimzadeh, B. Aslibeiki, G. Varvaro, and H. Salamati, *Magnetocaloric Effect in $Ni_{47}Mn_{40}Sn_{13}$ Alloy Prepared by Mechanical Alloying*, J. Alloys Compd. **598**, 6 (2014).

[30] J. Sharma and K. G. Suresh, *Investigation of Multifunctional Properties of $Mn_{50}Ni_{40-x}Co_xSn_{10}$ (x = 0-6) Heusler Alloys*, J. Alloys Compd. **620**, 329 (2015).

[31] V. K. Sharma, M. K. Chattopadhyay, and S. B. Roy, *Large Inverse Magnetocaloric Effect in $Ni_{50}Mn_{34}In_{16}$*, J. Phys. D. Appl. Phys. **40**, 1869 (2007).

[32] M. E. Fisher, *The Theory of Equilibrium Critical Phenomena*, Vol. 30 (1967).

[33] J. S. Kouvel and M. E. Fisher, *Detailed Magnetic Behavior of Nickel Near Its Curie Point*, Phys. Rev. **136**, A1626 (1964).

[34] S. Arumugam, U. Devarajan, S. E. Muthu, S. Singh, R. Thiyagarajan, M. M. Raja, N. V. R. Rao, and A. Banerjee, *Journal of Magnetism and Magnetic Materials Structural , Transport, Magnetic, Magnetocaloric Properties and Critical Analysis of Ni-Co-Mn-Ga Heusler Alloys*, **442**, 460 (2017).

[35] J. Du, Q. Zheng, W. J. Ren, W. J. Feng, X. G. Liu, and Z. D. Zhang, *Magnetocaloric Effect and Magnetic-Field-Induced Shape Recovery Effect at Room Temperature in Ferromagnetic Heusler Alloy Ni-Mn-Sb*, J. Phys. D. Appl. Phys. **40**, 5523 (2007).

Chapter 8 | Conclusion and scope for future study

This chapter represents an overall conclusion of the present thesis and describes about the scope of future work in the related field.

8.1 Overall conclusion of thesis

In the present thesis, we have investigated principally the magnetocaloric properties of transition metal based alloys such as MnNiSi-based intermetallic compound and NiMnSn-based Heusler alloy which contain earth-abundant elements, in search of cost-effective magnetic refrigerant material with giant MCE response for room temperature magnetic refrigeration technology. For NiMnSn-based Heusler alloy, due to the presence of ferromagnetic-antiferromagnetic correlation in the low temperature martensite phase, we have studied the exchange bias property. For the preparation of alloy, a conventional arc-melting technique is used followed by heat treatment in a vacuum. To extract the crystal structure information and elemental composition, XRD and EDAX are used. Magnetic, exchange bias, and MCE response of the samples are explored using VSM, PPMS, and SQUID. The essential findings of the present studies are discussed as follows.

We have observed first order coupled magnetostructural transition between FM orthorhombic and PM hexagonal structure and giant MCE across the MST in transition metal based Al doped $(Mn_{0.6}Fe_{0.4})NiSi_{1-x}Al_x$ (x = 0.06, 0.07) alloys. On doping Al in place of Si and for a fixed doping of Fe in place of Mn, the structural transition temperature is found to shift to around room temperature (~272 K for x = 0.07) from a high temperature of about 1210 K for MnNiSi system. On further increase in Al doping with x = 0.08, only magnetic transition is observed at about 136 K. Isothermal field dependent magnetization is measured across the MST to deduce MCE response using Maxwell equation. Here, we have discussed that isotherms should be measured during cooling to estimate the magnetocaloric parameter accurately. Isothermal magnetic entropy change (ΔS_M) as large as about 20.6 J kg^{-1} K^{-1} with large relative cooling power (RCP) ~249.2 J/kg is found for the alloy with x = 0.07 due to a magnetic field change of 50 kOe. Our results suggest that these materials can be potential candidates for the magnetic refrigerant.

Further, magnetic and structural transitions are observed to coincide at around room temperature in transition metal based $(MnNiSi)_{1-x}(FeCoGa)_x$ (x = 0.15 and 0.16)

alloys which lead to a coupled first order MST from PM hexagonal to FM orthorhombic structure and as a result giant MCE is observed in these alloys. With subsequent doping for x = 0.17, MST decouples into two separate transitions, structural and magnetic, though the transitions are realized to couple with enhancing the applied magnetic field. Substitution of Fe with relatively lower atomic radius in place of Mn increases the orthorhombic distortion and stabilizes the hexagonal phase at a lower temperature, resulting both T_C and T_M reduce towards room temperature with lower saturation magnetization. To compensate for the reduction in magnetization, Co can be doped in place of Ni, where Co enhances the ferromagnetic interaction to the system. Ga having a much larger atomic radius than Si again enhances orthorhombic distortion in a faster way to the system which couples T_C and T_M and as a result, MST is obtained in the vicinity of room temperature. Here, measuring isotherm during cooling mode is found to be preferred to estimate the precise value of magnetic entropy change for this type of material. The significant jump in magnetization across MST arises from the lattice as well as magnetic structure changes in the coupled transition, developing a giant magnetic entropy change in these investigated alloys. The alloys with x = 0.15, 0.16, and 0.17 are found to exhibit ΔS_M as large as about 25 J kg^{-1} K^{-1} at 323 K, ~31.1 J kg^{-1} K^{-1} at 281 K, and ~23.8 J kg^{-1} K^{-1} at 213 K respectively due to a field change of ΔH = 50 kOe. Moreover, MST for this investigated compound, $(MnNiSi)_{1-x}(FeCoGa)_x$, is tunable from 224 K – 342 K with a broad temperature window of 118 K which will be beneficial for magnetic refrigeration associated with wide and controllable operating temperature. Hence, these low-cost materials may be considered as promising candidates for magnetic refrigeration around room temperature due to their giant magnetocaloric properties with significantly large relative cooling power (RCP = 191.8, 209.6, and 139.2 J/kg respectively for x = 0.15, 0.16, and 0.17 due to ΔH = 50 kOe).

Next, we have investigated the effect of hydrostatic pressure and magnetic field on the magnetization, magnetocaloric effect, and exchange bias effect in a Co doped Ni-rich $Ni_{45.5}Co_2Mn_{37.5}Sn_{15}$ Heusler alloy. At ambient pressure, the martensitic transition temperature shifts to a lower temperature with a rate of $dT_M/d\mu_0 H \sim 3.29$ K/T whereas, T_M increases rapidly to a higher temperature with a shift rate of dT_M/dP ~31.90 K/GPa

when hydrostatic pressure is applied. Hence, the first order MST of similar materials can be tuned by applying both hydrostatic pressure and magnetic field as they influence the transition temperature oppositely. The coercivity of the sample at a given temperature merely changes, but the exchange bias effect in low temperature is improved by applying pressure. Although the ΔS_M associated with the net RCP decreases a little bit with an increase in pressure, a fine control of operating temperature is possible by applying hydrostatic pressure with the magnetic field which is very advantageous in the context of the application of similar materials to achieve potential magnetic cooling.

The addition of a small amount of Co substituting Ni in NiMnSn-based Heusler alloys enhances the ΔS_M value but the appearance of field induced hysteresis across the first order MST reduces the net RCP of that material in higher doping concentrations. Therefore to improve the inverse MCE properties of Heusler alloys, we have to reduce the hysteresis losses significantly to make their commercial use as refrigerant material. For that purpose, we have studied the magnetic, exchange bias, and MCE response of Si doped polycrystalline $Ni_{48}Co_{1.5}Mn_{35}Sn_{15.5-x}Si_x$ (x = 0, 1, 2, 4) Heusler alloys. These alloys are found to undergo a first order structural phase transition from martensite to austenite along with a second order FM to PM transition. With increasing Si substitution in place of Sn, martensitic transition temperature shifts to lower temperature whereas the Curie temperature (T_C) remains insensitive to the doping content. ΔS_M is found to reduce with Si content. Interestingly, the average hysteresis losses decrease drastically from 49.7 J/kg to 8.6 J/kg with the increase in Si substitution from x = 0 to x = 4, which can enhance the effective RCP of the materials. A maximum net RCP of about 141.8 J/kg has been observed for x = 2 alloy. Therefore, a small amount of Si substitution in place of main group element can enhance the effective efficiency of these similar kinds of alloys which can make them good refrigerant material for practical application.

Finally, to improve the conventional MCE across the second order magnetic transition of NiMnSn-based Heusler alloys, we have explored the magnetic, magnetocaloric properties and critical exponents of $Mn_{48-x}Fe_xNi_{41}Sn_{11}$ (x = 8.5, 10.5)

alloys across their second order transitions. These alloys show only second order FM to PM transition at their T_C and no structural transformation is observed. An increase of Fe doping content in place of Mn decreases the Mn-Mn antiferromagnetic interaction resulting in only austenite phase for $x \geq 8.5$. Second order transition being continuous is not associated with thermal and field induced hysteresis. A large value of saturation magnetization (M_S) about 72.76 Am^2/kg is observed at 80 K for $x = 8.5$ alloy as the alloy becomes purely austenite for this composition. A reversible ΔS_M of about 1.02 J Kg^{-1} K^{-1} with moderate RCP ~ 40.2 J/kg is obtained near room temperature (~305 K) for $x = 8.5$, across its T_C due to a field change of 14 kOe only. The less consumption of energy in the applicability of MCE across second order transition in these materials can make them a good candidate for magnetic refrigerant. Further, the critical exponents are calculated for both the samples and found to exhibit long range ferromagnetic ordering in their austenite phase.

We have tabulated all the important parameters related to the magnetocaloric properties of our investigated samples in **Table 8.1**. Here, $(Mn_{0.6}Fe_{0.4})NiSi_{1-x}Al_x$ and $(MnNiSi)_{1-x}(FeCoGa)_x$ alloys exhibit giant magnetocaloric properties around room temperature and MCE is tunable in a board operating temperature window. Moreover, these materials are non-toxic and very cheap compared to the already proposed rare earth based and transition metal based magnetocaloric materials described in **Chapter 1**. Besides, from the MCE response of our studied MnNiSi-based compounds, we suggest that instead of using single material if we cascade multiple materials to use as a refrigerant, an enormous efficiency of magnetic refrigeration as well as large operating temperature region can be achieved. For instance; the operational temperature window with giant MCE can be extended from 224 K – 342 K by cascading $(MnNiSi)_{1-x}(FeCoGa)_x$ with $x = 0.15 - 0.17$ and their intermediate compositions. However, Heusler alloys are already proposed as promising magnetocaloric materials. Further, we have presented that, by applying hydrostatic pressure with the magnetic field a fine control of operating temperature is possible as they are found to influence the first order MST oppositely and also the use of pressure retains the similar MCE response of the material. Si doping in place of post transition element of Heusler alloys is found to be an effective way to

reduce the hysteresis losses across first order transition significantly. Beside, inverse MCE, we have explored reversible MCE in Heusler alloys by tuning the second order magnetic transition near room temperature and the saturation magnetization. Thus, a proper device fabrication using our investigated low-cost transition metal based materials as a refrigerant may accelerate the path to construct a cost-effective, energy-efficient, and eco-friendly room temperature magnetic refrigerator for cooling technology.

Table 8.1: Peak value of isothermal magnetic entropy change (ΔS_M^{peak}), peak temperature where maximum ΔS_M is maximum (T_{peak}), average hysteresis loss (HL), relative cooling power (RCP) of the studied materials of the present thesis.

Samples	**ΔH (kOe)**	**ΔS_M^{peak} (J kg^{-1} K^{-1})**	**T_{peak} (K)**	**HL (J kg^{-1})**	**RCP (J kg^{-1})**
$(Mn_{0.6}Fe_{0.4})NiSi_{1-x}Al_x$					
x = 0.06	14	−5.1	317	–	21.5
x = 0.07	50	−20.6	256	–	249.2
	14	−7.1	249	–	56.8
$(MnNiSi)_{1-x}(FeCoGa)_x$					
x = 0.15	50	−25	323	–	191.8
x = 0.16	50	−31.1	281	–	209.6
x = 0.17	50	−23.8	213	–	139.2
$Ni_{45.5}Co_2Mn_{37.5}Sn_{15}$	50	13.4 (P = 0 Gpa)	237	53.1	147
		10.2 (P = 0.7 Gpa)	258	39.8	146.6
		11.0 (P = 0.9 Gpa)	263	40.9	130.1
$Ni_{48}Co_{1.5}Mn_{35}Sn_{15.5-x}Si_x$					
x = 0	50	11.99	248	49.7	136.1
x = 1	50	10.86	193	41.6	130.1
x = 2	50	5.46	188	19.3	141.8
x = 4	50	2.42	163	8.6	63
$Mn_{48-x}Fe_xNi_{41}Sn_{11}$					
x = 8.5	14	−1.02	306	–	40.2
x = 10.5	14	−1.00	319	–	36.7

8.2 Scope of Future study

Magnetic and structural transitions are observed to coincide at around room temperature in transition metal based $(Mn_{0.6}Fe_{0.4})NiSi_{1-x}Al_x$ (x = 0.06, 0.07) alloys and $(MnNiSi)_{1-y}(FeCoGa)_y$ (y = 0.15 − 0.17) alloys which lead to a coupled first order MST from PM hexagonal to FM orthorhombic structure and as a result, giant MCE is observed in these alloys. In these doped MnNiSi compounds, a remarkable shifting of structural transition temperature from about 1210 K for MnNiSi compound, to lower than 300 K is observed. Due to Fe doping in place of Mn, the saturation magnetization of the material reduces. To compensate for the reduction in magnetization, we have doped Co in place Ni in $(MnNiSi)_{1-x}(FeCoGa)_x$ system which also shows coupled MST around room temperature with large saturation magnetization. Usually, the reduction of structural transition temperature depends on the hexagonal distortion ratio, c_{hex}/a_{hex} (or a_{ortho}/b_{ortho}); when c_{hex}/a_{hex} decreases, the structural transition is found to shift toward room temperature from a high temperature of about 1210 K. Substitution of the transition elements with lower atomic radius in place of Mn reduces the value of c_{hex}, whereas the substitution of elements with higher atomic radius in place of Si site enhances a_{hex} value. Thus, c_{hex}/a_{hex} can be reduced in a faster way with double elements substitution and we have observed that MST is obtained near room temperature when $c_{hex}/a_{hex} \sim 1.30$. Therefore, it will be very interesting to study the MCE properties of the mentioned system with fixed doping of Fe/Co in place of Mn and then, by substituting of other post transition element such as Ga, Sn, In, Sb, Al, Ge in place of Si. Further, a phase diagram can be established in MnNiSi system by Fe/Co doping in place of Ni which may extend the study of MCE with elemental substitution to find better refrigerant material. An effect of the annealing temperature and the time of heat treatment on the MCE response of these materials can be investigated to know the influences of structural disorder on the MCE response of these materials. Further, to know the grain size dependence of MCE, one can prepare the ribbon form of these alloys. In addition to the magnetic field, hydrostatic pressure can also be applied to tune the magnetocaloric properties of these alloys as usually the hydrostatic pressure and magnetic field influence the transition temperature oppositely. Moreover, as MST of the investigated

systems is accompanied with a significant change in unit cell volume along with a large change in magnetization, it may exhibit interesting findings in the study of magnetoresistance properties.

Besides, the MCE response of NiMn-based Heusler alloys with various main group elements (p-block) such as Ga, In, Sb, Sn etc. have been explored in search of suitable refrigerant material for magnetic refrigeration technology. A few percent of Co or Fe doping in place of Ni enhances the ferromagnetic interaction to the system and which in turn enhances the MCE responses. At the same time, the first order transition shifts to the lower temperature and also, the thermal as well as magnetic hysteresis enhances which generates the irreversibility of MCE. We have observed that without affecting the MCE response, the application of hydrostatic pressure can regulate the operating temperature. We have shown that Si doping in place of post transition element can be an effective way to reduce the magnetic hysteresis losses significantly although it diminishes the MCE parameter. The MCE response of these alloys in ribbon form can be investigated further as the reduction of grain size may play a crucial role to reduce the hysteresis. Moreover, other similar elements having relatively smaller atomic radii can be partially substituted in place of the p-block element. The magnetic interactions and structural properties in these materials depend extensively on the inter-atomic spacing. Hence, by changing the lattice parameter we can explore the various interesting physical properties.

Recently, the d-metal Ti is found to show a similar effect to the p-block element on forming and stabilizing all d-metal Heusler alloy structure. Co/Fe substitution in place of Ni originates strong ferromagnetic coupling in the antiferromagnetic austenite of Ni(Co/Fe)-Mn-Ti alloys. On doping Fe/Co, the structural transition shifts to lower temperature whereas Curie temperature increases toward higher temperature, hence a tuning of inverse and conventional MCE is possible. Other transition elements such as Cu, Cr, and double transition elements can be co-doped to investigate the MCE as valence electron concentration (e/a) influences the transition temperature significantly. Similarly, other p-block elements can be doped in place of Ti to tune the MCE response

of all d-metal Heusler alloy. Hydrostatic pressure can be added as a stimulus with the magnetic field to tune the MCE properties further. In addition, the magnetoresistance of these alloys should be explored across first order MST.

Thus, the recent research activity should be to explore the new low-cost magnetocaloric material with giant MCE response around room temperature and also the optimization of the known material to make it suitable for commercial application. Although many prototypes are demonstrated to achieve room temperature magnetic cooling, still a considerable effort is required to make it commercially available.